High-Cycle Dynamic Cell Fatigue with Applications on Oncotripsy

Thesis by
Erika Figueroa-Schibber

In Partial Fulfillment of the Requirements for the
Degree of
Doctor of Philosophy in Space Engineering

CALIFORNIA INSTITUTE OF TECHNOLOGY
Pasadena, California

2020
Defended September 27, 2019

Erika Figueroa-Schibber
ORCID: 0000-0002-6629-297X

ACKNOWLEDGEMENTS

I would like to express my most profound appreciation to my advisor Professor Michael Ortiz, for his guidance and unparalleled support. Without his advice and expertise, this research and dissertation would not have happened.

Moreover, I would like to thank the members of my committee, Professors Domniki Asimkai, Guruswami Ravichandran, and Morteza Gharib, for their encouragement, support, and feedback. I also want to acknowledge Professor Mikhail Shapiro for his helpful advice throughout my project. His suggestions and invaluable insight into the experimental observations have enabled me to build a better model of Oncotripsy.

In addition, I want to thank Stefanie Heyden for introducing and guiding me at the early stages of this project. Special thanks to David Mittelstein for his collaboration and invaluable work on the Oncotripsy experiments. Particularly helpful during his visit to Caltech was Professor Laurent Stainier, who spend hours with me looking for bugs in my code. I very much appreciate Mauro Rodriguez's help, who taught me about bubble dynamics.

I gratefully acknowledge the funding sources towards my Ph.D. The Keck Institute for Space Studies funded me through my first year at Caltech. My research would not have been possible without the support of the Jones Family Trust Caltech Innovation Initiative and the funding of the Amgen Bioengineering Research Program.

My years at Caltech would not have been the same without the members of my group. Thanks to Lydia, who went above and beyond to make my stay at Caltech better. I will always cherish the coffee breaks with Trent and Will, in which we will start talking about math problems and finish on how to make our plots look pretty. Being a teaching assistant would not have been the same without the other A-Team members, Arnold and Will. I also want to thank Amir for the time we spent talking about my research and on the ideas that came with such conversations.

I have always been amazed by Caltech's fantastic staff. Everyone I met has always been willing to help me. Christine Ramirez has welcomed me in her office with a smile since the first day I stepped in Galcit. Erin-Kate Escobar has supported and helped me in every attempt to make Caltech a more inclusive place. Working with her in the *Women's Engagement Board* has been one of the best experiences I had in

grad school. Laura Flower and Daniel Yoder have made my life easier as I navigated the U.S. as an international student.

My deepest gratitude goes to my friends, who filled one of the most stressful times in my life with happy memories. My first year wouldn't have been the same without the support of my classmates. In particular, I recall all those evenings doing homework or studying for quals with Fabien and Simon. I also feel very fortunate to have cross paths with my loving friends Ana, Becky, Kavya, Tori, and Ying-Shi. Caltech would not have been the same without them, and I will treasure their friendship forever.

Finally, I want to express my most profound gratitude to my family, in particular to my dad, sisters —Connie and Evelyn—, and brothers-in-law —Gaston and Pablo— for their continuous encouragement and support throughout my years of study. They are my biggest fans and cheerleaders, and I would not have come to Caltech and accomplished this without them.

ABSTRACT

The method of *oncotripsy* (from Greek, *onco-* meaning "tumor" and *-tripsy* "to break") exploits aberrations in the material properties and morphology of cancerous cells in order to target them selectively by means of tuned low-intensity ultrasound. Compared to other noninvasive high-intensity ultrasound treatments that ablate unhealthy tissue, such as lithotripsy (which utilizes shock waves to fragment stones within the kidney and ureter) and histotripsy (which uses pulsed cavitation ultrasound to destroy tissue) oncotripsy is a cancer treatment with the capability of targeting unhealthy tissue with minimal damage to healthy cells in the ablation process.

We propose a model of oncotripsy that follows as an application of cell dynamics, statistical mechanical theory of network elasticity, and 'birth-death' kinetics to describe processes of damage and repair of the cytoskeleton. We also develop a reduced dynamical model that approximates the three-dimensional dynamics of the cell and facilitates parameter studies, including sensitivity analysis and process optimization.

The dynamical system encompasses the relative motion of the nucleus with respect to the cell membrane and a state variable measuring the extent of damage to the cytoskeleton. The cell membrane is assumed to move rigidly according to the particle velocity induced in the water by the insonation. The dynamical system evolves in time as a result of structural dynamics and kinetics of cytoskeletal damage and repair. The resulting dynamics is complex and exhibits behavior on multiple time scales, including the period of vibration and attenuation, the characteristic time of cytoskeletal healing, the pulsing period, and the time of exposure to the ultrasound. We also account for cell variability and estimate the attendant variance of the time-to-death of a cell population. We show that the dynamical model predicts — and provides a conceptual basis for understanding — the oncotripsy effect and other trends observed in experiments.

PUBLISHED CONTENT AND CONTRIBUTIONS

- Schibber, E. F., Mittelstein, D. R., Gharib, M., Shapiro, M. G., Lee, P. P., Ortiz, M., 2019. A dynamical model of oncotripsy by mechanical cell fatigue: Selective cancer cell ablation by low-intensity pulsed ultrasound. Arxiv. `https://arxiv.org/abs/1911.12407`.
  MO conceived the study. EFS and MO developed the theory and drafted the manuscript with input from all authors. All authors discussed the manuscript and gave final approval for publication. Article adapted for Chapters 2, 4 and 5.

- Schibber, E. F., Salahshoor, H., Ortiz, M., 2019. Quantitative oncotripsy, work in progress.
  EFS participated in the conception of the project, in developing the theory, solved and analyzed the model, prepared the plots, and participated in the writing of the manuscript. This work is presented in Chapter 6.

TABLE OF CONTENTS

LIST OF ILLUSTRATIONS

LIST OF TABLES

Chapter 1

INTRODUCTION

The method of *oncotripsy* (from Greek, *onco-* meaning "tumor" and *-tripsy* "to break") exploits aberrations in the material properties and morphology of cancerous cells in order to target them selectively by means of tuned low-intensity ultrasound. Compared to other noninvasive high-intensity ultrasound treatments that ablate unhealthy tissue, such as lithotripsy (which utilizes shock waves to fragment stones within the kidney and ureter) and histotripsy (which uses pulsed cavitation ultrasound to destroy tissue) oncotripsy is a cancer treatment with the capability of targeting unhealthy tissue with minimal damage to healthy cells in the ablation process.

A wealth of observational evidence reveals that healthy and cancerous cell have different morphologies and material properties, cf., e.g., Figs. 1.1 and 1.2. A substantial size difference between normal nuclei, with an average diameter of 7 to 9 microns, and malignant nuclei, which can reach a diameter of over 50 microns, often characterizes malignancy [7]. It has also been found that the cell stiffness of metastatic cancer cells is more than 70% softer than the benign cells that line the body cavity [13]. This was found using atomic force microscopy to measure the stiffness of live metastatic cancer cells taken from pleural fluids of patients with suspected lung, breast, and pancreas cancer. Swaminathan *et al.* [76] found that cells with the highest invasion and migratory potential are up to five times softer than healthy cells using a magnetic tweezer system to measure the stiffness of human ovarian cancer cell lines. Smolyakov *et al.* [72] experiments showed increasing cytoskeletal disorganization as cells invasiveness grows (Fig. 1.3). Experimental investigations of hepatocellular carcinoma cells (HCC) have also found that an increase in stiffness of the extracellular matrix (ECM) promotes HCC proliferation [70] and advances malignant growth [43]. This implies that altered mechanics properties are not just a diagnosis, but possibly a causal mechanism for cancer cell growth.

Owing to these and other similar observed aberrations in material properties and morphology attendant to malignancy, the cell resonance frequencies occurs are expected to differ markedly between healthy and cancerous cells. In a recent numerical study [29], Heyden and Ortiz have shown that HCC natural frequencies lie above

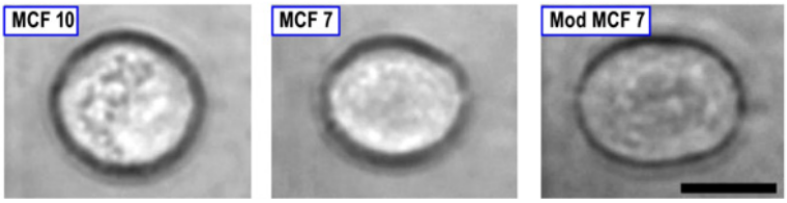

Figure 1.1: Optical images showing deformability on three breast cells due to a constant stretching laser power of 600mW. Deformability increases in the cancerous MCF-7 and ModMCF-7 cells in comparison to the healthy cell MCF-10. Reprinted from [75], with permission from Elsevier.

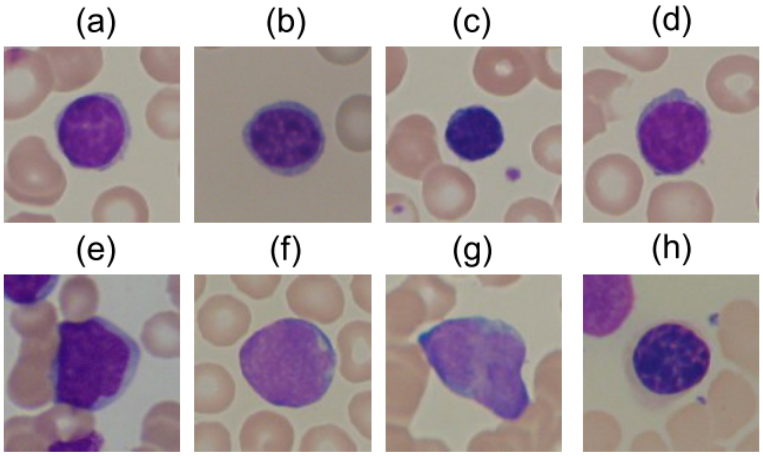

Figure 1.2: (a-d) Healthy lymphocyte cells from non-Acute Lymphoblastic Leukemia patients. (e-h) Probable lymphoblast cells showing marked differences in size and morphology with respect to the healthy cells. Reprinted from [39]. Copyright © 2011 IEEE.

those of healthy cells, with a typical gap in the lowest natural frequency of about 37 kHz. For instance, they computed the fundamental frequency of HCC and health cells to respectively be on the order of 80 kHz and 43 kHz. Heyden and Ortiz [29] posited that, by exploiting this *spectral gap* between cancerous and healthy cells, *oncolysis*, or killing of cancerous cells, can be induced selectively using carefully tuned ultrasound while simultaneously leaving normal cells intact, an effect that they referred to as *oncotripsy*. Specifically, by studying numerically the vibrational response of HCC and healthy cells, Heyden and Ortiz [29] found that, by carefully tuning the frequency of the harmonic excitation, lysis of the HCC nucleolus membrane could be induced selectively at no risk to healthy cells. They also estimated the acoustic density required for oncotripsy to operate to be in a low-intensity ultrasound range of the order of a few W/cm^2. This low-intensity requirement sets oncotripsy apart from High-Intensity Focused Ultrasound (HIFU), which acts via

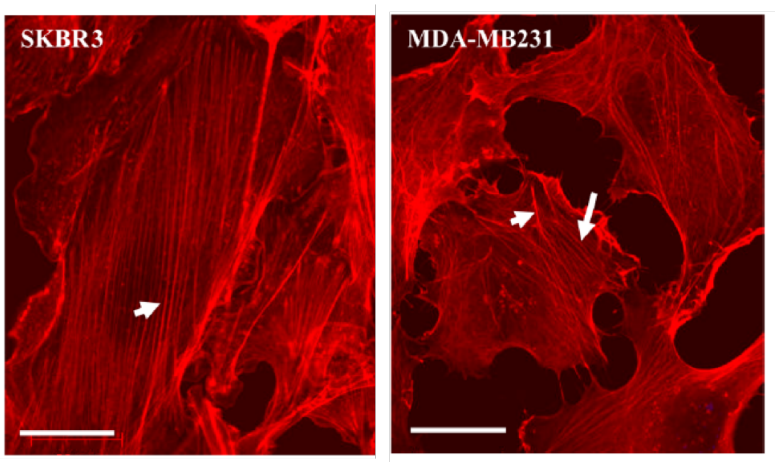

Figure 1.3: Cytoskeletal organization in breast tumor cells varies with the level of invasiveness. In the SKBR3 cell (left), the least invasive, the filaments are well-organized (short solid arrow). On the contrary, in the MDA-MB231 cell (right) the fibers are of unequal thickness and lengths, and there is no preferred organization. Reprinted with permission from [72]. Copyright © 2016 American Chemical Society.

thermal ablation and is non-specific as to cancer cell selectivity.

The first numerical calculations of Heyden and Ortiz [29] neglected viscoelasticity and damping in the cell and ECM. Under these conditions, the resonant response of the cells exhibits rapid linear growth in time, and the cells are predicted to attain lysis relatively quickly. However, experimental studies suggest that the material behavior of the different cell constituents is viscoelastic [24, 32, 63, 84]. In a subsequent study, Heyden and Ortiz [28] investigated the influence of viscoelasticity on the oncotripsy effect. They assumed Rayleigh damping and estimated the damping coefficients from dynamic atomic force microscopy (AFM) experiments on live fibroblast cells in buffer solutions [9]. They concluded that, for these cells, the main effect of viscoelasticity is a modest reduction in the natural frequencies of the cells and an equally modest increase of the time to lysis of the cancerous cells. Based on these results, they speculated that oncotripsy remains viable when viscoelasticity is taken into account.

Following these leads, Mittelstein *et al.* [54] have endeavored to assess the oncotripsy effect in carefully designed laboratory tests involving several cancerous cell lines in aqueous suspension. They have developed a system for testing oncoptripsy that includes a tunable source of ultrasonic transduction in signal communication with a control system that allows control of several parameters, including frequency

and pulse duration of the ultrasonic transduction. Transducers were selected to produce ultrasound pulses in the frequency range of approximately 100 kHz to 1 MHz, a pulse duration range of 1 ms to 1 s, acoustic intensity up to 5 W/cm^2, and output pressure up to 2 MPa. The instrumentation of the system allows the measurement of estimated cell death rates as a function of frequency, pressure, pulse duration, duty cycle, and the number of cycles.

In agreement with the original oncotripsy concept, the experiments confirm that the application of low-intensity pulsed ultrasound (LIPUS) can indeed result in high death rates in the cancerous cell population *selectively*, i. e., simultaneously with small or zero death rates among healthy cells. The death and survival rates depend critically on the frequency of the ultrasound, indicative of the dynamical response of the cells. The oncotripsy effect is observed to be maximized at a single measured frequency for a given type of cells, and diminishes at both larger and smaller frequencies. This behavior is consistent with a resonant response in cells. However, under the conditions of the experiments, cell death is observed to require the application of a much larger number of ultrasound cycles than anticipated by either [29] or [28], suggesting that the cell dynamics is much more heavily damped than estimated in [28] based on the AFM measurements of [9]. The observations reported by Mittelstein *et al.* [54] suggest that, under the conditions of the experiment, cell death occurs through a process of slow accumulation of damage over many cycles. This contrasts with the rapid rupture of cell membranes, as hypothesized in [29].

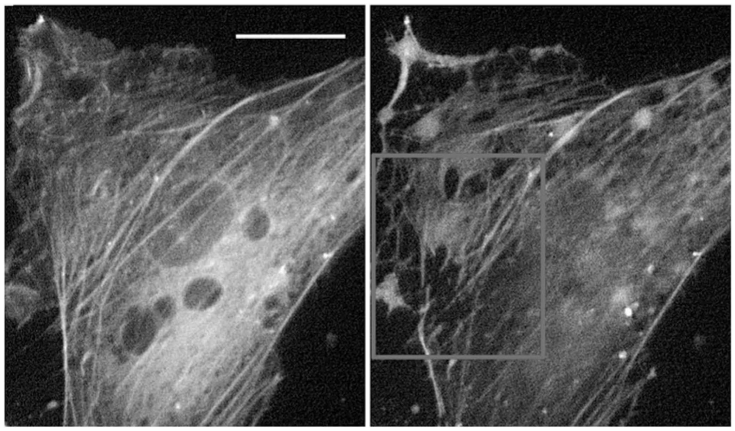

Figure 1.4: Live yellow fluorescent protein (YFP) tagged actin network staining of cells before and 5 min after exposure to 290 kPa acoustic pressure showing massive fiber disruption. Scale bar 10 μm. Reproduced from Ref. [55] with permission from The Royal Society of Chemistry.

Several experimental investigations suggest a mechanistic basis for the oncotripsy effect observed by Mittelstein *et al.* [54]. The susceptibility of the cytoskeleton dynamics to therapeutic ultrasound, at strains of the order of 10^{-5} and frequencies in the MHz range, has been noted by [55]. At low acoustic intensities, no structural network changes are observed throughout the experiments. By contrast, at sufficiently high acoustic intensities the actin network is progressively disrupted and disassembles within three minutes following exposure, Fig. 1.4. This disruption is accompanied by a 50% reduction in cell stiffness. Remarkably, after exposure to moderate acoustic intensities, the stiffness of the cell gradually recovers and returns to its initial value. The mechanisms of actin stress-fiber repair have been extensively studied and reasonably well-understood at present, cf., e. g., [57, 71] and references therein. By contrast, at high acoustic intensities, no recovery takes place after cessation throughout the observation.

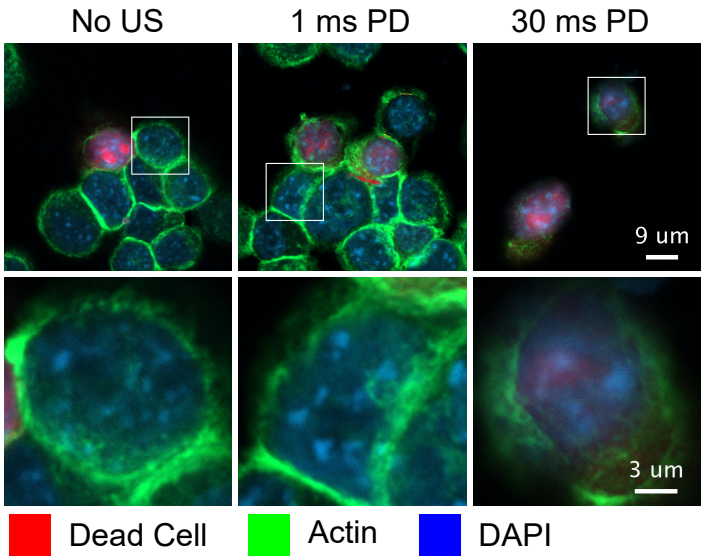

Figure 1.5: Confocal microscopy of CT-26 cells immediately after LIPUS treatment at 500kHz, focal pressure of 1.4MPa and pulse durations 0 ms (control), 1 ms and 30 ms (reproduced from [54]). Dead cells stained red with fixable LIVE/DEAD, actin cytoskeleton stained green using phalloiding, and nucleus stained blue with DAPI. Confocal images shows disrupted actin cytoskeleton ring and significantly decreased actin stain intensity. Microscopy suggests LIPUS cytodisruption is coupled with persistent cytoskeletal disruption.

To gain insight into the biomolecular mechanisms of LIPUS cytodisruption, Mittelstein *et al.* [54] examined CT-26 cells after 2-minute LIPUS treatment at 500 kHz and focal pressure of 1.4 MPa. To evaluate the effect of LIPUS on the cytoskeleton, they plated CT-26 cells after LIPUS and performed confocal microscopy immediately after insonation. Confocal images show the actin cytoskeleton, stained with

phalloidin-conjugated green dye, as a ring on the cell periphery, Fig. 1.5. This ring is disrupted and shows diminished fluorescence for a 30 ms pulse duration, suggesting that cytodisruption is coupled with persistent cytoskeleton disruption. These observations are consistent with reports for other systems that LIPUS disrupts the cellular cytoskeleton [59, 66]. In contrast, with 1 ms pulse duration, the actin cytoskeleton appears unchanged from the negative control. Mittelstein *et al.* [54] conclude that these observations suggest that LIPUS induces actin cytoskeletal disruption and activates apoptotic cell-death pathways.

In the present work, we argue that these competing mechanisms of cytoskeletal disruption and self-repair, when coupled to the—possibly resonant—dynamics of the cells over many insonation cycles, underlie the oncotripsy observations of Mittelstein *et al.* [54]. Based on this hypothesis, we develop a plausible theoretical model of oncotripsy that accounts for several of the key experimental observations of Mittelstein *et al.* [54], including the dependence of the cell death rates on frequency, pulsing characteristics and number of cycles. The goals are to explain the mechanism of resonance of cells in suspension theoretically, determine the control parameters for the low-intensity focused ultrasound, and predict the bounds in which cancerous cell death is likely. We posit that, under the conditions of the experiments, cells in suspension subjected to LIPUS act as frequency-dependent resonators and that the evolution of the cells is the result of competing mechanisms of high-cycle cumulative damage and healing of the cytoskeleton. We recall that structural materials can fail at load levels well below their static strength through processes of slow incremental accumulation of damage when subjected to a large number (millions) of loading cycles, a phenomenon known as *mechanical fatigue* [74]. Likewise, whereas one single LIPUS pulse is unlikely to cause significant cytoskeletal damage, we posit that over millions of cycles damage can accumulate to levels that render the cell unviable and cause it to die. By analogy to structural materials, we refer to the hypothesized necrosis mechanism as *mechanical cell fatigue*.

We note that, whereas the elasticity, rheology, and remodeling of the cytoskeleton have been extensively studied in the past (cf., e. g., [18, 33, 47, 56]), no model of cumulative damage and mechanical cell fatigue appears to have been as yet proposed. The model proposed in this work follows as an application of cell dynamics, statistical mechanical theory of network elasticity, and 'birth-death' kinetics to describe processes of damage and repair of the cytoskeleton. We also develop a reduced

dynamical model that approximates the three-dimensional dynamics of the cell and facilitates parameter studies, including sensitivity analysis and process optimization. The reduced dynamical system encompasses the relative motion of the nucleus to the cell membrane and a state variable measuring the extent of damage to the cytoskeleton. The cell membrane is assumed to move rigidly according to the particle velocity induced in the water by the insonation. The dynamical system evolves in time as a result of structural dynamics and kinetics of cytoskeletal damage and repair. The resulting dynamics are complex and exhibits behavior on multiple time scales, including the period of vibration and attenuation, the characteristic time of cytoskeletal healing, the pulsing period and the time of exposure to the ultrasound. We show that this multi-time scale response can adequately be accounted for by recourse to Wentzel–Kramers–Brillouin (WKB) asymptotics and methods of weak convergence. We also account for cell variability and estimate the attendant variance of the time-to-death of a cell population using simple linear sensitivity analysis. The reduced dynamical model predicts, analytically up to quadratures, the response of a cell population to LIPUS as a function of fundamental cell properties and process parameters. We show, by way of partial validation, that the reduced dynamical model indeed predicts—and provides a conceptual basis for understanding—the oncotripsy effect and other trends in the data of Mittelstein *et al.* [54], including the dependence of cell-death curves to pulse duration and duty cycle. Finally, employing the reduced model, we explore a practical application of the theory by creating bounds on the parameters for LIPUS that guarantee the demise of the cancerous cell while keeping healthy cells intact.

Chapter 2

EXPERIMENTAL BASIS ON ONCOTRIPSY

In the last years, low-intensity ultrasound has gained attention for its potential in therapies that promote physiological processes without significant changes in temperature. Bone healing, neural stimulation, and enhancement of drug uptake are just some of the possible applications. Low-intensity pulsed ultrasound (LIPUS) is a form of ultrasound delivered at low intensities (<3mW/cm^2) and in pulses that control the dosage of acoustic energy deposited. The ultrasound is described in terms of its pressure (or intensity), frequency, duty cycle, pulse length, and exposition time. Figure 2.1 and Figure 2.2 show schematics of these measures. On a pulsed wave, the duty cycle refers to the ratio of time the ultrasound is ON between the beginning of two consecutive pulses. The ON time is known as the pulse duration, and the OFF time as the listening time. The number of pulses in the exposure time, i.e., over the length of the experiment, is known as the pulse repetition frequency.

Following the leads on the oncotripsy effect, Mittelstein *et al.* [54] have designed laboratory tests involving several cancerous cell lines in aqueous suspension under LIPUS. In this chapter, we present a brief summary of the experimental system they developed, as well as data and observations resulting from the study that are directly relevant to the present work. Their original publication may be consulted for a complete account.

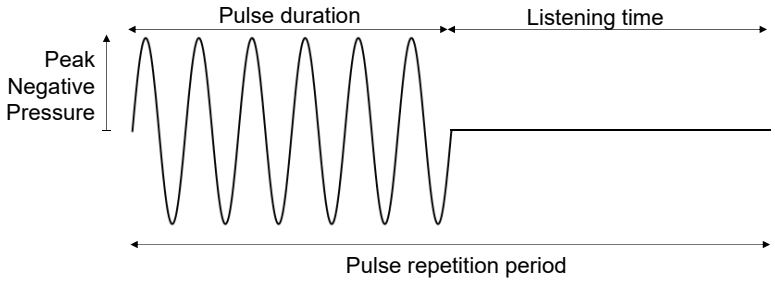

Figure 2.1: Schematic of pulsed ultrasound period.

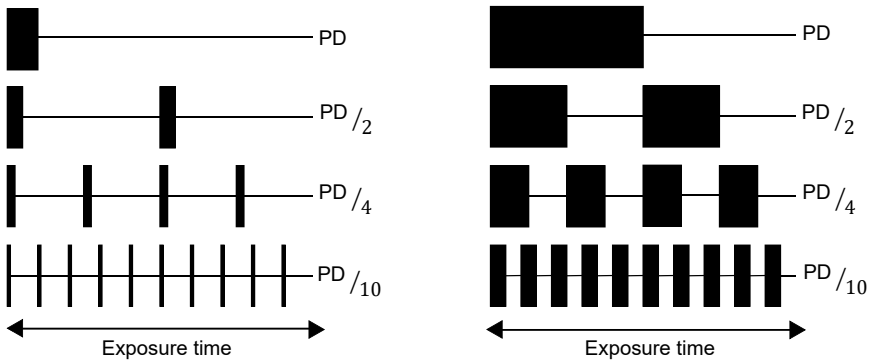

(a) (b)

Figure 2.2: Schematic of pulsed ultrasound period for different pulse durations and two duty cycles (DC). (a) DC=10%. (b) DC=50%.

2.1 Experimental system

In order to best proceed in understanding the nature of oncotripsy, we begin by first describing the experimental setup that will allow us to excite the system of interest and provide data for analysis. The experimental setup, Fig. 2.3a, was developed to investigate the response of cells in aqueous suspension to ultrasound insonation.

Mittelstain *et al.* [54] placed suspension cells within a mylar film pocket that is submerged in a water bath. The cells then mantain acoustic contact with the

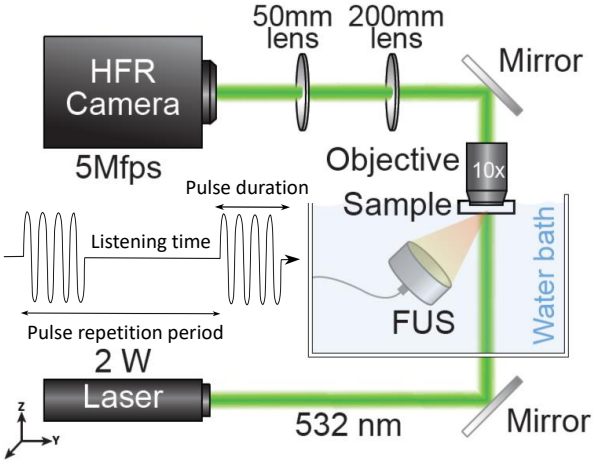

Figure 2.3: Experimental setup of Mittelstein *et al.* [54]. Schematic drawing of the LIPUS system and high frame-rate camera setup enabling cellular imaging at a frame rate of 5 MHz. (HFR: high-framerate. FUS: focused ultrasound.) Inset: Schematic of pulse duty cycle.

ultrasound transducer. Their investigation indicates that the cell disruption effect, seen through low-intensity pulsed ultrasound (LIPUS), requires the presence of spatial standing waves. Such waves are generated by the reflection of the ultrasound wave off of an acrylic or metal acoustic reflector. Several hypotheses were proposed within referenced paper to justify this observed requirement, but they fall outside the scope of this thesis. In summary, under the effect of standing waves, the cytodisruption was significantly higher than without them. In tests without the standing wave and double PNP (Peak Negative Pressure), the level of cytodisruption was still substantially lower. Additionally, they observed that, only under the effect of standing waves, the cells generated both stable and inertial cavitation, which acted as local amplifiers of the acoustic pressure and cytodisruption effect. They suggested that the presence of standing waves and cavitation is required for cell death to happen. However, cavitation is not a sufficient condition on cell killing, as peripheral blood mononuclear cells (PBMCs) generate similar cavitation to the other tested cells, and were not strongly disrupted by LIPUS.

The transducer in the water tank is positioned directly adjacent to the mylar pocket such that the acoustic axis is perpendicular to the optical axis, which illuminates the sample via laser light. The mylar pocket is supported by a three-sided acrylic frame with one of the three sides serving as an acoustic reflector to induce the required standing waves. A water immersion pan-fluor objective is lowered into a water bath, and a series of prism mirrors and converging lenses deliver the image into a high-speed camera. Images are acquired 100 ms after the arrival time of the pulse, to observe the effect of prolonged ultrasound exposure.

The experiments performed to investigate the oncotripsy theory aim to isolate the mechanical effects of ultrasound from other bioeffects, and thus prevent local heating. To maintain low-intensity ultrasound conditions (Ispta < 5 W/cm2), pulsed ultrasound tests were performed, as shown in Fig. 2.4a. LIPUS was applied at a 10% duty cycle; however, the pulsing parameters were varied to investigate their role on ultrasound cytodisruption. The pulse duration corresponds to the length of each pulse during which the ultrasound is active. By varying the pulse duration, while maintaining a constant duty cycle, the pulsing pattern of the ultrasound applied to the cells can be modified while maintaining constant acoustic energy deposition within the cells. To further investigate the effects of changing ultrasound parameters on cytodisruption, three different transducers that operate at 300 kHz, 500 kHz, and 670 kHz were used during this investigation. To provide consistent comparisons,

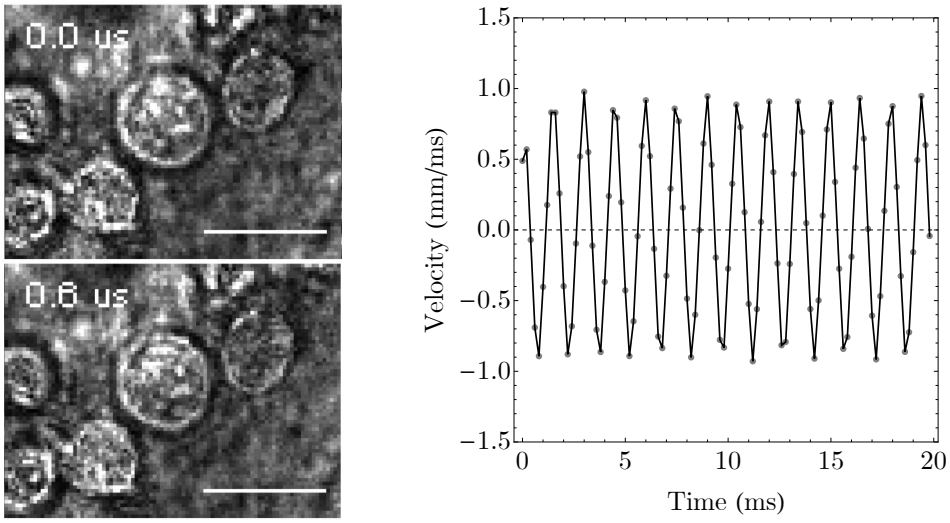

(a) (b)

Figure 2.4: a) Typical high frame-rate camera recordings showing minimal K-562 cell drift after 100 ms of 670 kHz ultrasound exposure (scale bar 20 microns). b)Measured velocity of K-562 cell under an incident plane wave of pressure amplitude $P_0 = 1.4$ MPa and excitation frequency $f_0 = 670$ kHz. Video captured by Mittelstein *et al.* [54] and processed with Ncorr[8] (scale bar 10 microns).

they were configured to produce a negative peak pressure of 0.7 MPa at their focus in free water.

Cell motion

Recordings from experiments show that the entire field-of-view oscillates in the direction of ultrasound propagation (see Fig. 2.4a). The observed membrane deformation was minimal, which is consistent with the damping expected for the exceedingly low Reynolds number characteristic of cells in aqueous suspension. Fig. 2.4b shows the measured trajectory of a K-562 cell upon insonation of focal pressure of $\bar{P}_0 = 2P_0 = 1.4$ MPa, frequency f_0=670 kHz and wavelength $\lambda = 2.2$ mm. As may be seen from the figure, the cell undergoes an ostensibly harmonic motion. The period of the motion is $T = 1.4$ μs, which corresponds to a frequency of $f = 714$ kHz. In addition, the amplitudes of the motion in the x- and y-directions are $u_x = 0.23$ μm and $u_y = 0.022$ μm, respectively, for a total displacement amplitude of $u = \sqrt{u_x^2 + u_y^2} = 0.231$ μm and a velocity amplitude of $v = 2\pi f u = 1.037$ m/s. By way of reference, the particle velocity amplitude of the medium is $v_0 = \bar{P}_0/\rho_0 c_0 = 0.97$ m/s, where $\rho_0 = 1000$ Kg/m^3 is the mass density of water and $c_0 = 1450$ m/s is its sound speed. We thus conclude that, as expected for the long wavelength of the insonation relative to the cell size, the cells move

Cell Line	Morphology	Tissue	Disease	Source
K-562	Lymphoblast	Lymphocyte	Chronic myeologeneous leukemia	Human cell line
U-937	Monocyte	Lymphocyte	Pleura/pleural effusion, lymphocyte, myeloid	Human cell line
T-Cells	Lymphocyte	Peripheral blood cells, isolated CD3+		Human primary cells

Table 2.1: Haematopoietic and lymphoid malignancies tumor cells used in the experiments of Mittelstein *et al.* [54] classified by morphology, type and disease.

ostensibly at the particle velocity of the fluid.

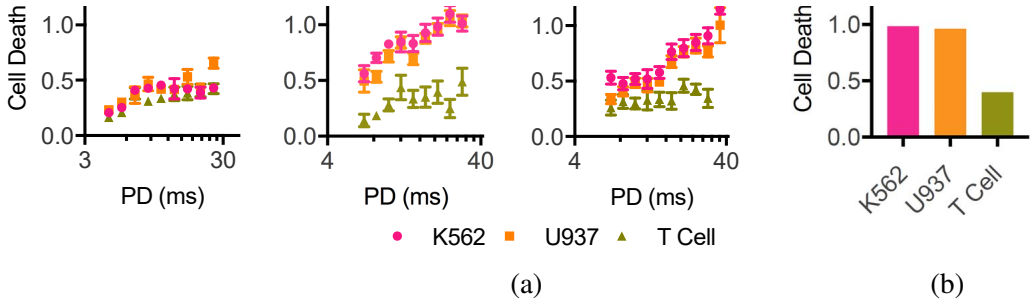

(a) (b)

Figure 2.5: Tests of cancerous K562 and U937 cells and healthy CD4 T-cells at a PNP of 0.7MPa and a time of exposure of 60 seconds, showing the effect of frequency and pulse duration on cell death rates. In call cases, the pulse duration is 10% of the total pulse repetition period. (a) Cell death fraction vs pulse duration, and (b) cell death fraction at 20 ms pulse duration vs type. Reproduced from [54].

Cell-death data

The experimental study of Mittelstein *et al.* [54] observed that LIPUS conditions at specific frequencies and pulsing parameters can achieve cell selective cytodisruption. This capability to tune ultrasound parameters to cause selective disruption in cancer cells while sparing healthy cells is a novel finding, and fits with many of the predictions of the oncotripsy project. The morphology, type, and related disease for each cell line are listed in Table 2.1.

Figure 2.5 demonstrates that cells can have a varied response to ultrasound based upon the ultrasound waveform. All data points in this figure represent cell death assessed using LIVE/DEAD assays after exposure to an equal dosage of acoustic

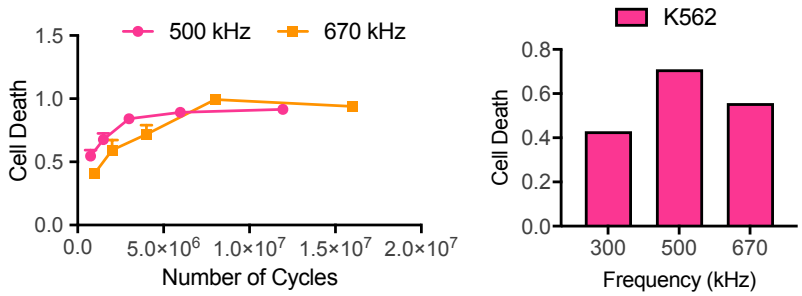

(a) (b)

Figure 2.6: Tests of cancerous cell K562 at a free field pressure of 0.7 MPa, pulse duration of 100 ms and duty cycle of 10%, showing the effect of frequency and number of cycles. (A) Cell death vs number of cycles (B) Cell death at 1.8 million cycles. Unpublished data from Mittelstein *et al.* [54].

energy, though administered with different signal frequencies and pulse durations. These tests were all performed on cells in suspension for an exposure time of 60 seconds, a duty cycle of 10%, and in a spatial standing wave setup with a free field pressure of 0.7 MPa. Remarkably, high cell-death rates are observed for both the cancerous K-562 and U937 lines at 500 kHz signal frequency and 20 ms pulse duration while, under identical conditions, the control T-cells remain nearly unaffected (see Fig. 2.5b). As a frequency-dependent resonant response, these observations bear out the oncotripsy effect —and its associated selective lethality— for cells under harmonic excitation. The data in Fig. 2.5 also shows a strong dependence of the cell response on pulse duration, with cell death enhanced at higher pulse durations. We take this dependence to suggest that the cell response is the result of two competing effects with vastly different characteristic times: damage accumulation during the on-part of the cycle and cell repair and healing during the entire time of exposure. The efficiency of the duty cycle may then be expected to depend sensitively on the relative values of the pulsing period and the characteristic times for damage accumulation and healing.

Figure 2.6 shows data from tests of cancerous K562, that we will model as being exposed to acoustic pressure waves with a peak negative pressure of 0.7 MPa in free water and a pulse duration of 100 ms, showing the effect of frequency and the number of cycles. In all cases, the pulse duration is 10% of the total pulse repetition period, or a duty factor of 0.1. As may be seen from these figures, cell death does not occur instantly but requires a certain exposure time to occur. We take this observation to suggest that death occurs by a process of damage accumulation

over many insonation cycles. It is also evident from the figures that some cells die relatively early whereas others require considerably large number of cycles to die. These observations are suggestive of a broad variability in the susceptibility of the cell population to LIPUS.

2.2 Discussion of experimental outcomes and concluding remarks

The oncotripsy effect is based on the hypothesis that differences in mechanical properties and geometries of normal and abnormal cells can be exploited to target the latter at their resonance frequency to break them down.

Mittelstein *et al.* [54] built an oncotripsy experiment set up to test this hypothesis. In agreement with this concept, the experiments confirm that the application of LIPUS can result in high death rates in the cancerous cell population at certain frequencies with low death rates among healthy cells. The death and survival rates depend critically on the parameters of the ultrasound, such as frequency and pulse duration, indicative of the dynamical response of the cells.

The cause of cell death in the experiments is still unknown, but through confocal microscopy, it was shown that the cytoskeleton undergoes a persistent disruption during LIPUS (see Fig.1.5). The issue of cavitation in Mittelstein *et al.* [54] is intriguing and should be explored in further computational research. Cavitation, as the process of mechanically-driven vaporization, is of stochastic nature and could be extra or intracellular. A spectrogram of the scattered signal showed significant cavitation at high pulse duration or high focal pressures, but only in the presence of cells. It could be indicative that cells could act as impurities in the media, increasing the probability of bubble formation. Interestingly, among all the cells tested, cell death has not been observed for PBMCs. Finally, the final cause of cell-death could be an interplay between oncotripsy and cavitation.

Chapter 3

FREQUENCY RESPONSE OF WHITE BLOOD CELLS

In this chapter, we study the frequency response of cancerous and healthy cells. The experiments by Mittelstein *et al.* [54] show through high-speed camera recordings a cell oscillating in the direction of the ultrasound propagation with minimal observable cell membrane deformation. Furthermore, cancerous cells under the influence of a harmonic excitation, with constant energy intensity, have a higher cell-dead fraction at 500kHz than at any other neighboring frequency. This observation suggests that the driving force is working in the range of the natural cellular frequency. Based on experimental observations of a dense and stiffer nucleus, we hypothesize that this natural frequency is the first longitudinal mode of the cell, in which the nucleus acts as a resonator.

This chapter is organized as follows. First, we review the mechanical properties and morphologies of the white blood cells involved in the experiments of Mittesltein *et. al.* [54]. Second, we perform a finite element modal analysis on these cells with varying elasticity, nucleus, and cell sizes, and make observations on their influence of the natural frequencies of the cell. Finally, we calibrate the shear modulus of a cancerous and healthy cell to the experiments and analyze the highest modal stresses and strains location.

3.1 Histology of white blood cells

In this section, we explain the morphology, dimensions, and shape of healthy and cancerous white blood cells (WBC). The first subsection is concerned with the different types of WBC and their typical characteristics, whereas the second one is a review of the mechanical properties and morphology of cancerous white blood cells.

White blood cells morphology, dimensions and shape

Blood is composed of the plasma and blood cells, with the latter divided into three major groups: red blood cells (RBC) or erythrocytes, white blood cells (WBC) or leukocytes, and platelets or thrombocytes. The primary function of the first group is to transport oxygen and release it into tissues and conforms by number the most substantial elements in the blood. White blood cells are part of the immune system

and are present in a ratio of 1 WBC to 500-1000 RBC [23].

WBC are found not only in the bloodstream but also in tissues. In the body, they can be shaped differently, but in suspension, these cells become almost spherical. They are conformed by cytoplasm and nucleus, being the latter the densest constituent of the cell. In adults, RBC and platelets are non-nucleated, while the size and number of the nucleus in WBC depend on the type.

Based on the characteristics of their constituents, WBC can be classified into two groups: (1) granular cells, granulocytes or polymorphonuclear leukocytes, and (2) non-granular cells, or mononuclear leukocytes [23]. In the first group, granules — small particles released as an immune response — can be found throughout the cytoplasm, and the nucleus is lobed or segmented. In the second group, instead, there are no granules, and there is only one defined nucleus.

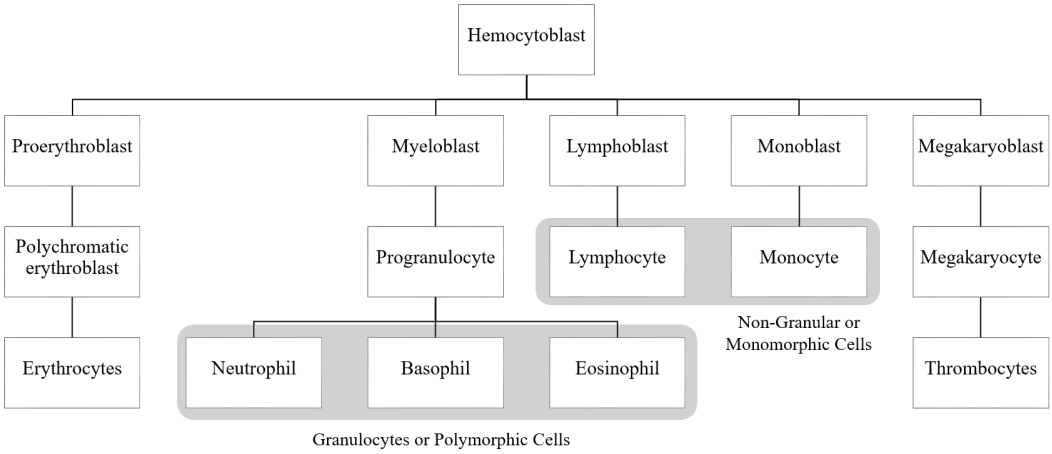

Figure 3.1: Blood Cells Development

Granulocytes or polymorphic cells

- *Neutrophil*. It is the leukocyte that is in blood in the largest concentration [1]. Its diameter varies between 10 to 12 μm. The granules are fine and evenly distributed throughout the cell. The nucleus shape depends on the stage of life, and transitions from an unsegmented cylindrical or banana-shaped nucleus, to a segmented form of two to five lobes, joined by a nuclear filament [23].
- *Eosinophil*. Its diameter varies between 10 to 14 μm, and it is very fragile. The nucleus of the eosinophil is larger but less dense than the neutrophil, and it evolves from an unsegmented band to a two-lobed or three-lobed form [23]. The granules are 1μm length-ovoids.

- *Basophil*. Its the smallest of the granulocytes, with a diameter between 8 to 10 μm. It also is the one with the least concentration in human blood [1]. The nucleus has an irregular shape, and the granules vary in size (0.5-1μm) and closely packed [23].

Non-Granular or monomorphic cells

- *Lymphocytes*. These cells are divided into two main groups due to their variability in size, though no clear division exists between both: small and large lymphocytes. The large lymphoblast is about 13.5μm, and it has one large spherical, ovoidal, or bean-shaped nucleus [23]. The small lymphoblast varies in size from 6μm to 8μm, and it also has one large spherical nucleus, which frequently has a small indentation [23]. Lymphocytes can also be divided in subtypes B and T, with the first ones making antibodies and the latter killing infected cells and regulating other white blood cells.

- *Monocytes*. According to the shape of their nucleus, these cells are divided into monocytes and the *transitional cell*. The first ones vary in size from 16 to 22 μm with a very irregular surface, and the nucleus is “spherical, ovoidal, slightly indented, or bean- or kidney-shaped" [23]. The transitional cell is larger than the monocyte, with a usual size of at least 20μm and an elongated, twisted, and E-shaped nucleus.

White blood cells lines type, size and mechanical properties

Leukemia is a type of cancer that starts in blood-forming tissue, whereas Lymphoma starts in the lymphatic system. Both of them involve white blood cells (WBCs). In our study, we used T-Cells, K-562, and U-937, which are WBCs from the family of the Non-Granular or Monomorphic Cells. The morphology, type, and related disease for each cell line can be seen in Table 3.1.

Morphology A criterion for malignancy is the size difference between normal nuclei, with an average diameter of 7 to 9 microns, and malignant nuclei, which can reach a diameter of over 50 microns [7]. Early studies [25] showed that the nuclear-nucleolar volume ratios in healthy tissues and benign as well as malignant tumors, do not differ quantitatively. Nucleoli volumes of normal tissues, however, are found to be significantly smaller than the volume of nucleoli in cancerous tissues [25]. In the family of haematopoietic and lymphoid malignancies tumor cells,

Cell Line	Morphology	Tissue	Disease	Source
K-562	Lymphoblast	Lymphocyte	Chronic myeologeneous leukemia	Human cell line
U-937	Monocyte	Lymphocyte	Pleura/pleural effusion, lymphocyte, myeloid	Human cell line
T-Cells	Lymphocyte	Peripheral blood cells, isolated CD3+		Human primary cells

Table 3.1: Haematopoietic and lymphoid malignancies tumor cells used in the experiments of Mittelstein *et al.* [54] classified by morphology, type and disease.

Downey *et al.* [17] measured cell size with a flow cytometer, and reported mean diameters of 8.3±0.05 μm, 6.05±0.039 μm and 8.13±0.042 μm for neutrophils, lymphocytes and monocytes, respectively. In the same veins, Rosenbluth et al. [65] found diameters of 12.4±1.2 μm for HL60 (myeloid cells), 11.5±1.5 μm for Jurkat, an acute lymphoblastic T-cell leukemia cell line, and 8.3±0.6 μm for neutrophils. Li et al. [45] measured the diameter of K-562 to be 28 μm, much larger than the size of normal lymphocytes (6-20μm) and neutrophils (10-12 μm). The ratio of nucleus-to-cell differs among cells, but in resting lymphocytes, the cell is mostly occupied by its nucleus*et al.* [53]. The average volume of lymphocytes is 130 μm^3 and for neutrophils 300 μm3 [53]. Zipursky *et al.* [86] measured the density of monocytes (1.067-1.077 g/ml) and lymphocytes (1.073-1.077 g/ml) and found that 70% of the patients with acute leukemia had high-density lymphoblast.

Mechanical properties The mechanical properties of various cell components are found to vary significantly in healthy and diseased tissues. Cross *et al.* [13], investigated the stiffness of live metastatic cancer cells using atomic force microscopy, showing that cancer cells are more than 70% softer than healthy cells. Other cancer types, including lung, breast, and pancreas cancer, display similar stiffness characteristics. Using magnetic tweezers, Swaminathan *et al.* [76] found that cancer cells with the lowest invasion and migratory potential are five times stiffer than cancer cells with the highest potential. Likewise, increasing stiffness of the extracellular matrix (ECM) promotes hepatocellular carcinoma (HCC) cell proliferation, thus being a strong predictor for HCC development [70]. Enhanced cell contractility due to decreased matrix stiffness results in an enhanced transformation of mammary epithelial cells [64]. By contrast, a decrease in tissue stiffness impedes malignant

growth in a murine model of breast cancer [43]. Various experimental techniques have been employed to characterize the material properties of individual cell constituents in both healthy and diseased tissues. Kim *et al.* [37] estimated the elastic moduli of both cytoplasm and nucleus of hepatocellular carcinoma cells based on force-displacement curves obtained from atomic force microscopy. Increased compliance of cancerous and pre-cancerous cells was reported by Furhmann *et al.* [21], who used atomic force microscopy to determine the mechanical stiffness of normal, metaplastic, and dysplastic cells, showing a decrease in the Young modulus from normal to cancerous cells. The inhomogeneity in stiffness of the living cell nucleus in normal human osteoblasts has been investigated using a non-invasive sensing system Konno *et al.* [38]. These measurements show that the stiffness of the nucleolus is three times larger than other nuclear domains. Dahl *et al.* [14] measured the network elastic modulus of the nuclear envelope, independently of the nucleoplasm, using micropipette aspiration. Their measurements suggest that the nuclear envelope is much stiffer and stronger than the plasma membranes of cells.

With the use of atomic force microscopy (AFM), Rosenbluth *et al.* [65] compared the deformability of leukemia cells at low deformation rates. Fitting the experimental data to a Hertzian contact model, they obtained an apparent stiffness of 855±670 Pa for HL60 (myeloid cells), 48±35 for Jurkat cells, and 156±87 for neutrophils at 25^oC. Using a liquid droplet model, they obtained a cortical tension of 155±81 pN/μm, 21±13 pN/μm, and 48±20 pN/μm for the HL60, Jurkat and neutrophil, respectively. Thompson *et al.* [78] found that, for indentations higher than 0.5 microns, the average Young modulus is 130 Pa for U-937, a diffuse large B-cell lymphoma cell line, and 40 Pa for Jurkat when they fit the atomic force microscopy curves data to a Hertzian contact model. By a similar procedure, Li *et al.* [45] obtained a Young modulus of 0.2-0.4 kPa for Raji cells, a Burkitt's lymphoma cell line, and 0.6-0.7kPa for K-562. Downey *et al.* [17] measured the deformability of leukocytes using a cell poker at 20^oC, and found out that lymphocytes and monocytes are stiffer than neutrophils. Their force-displacement curves reported values of approximately 0.06 mdyn/μm (600 pN/μm) for neutrophils, 0.095 mdyn/μm (950 pN/μm) for lymphocytes, and 0.14 mdyn/μm (1400 pN/μm) for monocytes. Zhou *et al.* [85] obtained the elastic modulus of leukocytes through the rate-jump optical-tweezers indentation method. This method yields a stiffness that is rate-independent. The authors reported values of elastic modulus of approximately 68 Pa for K-562, 130 Pa for the K-562 nucleus, 92 Pa for HL-60, 45 Pa for macrophages, 30 for monocytes, and 19 for granulocytes.

Numerous experimental studies have additionally suggested that the material behavior of the different cell constituents is viscoelastic. Schmid-Schönbein *et al.* [69] analyzed neutrophils stiffness employing micropipette aspiration experiments and fitted the data to a standard linear solid viscoelastic model of the cell. The study generated a long-term stiffness of k_1 = 275±119 dyn/cm^2 and a stiffness of k_2 = 737±346 dyn/cm^2 and a viscosity of μ=130±54 dyn-s/cm^2 for the Maxwell element. They additionally report that monocytes and eosinophils fall in the same range. Based on particle-tracking microrheology, Panorchan *et al.* [63] determined the viscoelastic properties of the cytoplasm of human umbilical vein endothelial cells. Using micropipette aspiration techniques, Guilak *et al.* [24] quantified the viscoelastic properties of isolated nuclei of articular chondrocytes and found that the nucleus is almost twice as viscous as the cytoplasm. In an investigation involving both cancerous and healthy cells, Zhang *et al.* [84] showed that human hepatocytes and hepatocellular carcinoma cells have approximately identical viscoelastic properties. Measurements of individual cytoskeletal biopolymers have been presented by Janmey [32], where the stress versus strain response and storage modulus are reported for three primary cytoskeletal fibers.

3.2 Frequency response

This section is concerned with the computation of the modal vectors and the effective mass of the first longitudinal mode of vibration of the cell-nucleus system. First, we study the influence of the mechanical properties and their size on the eigenfrequencies. Second, we analyze the modal stresses and strains of a healthy and cancerous cell.

The finite element model and analysis presented in this section are carried out in ABAQUS [15].

Parameter analysis

To study the sensitivity of the cell longitudinal mode to the mechanical properties and size, we build several finite element models with varying sizes and stiffnesses. We assume the cell to be spherical and composed by their major constituents: cytoplasm and a concentric nucleus, and we neglect the effect of the plasma membrane, nuclear envelope, and other organelles.

Neglecting viscous effects, we model the cell constituents to follow a Neo-Hookean strain energy density. We consider three different cell radii: 4.5μm, 9μm and 18μm, with nucleus-to-cell ratio constant. At constant cell diameter of 9 μm, we study

three different nucleus diameters: 3.6, 5.4, and 7.2 μm, equivalent to 0.06, 0.2, and 0.5 nucleus-to-cell volume ratios. Owing to the large variability of shear modulus reported, we vary the shear modulus of the constituents in the range 50Pa to 50kPa. For these computations, we consider the cells to be almost incompressible and set the poisson ratio to 0.45 .

The results of the parameter analysis are presented in Figure 3.2. The plots indicate that, under all the combinations under study, the first longitudinal mode varies within the range 20kHz to 1.5MHz. A closer inspection shows that a stiffer cytoplasm and nucleus result in a higher natural frequency, independently of the size and nucleus-to-cell ratio. At decreasing nucleus-to-cell ratio (Fig. 3.2a and b) or smaller cells (Fig. 3.2c and d) the frequency of resonance increases.

Eigenfrequencies and eigenmodes of a healthy and cancerous cell

In this subsection, we study the behavior of a cancerous cell and a healthy cell. For these computations, we consider the cell to be spherical with an average diameter of 18μm and a concentric nucleus of 9μm. For simplicity, we assume that healthy and cancerous cells to have the same size. Owing to the symmetric nature of the problem and that we are only interested in the translational mode of vibration, we build an axisymmetric model of the cell with 1740 hybrid elements. The cell geometry, as used in the finite element calculations, is shown in Fig. 3.3.

The effective shear modulus is recovered from the experimental paper by Mittelstain *et al.* [54]. We refer to the frequency tests in Fig. 2.6 showing a peak in a cancerous cell-dead fraction at 500kHz, and we hypothesize that this behavior is due to a translational eigenmode of the nucleus.

Based on experimental evidence suggesting the nucleus to be 5 to 10-folds stiffer than the cytoplasm [40], we infer the nucleus stiffness. For the bulk modulus of the constituents, we resort to small-strain elastic moduli conversion for the Poisson ratio of 0.45. The density is 1.5 g/cm^3 for the nucleus and 1 g/cm^3 for the cytoplasm [29]. Furthermore, following [29], we introduced the *cancerous potential* as a scaling factor for the nucleus and cytoplasm according to

$$p_{cell} = p_{cell} + (1 - \chi)p_{cell}, \tag{3.1}$$

where p refers to the material parameter, and carcinogenic potential χ of 100% corresponds to the cancerous cell. The calibrated material properties of the cancerous

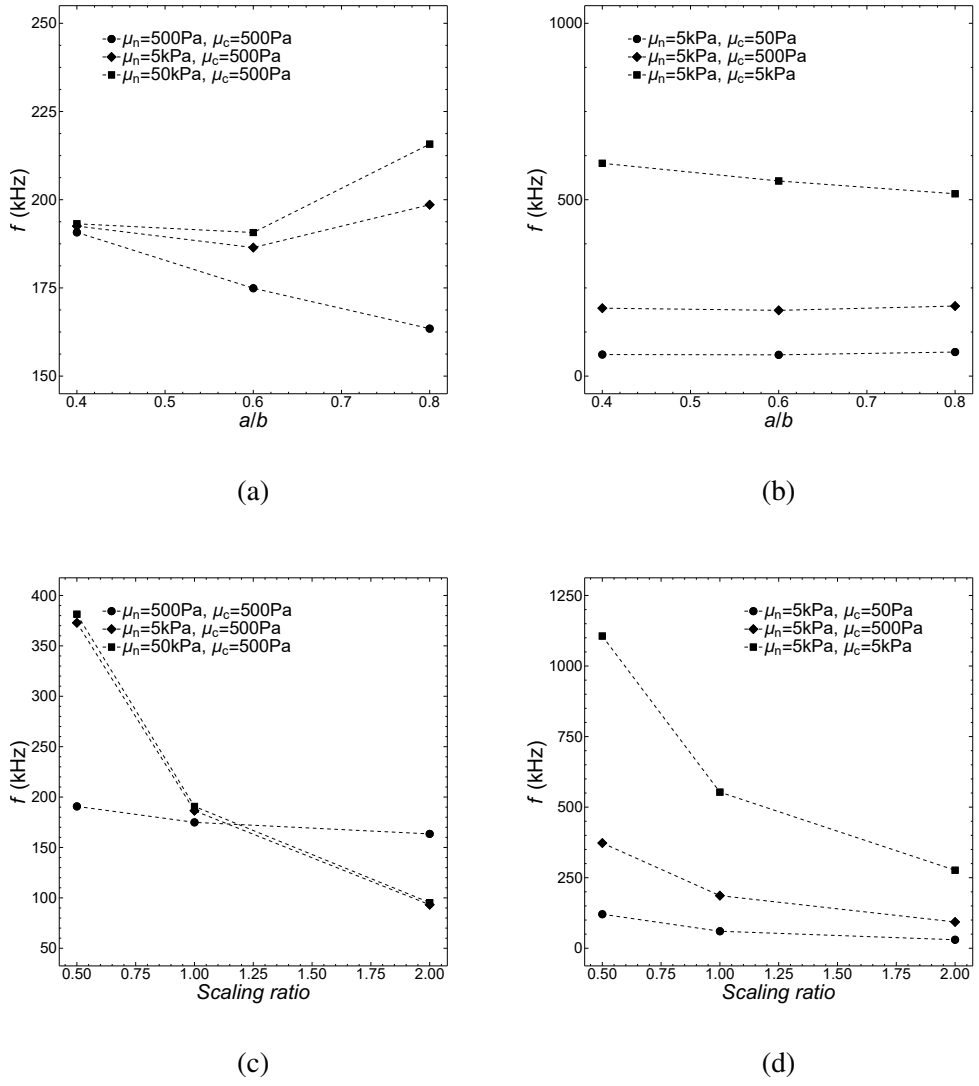

Figure 3.2: Influence of elasticity and size on the first translation eigenfrequency. a) Effect of nucleus stiffness at constant cytoplasm shear modulus for varying nucleus-to-cell ratio a/b; b) effect of cytoplasm stiffness at constant nucleus shear modulus for varying nucleus-to-cell ratio a/b; c) effect of nucleus stiffness at constant cytoplasm shear modulus for varying cell size (scaling 1 refers to a=5.4μm and b=9μm); and, d) effect of cytoplasm stiffness at constant nucleus shear modulus for varying cell size (scaling 1 refers to a=5.4μm and b=9μm).

and healthy cells ($\chi = 0.2$) are collected in Table 3.2.

Figure 3.4 presents the three eigenfrequencies with the highest effective mass contribution in the longitudinal direction for cells with different cancerous potential. On average, the first two eigenfrequencies corresponds to ~60% of the modal mass,

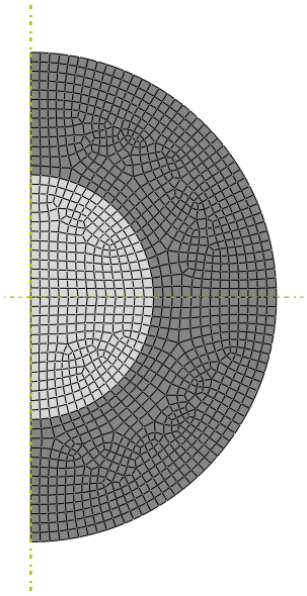

Figure 3.3: Geometry and mesh used in the modal analysis of a cancerous and healthy cell.

and the third mode to ~10%. As can be seen in the figure, the first eigenmode of the most cancerous cell is 500kHz. As the cancer potential decreases, the cell becomes stiffer, which increases the frequency of resonance of the cell. The gap between the most cancerous and healthy cells is 110kHz for the first eigenmode, 230kHz for the second, and 450kHz for the last one.

Contours plots of modal displacements, stresses, and strains for the cancerous cell are shown in Fig. 3.5, Fig. 3.6, and Fig. 3.7. The contours show that the distribution of stresses and strains is heterogeneous. The stresses will be mostly compressive and tensile along the nucleus direction of motion. In addition, high shear stresses are expected next to the nucleus. Similar results can be identified for the strains.

Table 3.2: Calibrated material properties of a cancerous (μ_c) and healthy (μ_h) cell

	μ_h	μ_c	ν
Cytoplasm	0.015 MPa	0.0225 MPa	0.45
Nucleolus	0.15 MPa	0.225 MPa	0.45

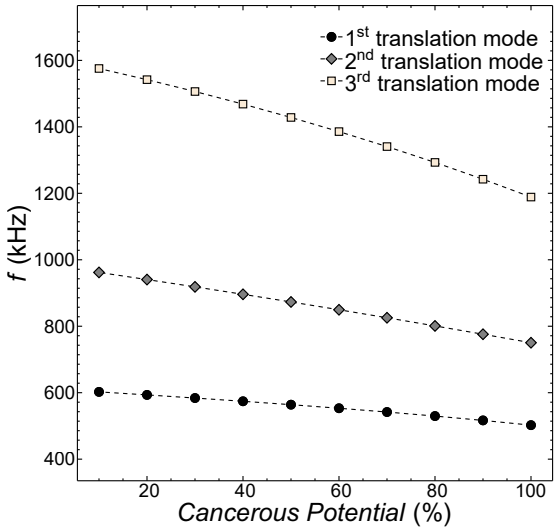

Figure 3.4: Geometry and mesh used in the modal analysis of a cancerous and healthy cell.

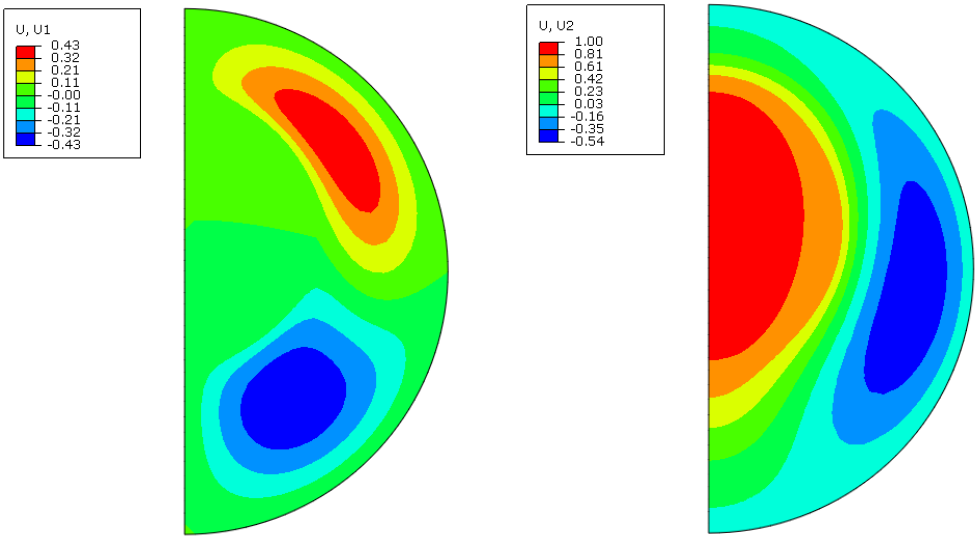

(a) (b)

Figure 3.5: Modal displacements for a cancerous cell at the principal longitudinal mode f=500kHz.

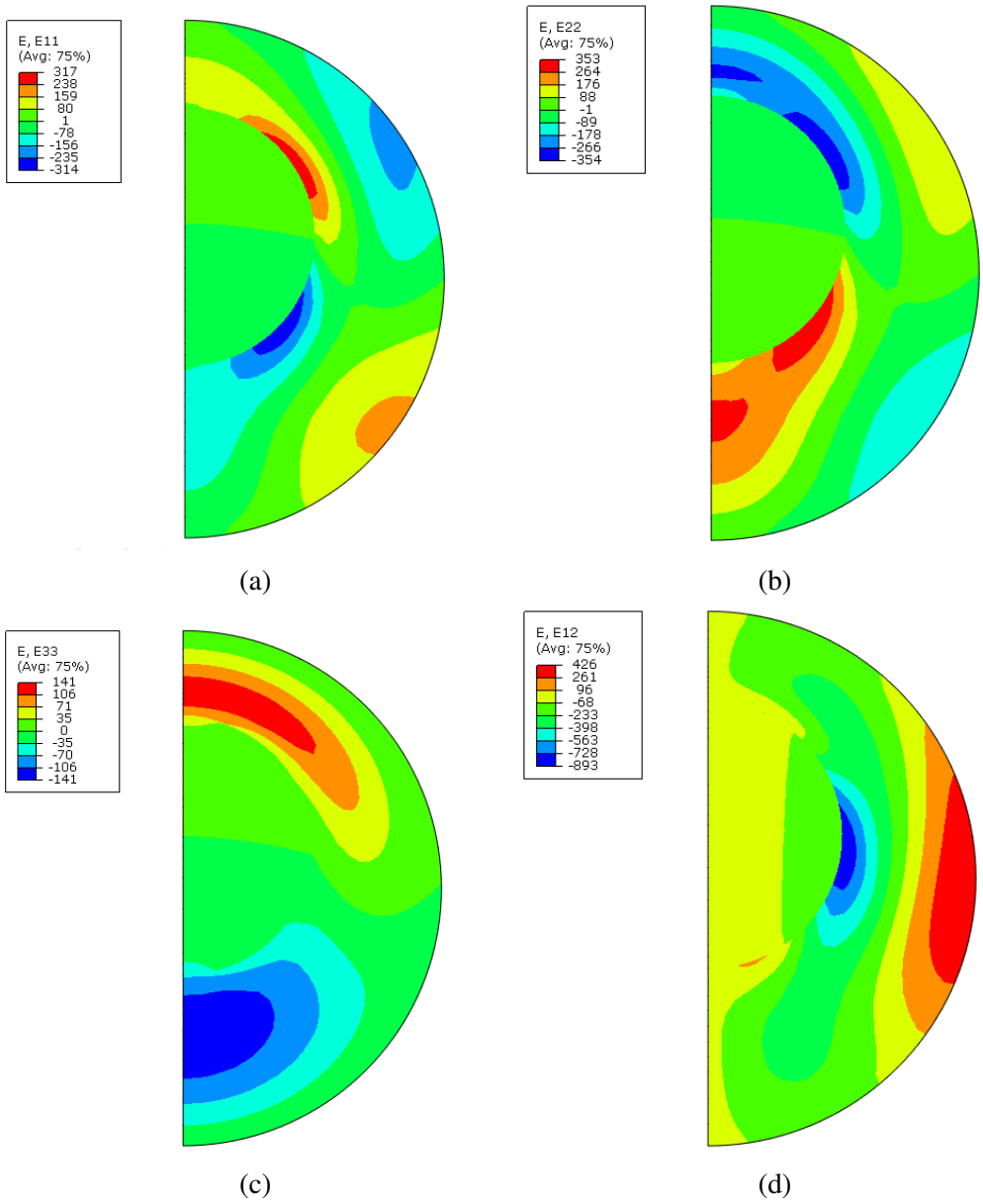

Figure 3.6: Modal strains for a cancerous cell at the principal longitudinal mode f=500kHz.

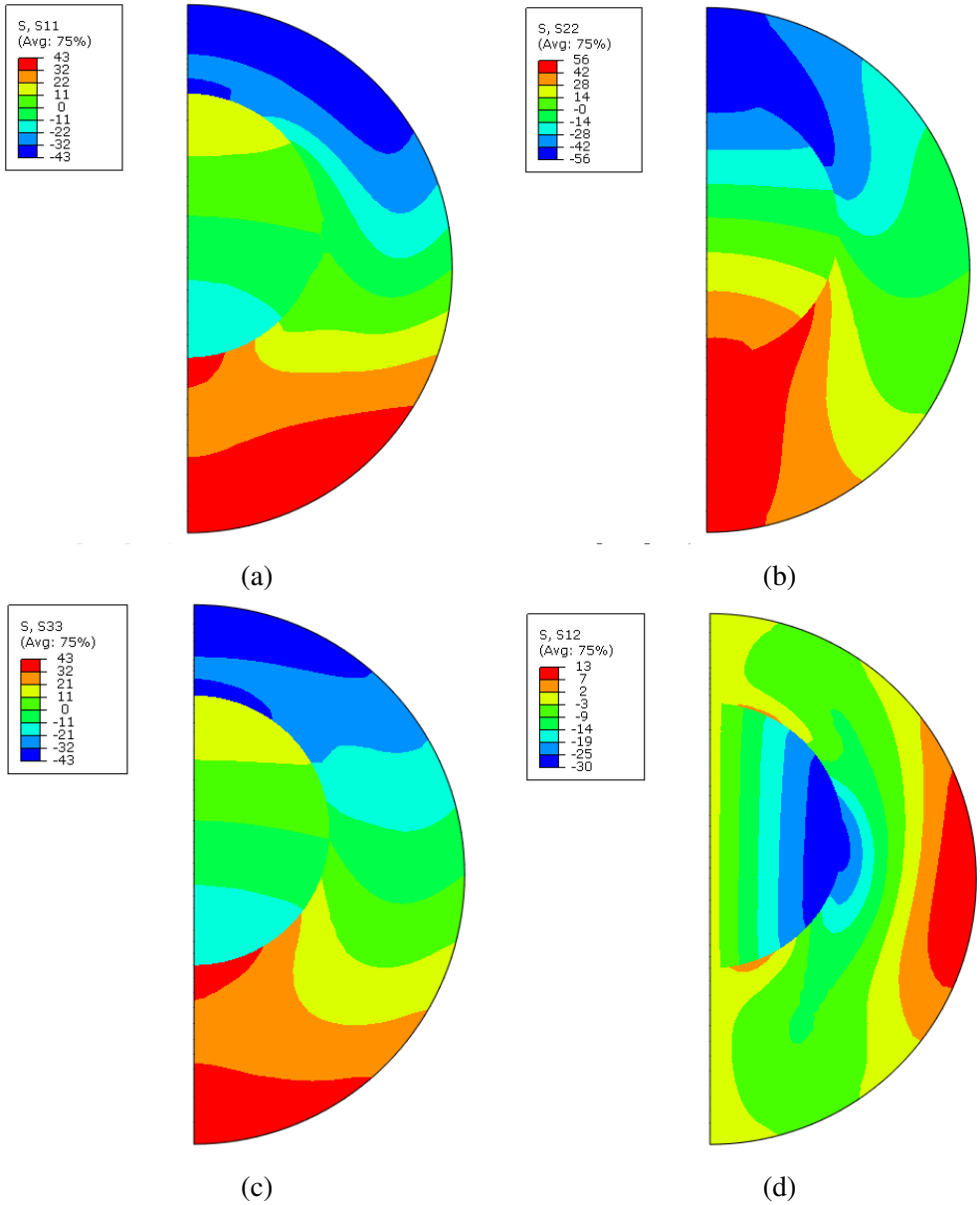

Figure 3.7: Modal stresses for a cancerous cell at the principal longitudinal mode f=500kHz.

Chapter 4

CYTOSKELETON CONSTITUTIVE LAW WITH DAMAGE AND RECOVERY OF FIBERS

In this chapter, we develop a theoretical framework to provide an understanding of the physical basis for the oncotripsy effect. We hypothesized that the cytodegeneration observed in the experiments of Mitteslstein *et al.* [54] results from cumulative damage to the cell over a large number (millions) of ultrasound cycles, mitigated by the recovery of the loss during the off periods between ultrasound pulses.

The first section is dedicated to reviewing existing cytoskeleton models. The modeling of the mechanical properties of living cells is currently an active area of research. Most models acknowledge the multiscale character of tissue mechanics and identify explicitly several scales, from continuum to subcellular components. Cell failure is usually taken as thresholds of strains or stresses. However, as this thesis is written, a cumulative damage model of cytoskeleton disruption has not been proposed yet.

Next, we develop a constitutive law for the cytoskeleton that describes the process of cytodegeneration due to a pulsed harmonic excitation which accounts for damage and recovery of cytoskeleton fibers, and it is based on the theory of network elasticity. The proposed model of oncotripsy follows as an application of cell dynamics, statistical mechanical theory of network elasticity, and 'birth-death' kinetics to describe processes of damage and repair of the cytoskeleton.

The numerical discretization to solve the system employing the finite element model is treated in Section 4.4. We propose a variational constitutive updated formulation of the cytoskeleton to characterize the damage and recovery of fibers.

The following section is dedicated to material point calculations. We discuss the damage and repair of the cytoskeleton fibers for a wide variety of material parameters and loading conditions. The study offers some vital insight into the understanding of the oncotripsy effect under the conditions of the experiments of Mitteslstein *et al.* [54].

We conclude with a complete mechanistic study on a finite element model that accounts for elasticity, viscosity, and kinetics of a healthy and cancerous cell, and we compare the results to the experimental trends observed by Mitteslstein *et al.* [54].

4.1 Previous mechanical modelling of the cytoskeleton on living cells

The mechanical models of living cells can be based on observations at the continuum level (i.e., viscoelastic or biphasic models) or in the micro-/nano- structural level (i.e., cytoskeleton models in adherent cells, or spectrin-network in the erythrocytes) [47]. In the first group, the length-scale of interest is much larger than the cytoskeleton fibers whereby the filament structure can be modeled, for instance, as a viscoelastic continuum. The continuum approach is straightforward if the mechanical properties at the cellular level are of interest. However, to study the microstructural response of the cell and its stiffness degradation, it is crucial to incorporate the intracellular filament network. This network is called *cytoskeleton*, and it is a system of filaments radiated from or to the nucleus and anchored to the plasma membrane. In eukaryotic cells, the cytoskeleton has three major components: microtubules, intermediate filaments, and microfilaments. Microfilaments are polymers of the protein actin, microtubules are composed of the protein tubulin, and intermediate filaments are composed of various proteins, depending on the type of cell. The cytoskeleton proportions resistance to cell shape distortion, is responsible for the movement of cells, helps to support the cytoplasm, and responds against external mechanical stimuli. In particular, microfilaments and intermediate filaments act like cables to support tension loads while microtubules act as beams in compression [46], in analogy to tensegrity structures [5, 31, 35, 44]. The contribution of physical factors in a hierarchical study is necessary to predict the distribution of stresses and strains from the cell to the tissue level, and relate it to the cytoskeleton mechanics. Therefore, a detailed understanding of the cytoskeleton is required to determine the response of cells under the effect of low-intensity pulsed ultrasound.

Several lines of evidence suggest that the cytoskeleton behaves like a discrete mechanical network [31], such as prestressed tensegrity structure which could explain how shape and movement of cells are controlled, and how it senses and respond to the environmental, mechanical loads. Kardas *et al.* [35], proposed a computational model of the osteocyte cytoskeleton based on this idea, which simulated the behavior of cells in-vivo under physiological mechanical loading. Their findings support the idea that external stimuli are mechanically transduced — i.e., the term *mechanotransdution* — to the nucleus through the cytoskeleton. In the same lines of research, Barreto *et al.* [5] suggested that the tensegrity approach is effective in modeling the overall behavior of cells but cannot predict the response of individual components of the cytoskeleton. Thus, they proposed a model combining a discrete model, which represented the cytoskeleton network, to a continuum model, which

acted as the cytoplasm and plasma membrane. This approach yielded a framework to study the distribution of stresses and strains in individual elements of the cytoskeleton and to correlate them to the mechanical properties of cells to resist external forces [5]. On efforts to model the cytoskeleton at the spectrin-level — proteins forming lattices responsible of the plasma membrane — Li *et al.* [44] formulated an algorithm that generates the cytoskeleton structures consistent with experimental observations. Their approach incorporates the effects of random network models in which spectrin links are used to populate different surfaces and shapes. The system is finally solved using coarse-grained molecular dynamics simulations [44].

By drawing on the concept of cytoskeleton dynamics, Deshpande *et al.* [16] built a continuum model that accounts for the biochemistry of an active cell that generates, supports, and responds to mechanical forces. In this bio-chemo-mechanical model, the dynamic rearrangement of the cytoskeleton is incorporated through the kinetics of biochemical state parameters and fiber orientation. The cytoskeleton is generalized to two- and three-dimensional networks by a homogenization analysis which assumes that the cell dimensions are much larger than the length-scale of the fibers.

As regards as models on cells under harmonic excitation, Meir and Kimmel [61] proposed a linear model of a cell, in which an organelle (the nucleus) oscillated within a viscoelastic medium (the cytoplasm) and computed the resonance frequencies. They suggested that a cumulative effect of the oscillatory strains transfers into biological alterations. Following on this mathematical approach, Fraldi *et al.* [20] studied the difference in resonance frequencies among cancerous and healthy cells. Similarly to Heyden and Ortiz [29], they proposed that these mechanical aberrations can be exploited to target and selectively kill cancer cells.

4.2 Constitutive Modeling

This section is concerned with the definition of the constitutive law of the cytoskeleton.

Cytoskeleton elasticity

At finite and constant temperature (T), the Helmholtz free energy (A) can be written as the change in the internal energy of a chain (U) and the change of entropy (S) as

$$A = U - TS. \tag{4.1}$$

Whereas the internal energy is the energy stored in chemical bonds and is dominant

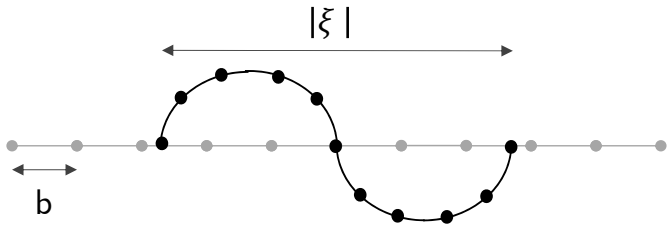

Figure 4.1: Sketch of the end-to-end vector ξ of a polymer chain. Each chain is composed by n links of size b.

in hard solids, the contribution of the entropy due to fluctuations is dominant in elastomers. The considerable disordered of the chains is measured by the number of configurations that these can adopt, and the entropy quantifies it.

According to the *shape network theory of elasticity* in statistical mechanics [19, 81], the cytoskeleton may be modeled as an amorphous network of cross-linked fibers. We consider that the fibers consist of many freely-jointed segments and are far from full extension (see Fig. 4.1). Subsequently, the end-to-end vector ξ will be given by the sum of each individual segment

$$\xi = \sum_{i=1}^{N} \xi_i. \tag{4.2}$$

Following the path of these segments in a volume, the probability of returning to the initial volume is a random process and results in a normal probability density function p(ξ) of the form,

$$p(\xi) = \left(\frac{3}{2\pi n b^2}\right)^{3/2} \exp\left(\frac{-3\xi^2}{2nb^2}\right), \tag{4.3}$$

where n is the number of fibers per unit volume, and b is the segment length. It is essential to notice that, because we are considering every direction in space equally distributed, the probability density is found within a spherical shell of radius ξ and thickness dξ [80] (see Fig. 4.2).

If we consider that the probability density is proportional to the number of configurations, then we can write the entropy Z as

$$Z = \gamma p(\xi), \tag{4.4}$$

with γ a volumetric constant. It follows that the entropy contribution of the energy per unit volume of a single chain can be computed as

$$F = -k_B T \log(Z). \tag{4.5}$$

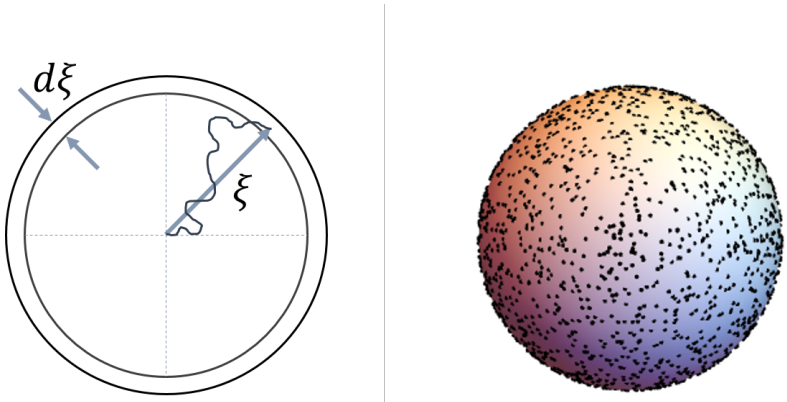

Figure 4.2: The probability density of fibers with respect to the end-to-end vector ξ is equally distributed in a spherical shell of thickness $d\xi$: (left) sketch of the end-to-end vector of a polymer chain (adapted from [80]) and (right) uniformly distributed numbers on a sphere surface.

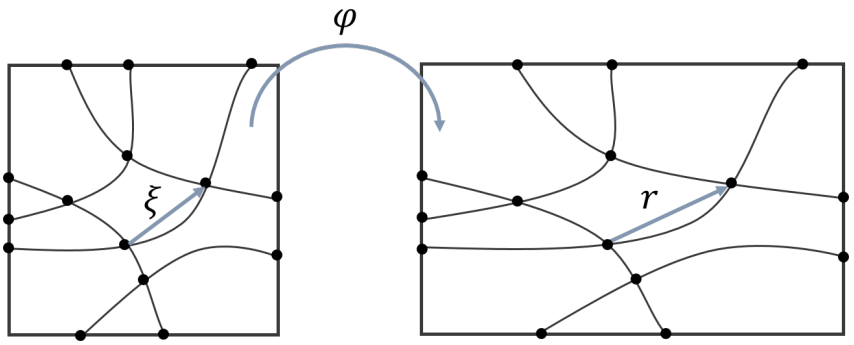

Figure 4.3: The cross-linking points of the polymer network move according to the local macroscopic deformation (adapted from [81]).

It is further assumed that the cross-linking points move according to the local macroscopic deformation (see Fig. 4.3). Under these assumptions, the change in entropy of the network can be written as

$$\Delta Z = \frac{-3k_B T}{2nb^2}(\xi^2 - r^2) = \frac{-3k_B T}{nb^2} K_{IJ} E_{IJ}, \tag{4.6}$$

where k_B is Bolzmann's constant, r is the end-to-end vector upon deformation, E_{IJ} is the material strain tensor and K_{IJ} is a property of the undeformed network. For both tensors, the uppercase letter subscripts refers to tensor components in the reference configuration.

A standard analysis (cf., e. g., [81]) for a general probability density p(ξ) then gives

the free-energy density per unit volume of the network as

$$A(F,T) = \frac{\mu(T)}{2} K_{IJ}(C_{IJ} + C_{IJ}^{-1}), \tag{4.7}$$

where $\mu(T)$ is a temperature-dependent shear modulus, F is the local deformation gradient and $C = F^T F$ is the right Cauchy-Green deformation tensor and T is the absolute temperature (cf., e. g., [52, 81] for background on continuum mechanics). An analysis of the configurational entropy of the fibers [19, 81] gives the shear modulus as

$$\mu(T) = \frac{2nl^2}{b^2} k_B T, \tag{4.8}$$

where l is the end-to-end distance of the fibers. In addition, the structure tensor K in (4.7) follows as

$$K_{IJ} = \int_{S^2} p(\xi)\xi_I \xi_J \, d\Omega, \tag{4.9}$$

where ξ is the unit vector pointing from one end of the fiber to the other, or *fiber direction*, $p(\xi)$ is the fraction of chains in the ensemble of direction ξ, S^2 is the unit sphere and $d\Omega$ is the element of solid angle. The density $p(\xi)$ is subject to the normalization condition

$$\int_{S^2} p(\xi) \, d\Omega = 1. \tag{4.10}$$

The distribution function $p(\xi)$ describes the structure of the cytoskeletal network and is assumed fixed and known. For instance, Smolyakov *et al.* [72] used single-cell force spectroscopy to test mechanical properties of four breast cancer 11 cell lines and found that the most invasive cells, MDA-MB231, contain actin fibers that are distributed randomly throughout the cell without any particular structure of preferred direction. By considering the underformed configuration, from a macroscopic perspective, homogeneous and isotropic on average, it follows that K_{IJ} must be isotropic. Then,

$$K_{IJ} = K_{IJ}\delta_{IJ} = \frac{1}{3} K_{II}. \tag{4.11}$$

For an *isotropic* fiber distribution of this type, $p = 1/4\pi$, and the structure tensor (4.9) reduces to the identity. Under these conditions, the free-energy density (4.7) specializes to

$$A(F,T) = \frac{\mu(T)}{2}(\mathrm{tr}(C) + \mathrm{tr}(C^{-1})), \tag{4.12}$$

where tr denotes the matrix trace.

An interesting aspect is that, as in tensegrity structures, the free energy density comprises of elements under tension (tr(C)) and compression (tr($C^{-}1$)). We can see that, if we consider a chain in a volume under the deformation mapping $x_1 = \frac{1}{\lambda_1}X_1$, $x_1 = \frac{1}{\lambda_1}X_1$ and $x_1 = \frac{1}{\lambda_1}X_1$, where X_I refers to the reference configuration, x_i to the deformed configuration with i=1..3, and λ_i a stretch larger than 1, the change in entropy is given by

$$\Delta Z = \frac{-3k_BT}{2nb_i^2}(\xi^2 - r^2) \tag{4.13}$$

$$= \frac{-3k_BT}{2nb_i^2}(X_1^2 + X_2^2 + X_3^2 - (x_1^2 + x_2^2 + x_3^2)) \tag{4.14}$$

$$= \frac{-3k_BT}{2nb_i^2}\Big(X_1^2 + X_2^2 + X_3^2 - \Big(\Big(\frac{1}{\lambda_1}X_1\Big)^2 + \Big(\frac{1}{\lambda_2}X_2\Big)^2 + \Big(\frac{1}{\lambda_3}X_3\Big)^2\Big)\Big) \tag{4.15}$$

$$= \frac{3k_BT}{2nb_i^2}\Big(\Big(\frac{1}{\lambda_1^2} - 1\Big)X_1^2 + \Big(\frac{1}{\lambda_2^2} - 1\Big)X_2^2 + \Big(\frac{1}{\lambda_3^2} - 1\Big)X_3^2\Big). \tag{4.16}$$

Now, suppose that this particular volume has n chains of type p=1...P .The change in entropy of all the chains type p results in

$$\Delta Z = \sum_{i=1}^{n} \frac{3k_B}{2nb_p^2}\Big(\Big(\frac{1}{\lambda_1^2} - 1\Big)X_1^2 + \Big(\frac{1}{\lambda_2^2} - 1\Big)X_2^2 + \Big(\frac{1}{\lambda_3^2} - 1\Big)X_3^2\Big). \tag{4.17}$$

For a particular volume, the number of chains n is very large. In addition, if we consider the material is homogeneous and isotropic, there is no directional preference on X_1, X_2 and X_3, so

$$\sum_{i=1}^{n} X_1^2 = \sum_{i=1}^{n} X_2^2 = \sum_{i=1}^{n} X_3^2 = \frac{1}{3}nl^2 \quad \text{and} \quad \frac{X_1^2 + X_2^2 + X_3^2}{n} = l^2, \tag{4.18}$$

with $\bar{\xi^2}$ the root mean square distance given by

$$\bar{\xi^2} = \frac{\int_0^\infty \xi p(\xi) d\xi}{\int_0^\infty p(\xi) d\xi} = \frac{3}{2b^2} = nl^2. \tag{4.19}$$

Using eq.(4.18) in eq.(4.17), the free energy for the elements under compression can be written as

$$A(F,T) = \frac{\mu(T)}{2}\Big(\frac{1}{\lambda_1^2} + \frac{1}{\lambda_2^2} + \frac{1}{\lambda_3^2} - 3\Big) \tag{4.20}$$

$$= \frac{\mu(T)}{2}\Big(\text{tr}(C^{-1}) - 3\Big), \tag{4.21}$$

with $\mu(T)$ given by eq.(4.8). Similarly, one can suppose that, at the same time, some elements are in tension. It follows that the deformation mapping can be assumed to be $x_1 = \lambda_1 X_1$, $x_1 = \lambda_1 X_1$ and $x_1 = \lambda_1$. The energy of this elements result can be easily show to be

$$A(F,T) = \frac{\mu(T)}{2}\Big(\lambda_1^2 + \lambda_2^2 + \lambda_3^2 - 3\Big) \tag{4.22}$$

$$= \frac{\mu(T)}{2}\Big(\mathrm{tr}(C) - 3\Big). \tag{4.23}$$

Finally, the total free energy will be the sum of the elements in compression and in tension, which results in eq. 4.12.

Cytoskeletal damage and healing

The experimental observations of Mittelstein *et al.* [54], Section 2 reveal that cell death requires the application of a large number (millions) of insonation pulses, which suggests that, under the conditions of the experiment, cell death is the result of a process of slow damage accumulation. Indeed, Mizrahi *et al.* [55] observed that the cytoskeletal actin fibers are catastrophically disrupted under the action of ultrasound stimulation of sufficiently high intensity, Fig. 1.4. In contrast, under low-intensity ultrasound, cellular responses exhibit gradual and sometimes complete recovery.

Whereas cytoskeletal elasticity has been extensively studied in the past, processes of damage accumulation in the cytoskeleton under LIPUS actuation, or high-cycle cell fatigue, appear to be as yet poorly understood. Building on past work on failure of polymer networks [4, 26, 27], we develop a model of cumulative cell damage that accounts for the gradual deterioration and recovery of cytoskeletal fibers. This competition between disruption ('death') and repair ('birth') is a classic example of a 'birth-death' process in evolutionary dynamics (cf. e.g., [60]). Birth-death processes are Markov processes characterized by two-state transitions: 'birth', which adds an element to the population, and 'death', which removes a component. Birth-death processes have many applications in demography, queueing theory, epidemiology, and other areas. In the present study, a 'death' occurs when a filament breaks, which results in a gradual loss of stiffness of the cytoskeleton. We hypothesize that when the stiffness degradation exceeds a critical threshold, the cell becomes unviable and dies.

We assume that the mechanism of damage accumulation to the cytoskeleton is the progressive disruption of the actin fibers. In order to account for the attendant loss

of stiffness, we introduce a damage variable $q(\xi)$ ranging from 0 to 1 such that $q(\xi) = 0$ when all the fibers with direction ξ are intact and $q(\xi) = 1$ when all the fibers with direction ξ are broken. We additionally assume that the breaking of the fibers requires a certain energy to be supplied. We represent these effects employing a free-energy density of the form

$$A(\mathbf{F}, T, \mathbf{q}) = \int_{S^2} p(\xi)\Big(\frac{\mu(T)}{2}(1-q(\xi))^2(\lambda^2(\xi)+\lambda^{-2}(\xi)-2)+\frac{\beta}{2}q^2(\xi)\Big)\, d\Omega, \quad (4.24)$$

where

$$\lambda(\xi) = \sqrt{C_{IJ}\xi_I\xi_J} \quad (4.25)$$

is the stretch ratio of the fibers of direction ξ and β is a constant. We note from (4.24) that the effect of a damage field $q(\xi)$ is to decrease the free-energy density of the fibers of direction ξ by a factor $(1 - q(\xi))^2$ at an energy cost of $(\beta/2)q^2(\xi)$. Additionally, damage relaxes the stresses in the network by reducing the stiffness of the fibers. Evidently, in the absence of damage, $q(\xi) = 0$, (4.24) reduces to (4.7), as required.

Following the method of Coleman and Noll [11], the thermodynamic driving forces for damage follow as

$$f(\xi) = -\frac{\partial A}{\partial q(\xi)} = p(\xi)\Big(\mu(T)(1 - q(\xi))(\lambda^2(\xi) + \lambda^{-2}(\xi) - 2) - \beta q(\xi)\Big). \quad (4.26)$$

We see from this expression that, by choice (4.24) of free-energy density, the driving force (4.26) comprises two terms. The first term represents the energy-release rate due to the disruption of the fibers and, therefore, promotes damage. The second term represents the energetic cost of disrupting the filaments, which hinders deterioration and promotes healing. Assuming linear kinetics, we obtain the damage evolution law

$$\alpha\, \dot{q}(\xi) = f(\xi), \quad (4.27)$$

where α is a kinetic coefficient. The kinetic relation (4.27), in combination with the driving forces (4.26), define an evolution of the cytoskeletal state as a balance between 'birth' and 'death' processes. Thus, the energy-release term $\mu(T)(1 - q(\xi))(\lambda^2(\xi)+\lambda^{-2}(\xi)-2)$ in the driving force induces progressive damage ('death') of the fiber population proportionally to the energy $\mu(T)(\lambda^2(\xi) + \lambda^{-2}(\xi))$ of the fibers. The additional factor $(1-q(\xi))$ brings the driving force to zero at full damage $q(\xi) = 1$ and ensures that $q(\xi) \leq 1$ at all times. By contrast, the energetic cost term $-\beta q(\xi)$ in the driving force tends to restore ('birth') the fiber population and thus

accounts for healing. Built into the form of (4.26) is the assumption that the rate of healing is proportional to the extent of damage. In particular, the healing rate vanishes for $q(\xi) = 0$, which it ensures that $q(\xi) \geq 0$ at all times.

Cell viscosity

Another source of resistance to cell deformation arises from the viscosity of the cytoplasm. This viscosity is likely to significantly damp resonant vibrations within the cell and limit their amplitude. On average, the cytoplasm viscosity does not differ considerably from that of water [22, 51]. However, the distribution of intracellular viscosity is highly heterogeneous. Full maps of subcellular viscosity have been successfully constructed via fluorescent ratiometric detection and fluorescence lifetime imaging [48]. However, this degree of detail is beyond the scope of this study. Instead, we assume an average viscosity uniformly distributed over the cytoplasm.

Further assuming linear viscosity, may be expressed explicitly as a function of $\dot{\boldsymbol{F}}$ and $\boldsymbol{F}$ in the form

$$\boldsymbol{\sigma}^v(\dot{\boldsymbol{F}}, \boldsymbol{F}) = \lambda \mathrm{tr}(\dot{\boldsymbol{F}}\boldsymbol{F}^{-1})\boldsymbol{I} + \eta(\dot{\boldsymbol{F}}\boldsymbol{F}^{-1} + \boldsymbol{F}^{-T}\dot{\boldsymbol{F}}^T) \tag{4.28}$$

with

$$\boldsymbol{d} = \mathrm{sym}(\dot{\boldsymbol{F}}\boldsymbol{F}^{-1}). \tag{4.29}$$

Here $\boldsymbol{\sigma}^v$ is the viscous part of the Cauchy stress tensor, and

$$\boldsymbol{d} = \mathrm{sym}(\dot{\boldsymbol{F}}\boldsymbol{F}^{-1}) \tag{4.30}$$

is the rate of deformation tensor, $\lambda = (\kappa - 2/3\eta)$, η is the shear viscosity, and κ is the bulk viscosity.

The corresponding viscous part of the first Piola-Kirchoff stress tensor is

$$\boldsymbol{P}^v(\dot{\boldsymbol{F}}, \boldsymbol{F}) = J\boldsymbol{\sigma}^v\boldsymbol{F}^{-T}, \tag{4.31}$$

where $J = \det(\boldsymbol{F})$. The total stress is then

$$\boldsymbol{P}(\dot{\boldsymbol{F}}, \boldsymbol{F}) = \partial_{\boldsymbol{F}} W(\boldsymbol{F}) + \boldsymbol{P}^v(\dot{\boldsymbol{F}}, \boldsymbol{F}). \tag{4.32}$$

A simple calculation reveals that the Newtonian viscosity law possesses the potential structure

$$\boldsymbol{P}^v = \partial_{\dot{\boldsymbol{F}}}\Phi(\dot{\boldsymbol{F}}, \boldsymbol{F}), \tag{4.33}$$

where that the viscous potential per unit undeformed volume is

$$\Phi(\dot{\boldsymbol{F}}, \boldsymbol{F}) = J \left\{ \frac{\lambda}{2} \mathrm{tr}(\boldsymbol{d})^2 + \eta \boldsymbol{d} \cdot \boldsymbol{d} \right\}. \tag{4.34}$$

For later reference we also introduce the viscous potential per unit deformed volume as

$$\phi(\boldsymbol{d}) = J^{-1} \Phi(\dot{\boldsymbol{F}}, \boldsymbol{F}) = \frac{\lambda}{2} \mathrm{tr}(\boldsymbol{d})^2 + \eta \boldsymbol{d} \cdot \boldsymbol{d}. \tag{4.35}$$

which has the property that

$$\boldsymbol{\sigma}^v = \partial \phi(\boldsymbol{d}), \tag{4.36}$$

i.e., that it acts as kinetic potential for the viscous component of the Cauchy stress.

4.3 Variational constitutive updates in finite deformations

In this section, we present a variational constitutive update framework for the cytoskeleton network undergoing damage and repair of fibers. The formulation used in this section is based on the framework proposed by Ortiz and Stainier [62].

Field equations

Let $\Omega \in \mathbb{R}^3$ be a continuous body and $\varphi : \Omega \to \mathbb{R}^3$ a deformation mapping. We consider the body deforms due to the action of body forces B and tractions t. In order to characterize the change of the material state due to deformation processes we introduce a constitutive relation which utilize internal variables. Let the strain energy density be given by

$$W = A(\mathbf{F}, \mathbf{q}) \tag{4.37}$$

with $\mathbf{F} = \nabla \varphi$ the deformation gradient, $\mathbf{q} \in \mathbb{R}^N$ is a collection of internal variables. For this calculations, we will not consider dependency on other variables as temperature, though it can be extended later.

In the presence of inertia effects, the deformation on the cell due to the low-intensity ultrasound excitation can be solved by the following governing equations pertaining to the dynamic deformations of a deformable body Ω:

$$\begin{aligned}
\mathbf{F} = \mathrm{Grad}\boldsymbol{\varphi} \quad & \text{in } \Omega \times (0, T) \\
\mathrm{Div}\mathbf{P} + \rho\mathbf{B} = \rho\mathbf{A} \quad & \text{in } \Omega \times (0, T) \\
\boldsymbol{\varphi}(t) = \hat{\boldsymbol{\varphi}}(t) \quad & \text{in } \Omega_1 \times (0, T) \\
\mathbf{P} \cdot \mathbf{N} = \hat{\mathbf{T}} \quad & \text{in } \Omega_2 \times (0, T) \\
\boldsymbol{\varphi}(0) = \boldsymbol{\varphi}(t) \quad & \text{in } \Omega
\end{aligned}$$

where $\mathbf{P}$ is the first Piola-Kirchhoff stress tensor, $\mathbf{B}$ is a body force density per unit of undeformed volume, $\hat{\varphi}$ is the prescribed value of the deformation mapping over the Dirichlet part of the boundary $\partial\Omega_1$, and $\hat{\mathbf{T}}$ is the prescribed traction applied to the Neummann part of the boundary $\partial\Omega_2$. In this analysis, the effect of gravity or other body forces are not considered, thus $\mathbf{B} = \mathbf{0}$. In addition, we are interested on wavelengths of the ultrasound that are long compared with the diameter of the cell. For instance, at 1MHz in water the wavelength results in ~100 times larger than a living cell of 15 microns. Because of this, the resulting pressure at the circunference of the cell will be equal to the intensity of the plane wave. Based on these and on the observations of Mittelstein *et al.* [54] presented in Chapter 2, we assume that the cell sloshes in suspension at the particle velocity of the media, reducing the boundary conditions to a displacement field applied on the surface of the cell.

Constitutive relations

The First Piola-Kirchoff stress tensor is given by

$$\mathbf{P} = \mathbf{P}^e + \mathbf{P}^v, \tag{4.38}$$

where we assume an additive decomposition of the equilibrium part $\mathbf{P}^e$ and a viscous part $\mathbf{P}^v$. The equilibrium part follows from Coleman & Noll thermodynamic equations as

$$\mathbf{P}^e = \frac{\partial W}{\partial \mathbf{F}} \tag{4.39}$$

and the viscous part follows as

$$\mathbf{P}^v = \frac{\partial \varphi}{\partial \dot{\mathbf{F}}}. \tag{4.40}$$

The evolution of the internal variables is determined by a suitable kinetic law of the form

$$\frac{\partial W}{\partial \mathbf{q}} + \frac{\partial \psi^*}{\partial \dot{\mathbf{q}}} \ni 0, \tag{4.41}$$

where ψ^* denotes the dissipation (dual) potential and we assume that such potential exists. In the case of rate-dependent problems, the differential inclusion is replaced by an equality. Alternatively, we can write eq.(4.41) in the minimization form

$$\dot{\mathbf{q}} = \arg\inf\{\dot{W} + \psi^*\}. \tag{4.42}$$

Introducing a discretization in time t^α with constant time steps $\Delta t = t^{\alpha+1} - t^\alpha$, and using a backward-Euler rule, the strain energy and internal variables result in

$$\dot{W} = \frac{W^{\alpha+1} - W^\alpha}{\Delta t} \qquad \text{and} \qquad \dot{\mathbf{q}} = \frac{\mathbf{q}^{\alpha+1} - \mathbf{q}^\alpha}{\Delta t}, \tag{4.43}$$

respectively, with $W^\alpha \equiv W(F^\alpha, q^\alpha)$. Then,

$$\frac{\mathbf{q}^{\alpha+1} - \mathbf{q}^\alpha}{\Delta t} = \arg\inf \left\{ \frac{W^{\alpha+1} - W^\alpha}{\Delta t} + \psi^* \left(\frac{\mathbf{q}^{\alpha+1} - \mathbf{q}^\alpha}{\Delta t} \right) \right\}. \tag{4.44}$$

Reorganizing, leads to an incremental variational constitutive update of the form

$$q^{\alpha+1} = \arg\inf \left\{ W^{\alpha+1} + \Delta t \psi^* \left(\frac{q^{\alpha+1} - q^\alpha}{\Delta t} \right) \right\}. \tag{4.45}$$

Finally, we define the right-hand side as an effective incremental potential

$$\mathcal{F}^{\alpha+1}(F^{\alpha+1}, q^{\alpha+1}) = \arg\inf \left\{ W^{\alpha+1} + \Delta t \psi^* \left(\frac{q^{\alpha+1} - q^\alpha}{\Delta t} \right) \right\} \tag{4.46}$$

and the stresses can be computed as

$$P^{\alpha+1} = \frac{\partial W^{\alpha+1}}{\partial F^{\alpha+1}} = \frac{\partial \mathcal{F}^{\alpha+1}}{\partial F^{\alpha+1}}. \tag{4.47}$$

Integration scheme

The system is solved via the Newmark's scheme,

$$\varphi_{n+1} = \varphi_n + \Delta t \dot{\varphi}_n + \left(\frac{1}{2} - \beta \right) \Delta t^2 \ddot{\varphi}_n + \beta \Delta t^2 \ddot{\varphi}_{n+1} \tag{4.48}$$

$$\dot{\varphi}_{n+1} = \dot{\varphi}_n + (1 - \gamma) \Delta t \ddot{\varphi}_n + \gamma \Delta t \ddot{\varphi}_{n+1}, \tag{4.49}$$

where φ_n, $\dot{\varphi}_n$, and $\ddot{\varphi}_n$ are the approximations of $\varphi(t_n)$, $\dot{\varphi}(t_n)$ and $\ddot{\varphi}(t_n)$, respectively. The parameters β and γ determine the accuracy and stability of the algorithm (cf. [30]). We choose an explicit solver, i.e., $\beta = 0$ and $\gamma = 0.5$.

4.4 Numerical implementation

In this section, we present the numerical integration scheme for the initial boundary value problem implemented as a finite element model. For a detailed description of the finite element method, please refer to [30].

The surface integral in eq. (4.24) is computed by cubature rules as derived by Cools in [12]. In particular, we choose n=14 cubature points with weights $\{w_1, ..., w_n\}$ and locations $\{\xi_1, ..., \xi_n\}$. These are provided in Table 4.1. In our computations, each fiber direction corresponds to a cubature point as shown in Figure 4.4.

The first Piola-Kirchoff stress tensor of the cytoskeleton follow as

$$\frac{\partial W_\alpha}{\partial \mathbf{F}}(\mathbf{F}_{\alpha+1}, T) = \sum_{\lambda_{p,\alpha+1}} w_p \mu(T) (1 - q_{p,\alpha+1})^2 (1 - \lambda_{p,\alpha+1}^{-4}) (\mathbf{F}_{\alpha+1} \xi_p) \otimes \xi_p \tag{4.50}$$

Table 4.1: Weights w and locations ξ for n=14 cubature points with $w_1 = 1/15$, $w_2 = 7.5\text{e}{-2}$, $r_1 = 0$ and $r_2 = \sqrt{3}/3$.

n	w	ξ
1	w_1	$\{1, r_1, r_1\}$
2	w_1	$\{-1, r_1, r_1\}$
3	w_1	$\{r_1, 1, r_1\}$
4	w_1	$\{r_1, -1, r_1\}$
5	w_1	$\{r_1, r_1, 1\}$
6	w_1	$\{r_1, r_1, -1\}$
7	w_2	$\{r_2, r_2, r_2\}$
8	w_2	$\{r_2, r_2, -r_2\}$
9	w_2	$\{r_2, -r_2, r_2\}$
10	w_2	$\{r_2, -r_2, -r_2\}$
11	w_2	$\{-r_2, r_2, r_2\}$
12	w_2	$\{-r_2, r_2, -r_2\}$
13	w_2	$\{-r_2, -r_2, r_2\}$
14	w_2	$\{-r_2, -r_2, -r_2\}$

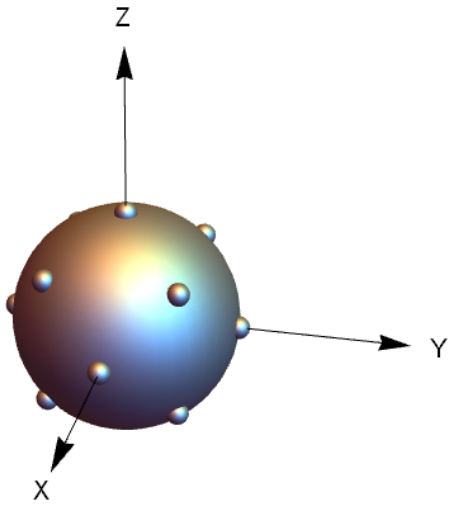

Figure 4.4: Location of the quadrature points on the surface of a unit sphere.

with $\otimes$ the dyadic or outer product.

The second Piola-Kirchoff stress tensor is

$$\mathbf{S}_{\alpha+1} = \mathbf{F}_{\alpha+1}^{-1}\mathbf{P}_{\alpha+1} = \sum_{\lambda_{p,\alpha+1}} w_p \mu(T)(1 - q_{p,\alpha+1})^2(1 - \lambda_{p,\alpha+1}^{-4})\xi_p \otimes \xi_p. \tag{4.51}$$

In the undeformed configuration we have $\mathbf{F} = \mathbf{I}$, leading to a stress free material in the reference configuration.

For completeness, the Cauchy stress tensor results in

$$\sigma_{\alpha+1} = J^{-1}\mathbf{F}_{\alpha+1}^{-1}\mathbf{P}_{\alpha+1}. \tag{4.52}$$

The derivation of the tangent matrix is cumbersome and not needed as we are solving the system explicitly, so the derivation can be found in appendix A.1.

At each material point, the damage state is characterized by n number of fiber directions which results in a vector of the form,

$$q = \{q(\xi_1), ..., q(\xi_p), ..., q(\xi_n)\}. \tag{4.53}$$

The state of damage update follow as

$$q_{p,\alpha+1} = \frac{\alpha\, q_{p,\alpha} + \mu(\lambda_{p,\alpha+1}^2 + \lambda_{p,\alpha+1}^{-2} - 2)\Delta t}{\alpha + \beta\Delta t + \mu(\lambda_{p,\alpha+1}^2 + \lambda_{p,\alpha+1}^{-2} - 2)\Delta t}, \tag{4.54}$$

which can also be written as

$$1 - q_{p,n+1} = \frac{\alpha + \beta\Delta t - \alpha\, q_{p,\alpha}}{\alpha + \beta\Delta t + \mu(\lambda_{p,\alpha+1}^2 + \lambda_{p,\alpha+1}^{-2})\Delta t}. \tag{4.55}$$

The evolution of the damage at an element with N number of quadrature points is given by a weighted average as

$$q_e(\xi_p, t) = \frac{1}{V_e}\int_{V_e} q(\xi_p, t)dx = \frac{1}{V_e}\sum_N \mu_N q(\xi_p, t) \tag{4.56}$$

with V_e the volume of the element in the undeformed configuration and μ_N the quadrature weight. The average guarantees $q_e \in [0, 1]$ at each element.

The state of damage on a mesh in the fiber direction ξ_p is computed as follows:

$$\bar{q}(\xi_p, t) = \frac{1}{V}\int_\Omega q(\xi_p, t)dx = \frac{1}{V}\sum_K V_e q_e(\xi_p, t) \tag{4.57}$$

with V the volume of the cytoskeleton, K the cytoskeleton elements, and q_e the damage at the element. Again, this guarantees that $\bar{q} \in [0, 1]$ at each fiber direction.

The evolution of the maximum damage is

$$\bar{q}_{max}(\xi, t) = \max\{\bar{q}(\xi, t)\}. \tag{4.58}$$

The total weighted average results in

$$\langle q(t)\rangle = \frac{1}{|S^2|}\int_{S^2} \bar{q}(\xi, t)dx = \frac{1}{|S^2|}\sum_{N} \mu_N \bar{q}(\xi, t). \tag{4.59}$$

Notice that we consider the total weighted average on the underformed surface area. However, one could also consider a different form of the average, in which the highest weight belongs to the most damaged fiber.

Finally, for these computations, the failure criterion is a threshold which the mean average damage cannot surpass:

$$\langle q(t)\rangle = q_c. \tag{4.60}$$

The critical value is a material parameter, and its upper bound $q_c = 1$ corresponds to the complete braking of all microstructural elements. Nevertheless, the cell may die before reaching this upper bound; thus, the critical damage will have to be adjusted to experimental results with $q_c \in [0, 1]$.

The failure criterion quantifies the maximum average change of the shear modulus under which the cytoskeleton can sustain loads under harmonic excitation. This is,

$$q_c = 1 - \sqrt{\frac{\mu_c}{\mu_0}}, \tag{4.61}$$

where μ_c is the minimum shear modulus and μ_0 is its value at the reference configuration (i.e., μ(t=0)=μ_0). Fig. 4.5 shows the fraction of change between the critical shear modulus μ_c to the initial or reference shear modulus μ_0.

As regards the viscosity, we adopt a constitutive update by means of the method of incremental deformations. By these, the gradient of deformation is given by

$$F^{\alpha+1} = \bar{F}F^{\alpha} \tag{4.62}$$

with $\bar{F}$ the incremental deformation gradient.

It follows that the change of the energy density per unit time is

$$\frac{1}{\Delta t}W(\bar{F}) = \frac{1}{\Delta t}W_0(F^{\alpha+1}F^{\alpha-1}) \tag{4.63}$$

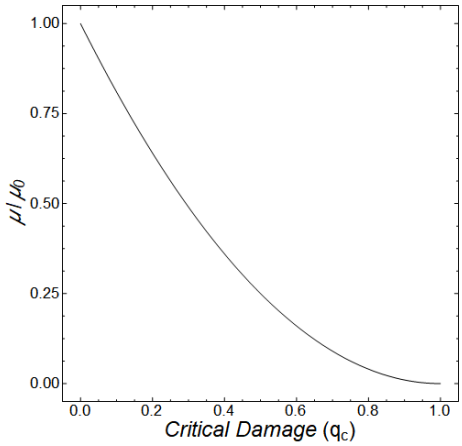

Figure 4.5: The failure criterion limits the change in shear modulus with respect to its reference configuration.

and the Piola Kircchhoff stresses,

$$P_{iJ}(\bar{F}) = \frac{1}{\Delta t}\frac{\partial W_0}{\partial F_{jB}^{\alpha+1}}\frac{\partial F_{jB}^{\alpha+1}}{\partial \bar{F}_{iJ}} \tag{4.64}$$

$$= \frac{1}{\Delta t}\frac{\partial W_0}{\partial F_{jB}^{\alpha+1}}\frac{\partial (\bar{F}_{jM}F_{MB}^{\alpha-1})}{\partial \bar{F}_{iJ}} \tag{4.65}$$

$$= \frac{1}{\Delta t}\frac{\partial W_0}{\partial F_{jB}^{\alpha+1}}F_{JB}^{\alpha-1}. \tag{4.66}$$

Thus,

$$P_{iJ}(\bar{F}) = \frac{1}{\Delta t}[P_0(F^{\alpha+1}F^{\alpha-1})]_{iB}F_{JB}^{\alpha-1}. \tag{4.67}$$

Likewise, the stiffness matrix update is given by

$$T_{iJkL} = \frac{\partial P_{iJ}}{\partial F_{kL}} = \frac{\partial (P_0)_{iB}}{\partial F_{lD}^{\alpha+1}}\frac{\partial F_{lD}^{\alpha+1}}{\partial \bar{F}_{kL}}F_{JB}^{\alpha-1} \tag{4.68}$$

$$= (T_0)_{iBlD}\frac{\partial (\bar{F}_{lN}F_{ND}^{\alpha-1})}{\partial \bar{F}_{kL}}F_{JB}^{\alpha-1} = (T_0)_{iBlD}F_{JB}^{\alpha-1}F_{LD}^{\alpha-1}. \tag{4.69}$$

Thus,

$$T_{iJkL} = [T_0(F^{\alpha+1}F^{\alpha-1})]_{iBlD}F_{JB}^{\alpha-1}F_{LD}^{\alpha-1}. \tag{4.70}$$

4.5 Model verification and parameter analysis

This section presents a numerical study at the material point level to understand the softening behavior of the cytoskeleton and the influence of the material parameters on the damage evolution. In these examples, we assume the load is applied quasi-statically, the cytoskeleton is isotropic and non-viscous, and it fails at critical damage q_c=1.

Stretch

Triangular Pulse In this example, the material point is subject to a uniaxial stretch history in the form of a triangular pulse with an increasing amplitude of λ. The uniaxial condition establishes that $P_{22} = P_{33} = 0$.

The energy density, as presented in the previous section, is used with an effective shear modulus of $\mu = 0.15$MPa, and damage parameters $\alpha = 0.001$ MPa ms and $\beta = 0.001$ MPa. For a triangular uniaxial stretch (Fig. 4.6a), we present the stress-stretch, stress *vs.* time, and mean damage *vs.* time in Fig. 4.6b, c and d, respectively. As can be observed in the stress-stretch curve, the cytoskeleton response differs from a material without damage. As stress increases, the material deviates from linearity. This is not only associated with the deviation from small deformations, but also to the rearrangement of the cytoskeleton. In addition, the stress-strain curve shows the energy dissipated by the rupture of the fibers. As seen in Fig 4.7, the effect of the stretch on the fibers is quite complex. During one cycle of the triangular pulse, the damage state undergoes moments of damage and recovery. As the stretch increases (or diminishes) away from equilibrium, the 'death' of fibers is preponderant. However, as the stretch is unloaded to its initial configuration, a damage-recovery trade-off results in the 'birth' of fibers. These complex behavior during the loading-unloading phases result in a wavy damage curve.

Apart from studying the mean damaged state, it is of interest to study the damage along each fiber (see Fig. 4.8). As expected, the fibers along the direction of the uniaxial stretch (ξ_1 and ξ_2) are the ones carrying most of the load and, for enough cycles and stretch amplitude, will eventually fail. However, it is also interesting to notice that, because of the competition between damage and recovery, the damage state can result in a well-defined steady-state amplitude, as seen in Fig 4.6d. In this way, for low enough strain amplitude, the balance between damage accumulation and healing prevents the cytoskeleton from attaining failure even under a very large number of cycles.

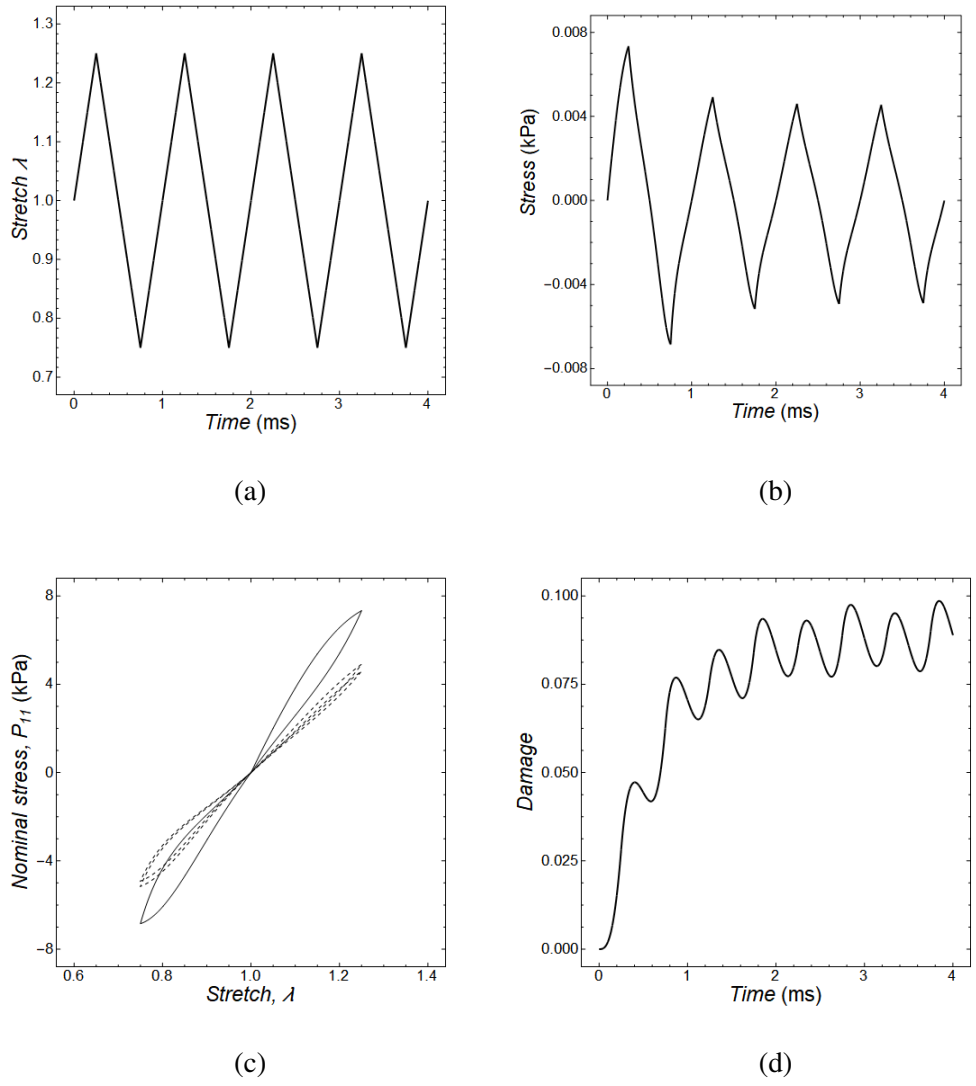

Figure 4.6: Damage evolution at a material point for a triangular stretching history. (a) Applied triangular stretching history; (b) nominal stress (P_{11}) evolution; (c) nominal stress (P_{11}) *vs.* stretch (λ) curve, (d) mean damage evolution.

Square Pulse In this second example, we subject a unidimensional cube to a uniaxial stretch history in the form of a square pulse and analyze the mean damage curve under several parameters μ, α, and β. The results of the numerical experiments are shown in Fig. 4.9 and Fig. 4.10.

Fig. 4.9 presents an example of how the model behaves under two different shear modulus. From these plots, it is clear that the stiffest cytoskeleton will attain higher levels of damage. Recall, however, that failure is determined by the ability of the structure or material to support loads. Therefore, the material to fail will be the one

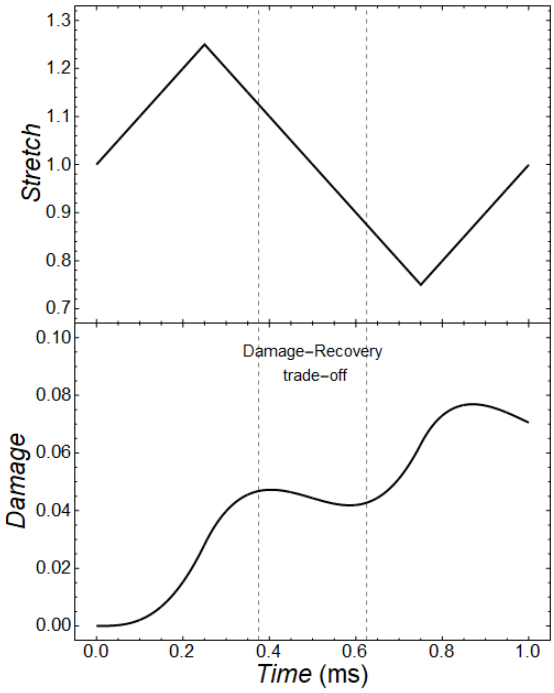

Figure 4.7: Damage evolution depends on the shape of the applied load. As the stretch increases (or diminishes) away from equilibrium, there is a damage-recovery trade-off which will result in 'death' or 'birth' of fibers.

to reach their critical damage first.

Fig. 4.10 shows the evolution of the damage for different combinations of kinetic parameters. While fibers break during the loading and hold phase, they are also able to recover. The parameters α and β are responsible for the interplay between these two phases. At a constant ratio of α to β, increasing both parameters by the same factor reduces the mean damage. At constant α, lower β increases the recuperation time and the damage, which leads to a longer time for the system to reach its initial shear modulus. In contrast, smaller α values lead to a higher amount of broken fibers but faster recovery.

Finally, the force *vs.* time plots (Fig. 4.11a.) shows that the force carried by the fibers reduces with increasing damage, reflecting the reduction of stiffness by the disruption of fibers (Fig. 4.11b).

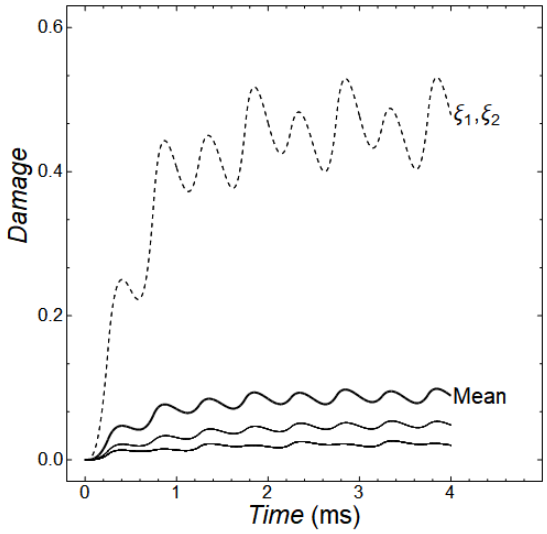

Figure 4.8: Damage evolution of the fibers with respect to their direction. In particular, ξ_1 and ξ_2 are parallel to the load.

Shear

The same numerical experiments are performed for simple shear at the material point, and the results are shown in Fig 4.12. For the same material parameters, the cytoskeleton does not experience as a high damage state as for the uniaxial case. However, the softening could be non-negligible, and under many cycles, its effect could play an important role in the overall failure of the material.

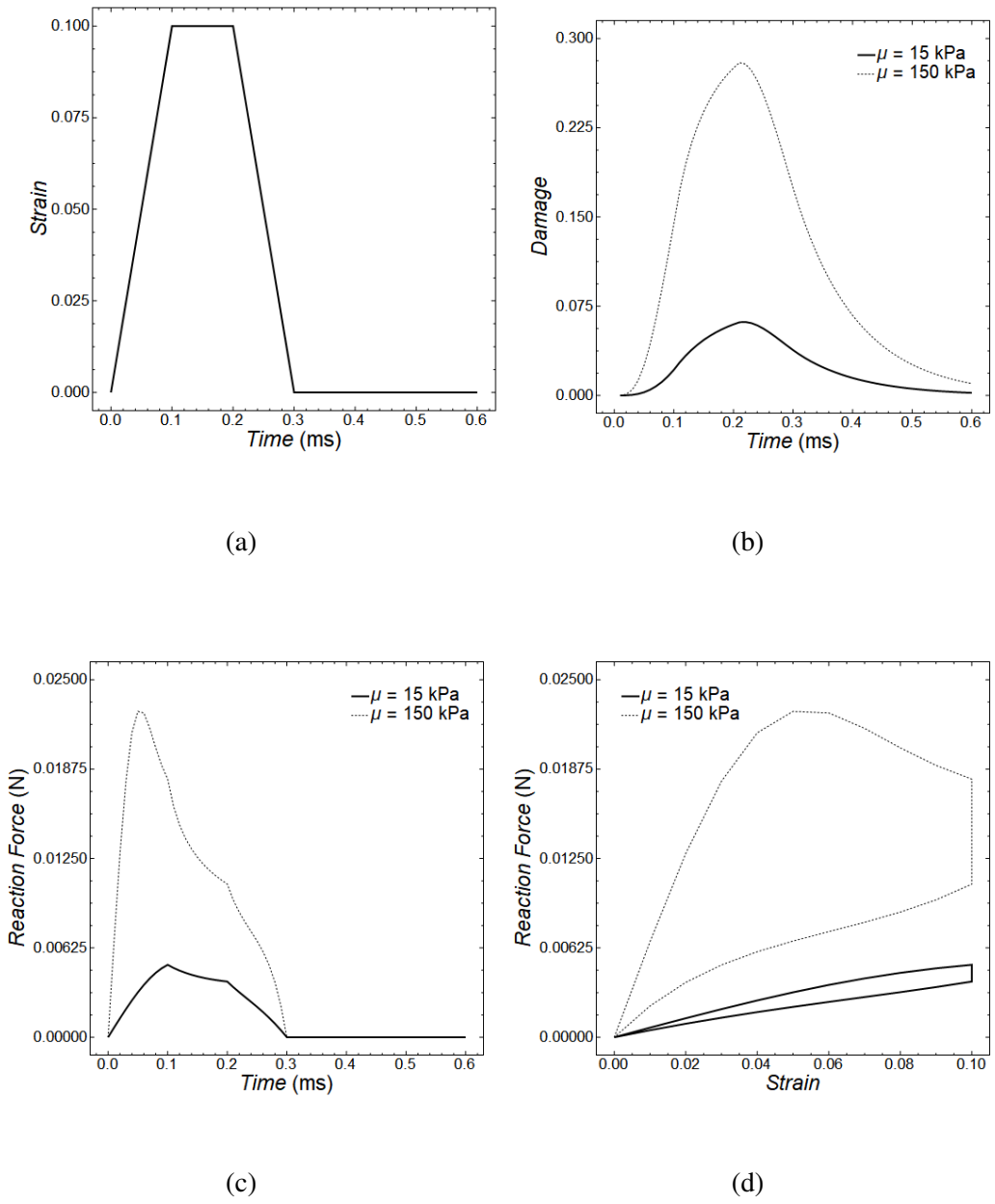

Figure 4.9: Damage state for an uniaxial stretch of a 1x1x1mm^3 cube fixed on the bottom for two different shear modulus. (a) Strain history applied on the top; (b) damage evolution; (c) reaction force *vs.* time; and, (d) reaction force *vs.* nominal strain.

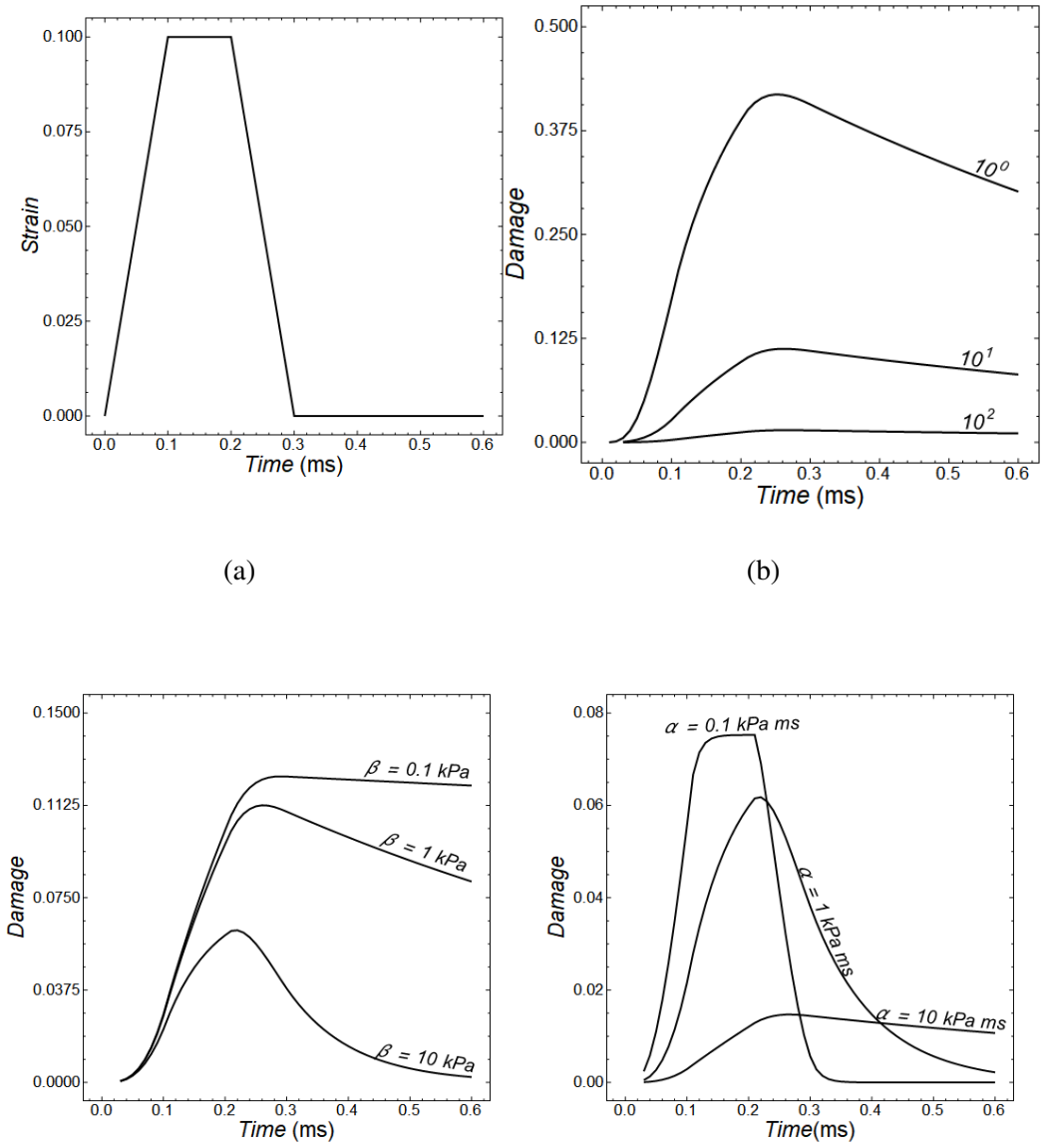

Figure 4.10: Damage state for an uniaxial stretch of a 1x1x1mm^3 cube fixed on the bottom. (a) Strain history applied on the top; (b) damage evolution for a constant ratio α to β, and $\alpha = \beta = 0.1\{10^0, 10^1, 10^2\}$ (Units: kPa ms and kPa for α and β respectively); (c) damage evolution for α = 1kPa ms; and, (d) damage evolution for β = 10kPa.

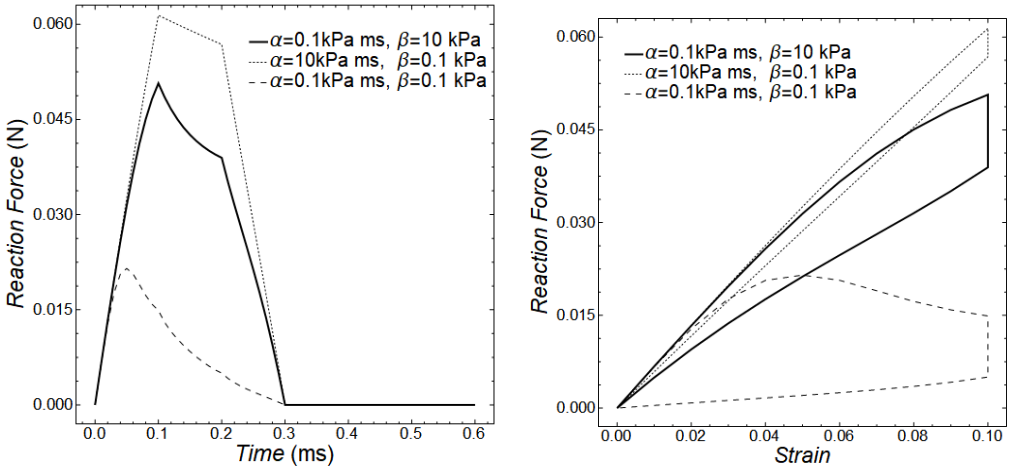

(a) (b)

Figure 4.11: Uniaxial stretch of a 1x1x1mm^3 cube fixed on the bottom. (a) Evolution of the reaction force and, (b) force *vs.* strain curve for different kinetic parameters

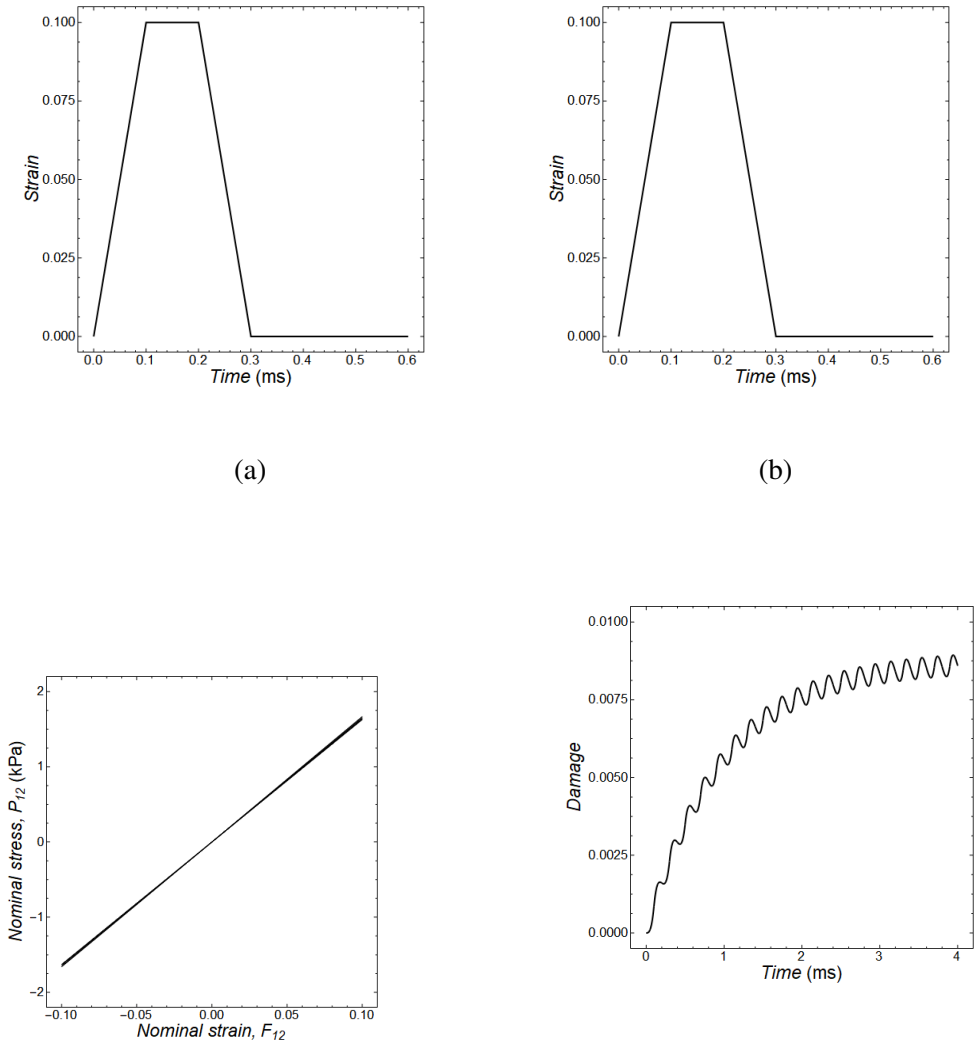

Figure 4.12: Damage state for a simple shear of a material point. (a) Applied triangular stretching history; (b) nominal stress (P_{12}) evolution; (c) nominal stress (P_{12}) *vs.* nominal strain (F_{12}) curve, (d) mean damage evolution.

4.6 Validation of the oncotripsy effect

In this section, we validate the constitutive law by simulating the cancerous and healthy cells under harmonic excitation and comparing the predicted damage-time histories against the trends observed experimentally. In the first part of this section, we describe the geometry and properties used in the simulation. The damage evolution is then validated against the experiments, showing a very good prediction.

The analysis was set-up in EurekaLite, a finite element code developed in the Computational Mechanics Group at Caltech.

Description of the model

We build a finite element model of a spherical eukaryotic cell subject to a harmonic oscillation. In mammalian cells, the nucleus, as the largest cellular organelle, occupies between 10 % and 20 % of the total cell volume [2, 49]. It is surrounded by the cytosol, a viscoelastic solid containing several subcellular structures such as the Golgi apparatus, the mitochondrion, and the endoplasmic reticulum. The cytosol and other organelles contained within the plasma membrane, for instance, mitochondria and plastids, form the so-called cytoplasm. The nucleus is bounded by the nuclear envelope and contains the nucleoplasm, a viscoelastic solid similar in composition to the cytosol. It furthermore comprises the nucleolus, which constitutes the largest structure within the nucleus and consists of proteins and RNA. In the present work, we neglect the organelles within the cytosol, which is idealized as a uniform viscous matrix containing the cytoskeleton. The nucleus is likewise idealized as rigid and omits explicit consideration of the nucleoplasm. In particular, the nucleus strain energy follows a Neo-Hookean, which is also embedded in a Newtonian fluid. Given the focus on cytoskeletal dynamics, we additionally neglect the effect of nuclear and cellular membranes.

For these computations, the cell under consideration has a diameter of 18μm and a concentric nucleus of 9μm. The cell is loaded by imposing a sinusoidal displacement at the membrane applied as a train of pulses, with ON and OFF periods. Owing to the symmetric nature of the problem around the prescribed displacement, we built an axisymmetric model of the cell. To guarantee convergence, we consider two different meshes: a fine mesh consisting of ~2500 linear axisymmetric triangular elements and a coarser mesh of ~900 triangular elements. The geometry and two meshes used for the calculations are shown in Fig. 4.13. The system is solved explicitly with a constant timestep proportional to the Courant-Friederichs-Lewy

Table 4.2: Geometry, mass and effective mechanical properties of a lymphoma cell type K562. The mechanical properties are tuned so that resonance occurs at 500kHz and q_{max} is reached at t=20ms.

Characersitic		**Value**	**Unit**
a	nucleus radius	0.0045	mm
b	cell radius	0.009	mm
α	kinetic damage parameter 1	0.0001	MPa ms
β	kinetic damage parameter 2	0.0005	MPa
μ_c	shear modulus of the cytoskeleton (cancerous)	0.033	MPa
μ_n	shear modulus of the nucleus(cancerous)	0.3	MPa
μ_c	shear modulus of the cytoskeleton (healthy)	0.066	MPa
μ_n	shear modulus of the nucleus(healthy)	0.6	MPa
η	shear viscosity of the cell	1e-5	MPa ms
ρ_c	density of the cytoskeleton	0.001	gr/mm^3
ρ_n	density of the nucleus	0.0015	gr/mm^3
ν	Poisson ratio	0.25	

condition.

The effective material parameters — i.e., shear modulus of the cytoskeleton and nucleus, kinetic damage parameters α and β and viscosities — were recovered from the experimental paper by Mittelstain *et al.* [54] and certain hypotheses. We refer to the frequency tests in Fig. 2.6 showing a peak in cell death at 500kHz. We hypothesize that this behavior is due to a longitudinal mode of the nucleus located in the neighborhood of this frequency. By means of frequency response analysis, we obtain the modal shear modulus of the cytoskeleton such that a longitudinal mode occurs at 450kHz and, for purposes of validation, we choose the kinetics parameters that generate considerable damage in an exposure time of 2ms. For the healthy cell, we choose the shear modulus to be 1.70 times stiffer, which results in a mode at 680kHz, and keep the kinetic parameters constant. The density is 1.5 g/cm^3 for the nucleus and 1 g/cm^3 for the cytoplasm [29]. The effective viscosity of the cytoplasm has been reported to be between 2 to 6 times the one of water ($\sim 10^{-3}$Pa s at 20^0C) [50]. For the bulk modulus, we resort to small-strain elastic moduli conversion. The material properties, geometry, and mass of the cell are collected in Table 4.2.

Due to the wavelength of the ultrasound being much longer than the cell length, we hypothesize the cell responds with the particle velocity of the applied field. Then, the performed simulations concerned an applied displacement field at the external

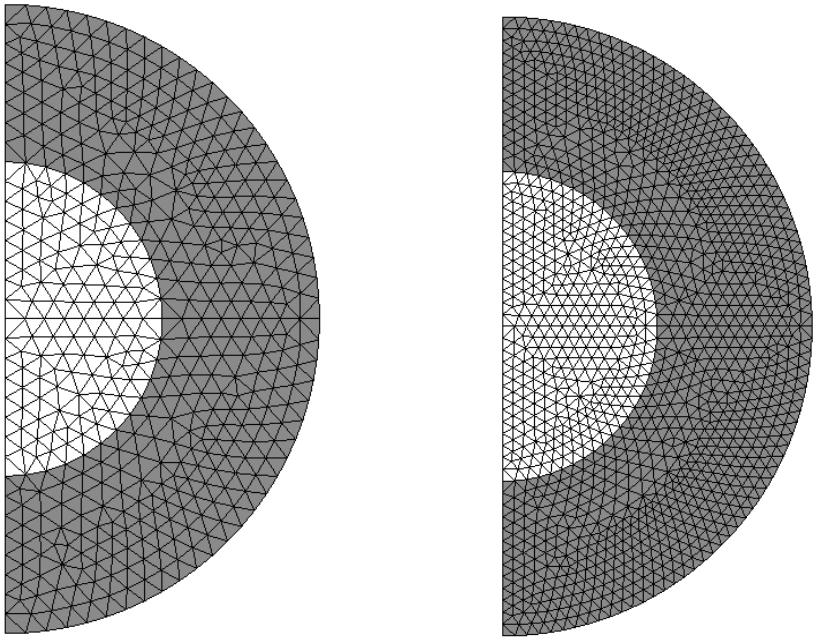

(a) (b)

Figure 4.13: Axysimmetric element meshes used in the simulations: (a) Coarse 902-element mesh and (b) fine 2464-element mesh. Color legend: (white) nucleus and (gray) cytoplasm.

surface of the cell. In particular, the prescribed displacement field $\bar{u}$

$$\bar{u} = \frac{P_0}{\omega \rho_f c_f} \sin(\omega t), \tag{4.71}$$

where P_0 is the pressure, ω is the excitation frequency,and ρ_f and c_f are the density and wave speed velocity of water.

Results and Analysis

The experimental loading conditions of Mittelstain *et al.* [54] were considered as load cases. In particular, we study the evolution of damage, stresses and nucleus displacement on a healthy and cancerous cell in the frequency range 300-800kHz, focal pressure of 1.4MPa and duty cycle 10%. We solve the system for an ultrasound exposure of 2ms.

Nucleus displacement The displacement on the nucleus is computed as

$$\bar{u}(t) = \frac{1}{|\Omega|} \int_{\Omega} u(t) dx = \frac{1}{|\Omega|} \sum_{K} v_e u_e(t) \tag{4.72}$$

with

$$u_e(t) = \sum_{K_e} N^a u^a(t) \tag{4.73}$$

where u is the displacement, N^a is the shape function at node a, K is the set of the nucleus elements v_e is the volume of the element in the deformed configuration, and Ω is the total volume of the nucleus in the deformed configuration

Fig. 4.14 and Fig. 4.15 shows the nucleus displacement evolution for a cancerous and healthy cell, respectively. The displacements show clearly the ON/OFF periods of the ultrasound. Because the accumulated damage in 2 ms is very low, there is minimal change in the maximum displacement over time. However, at resonance, the nucleus displacement changes dramatically, leading to higher amplitudes and, eventually, to the highest possible accumulated damage. If we consider the stretch of the cytoplasm to be of the form,

$$\lambda = 1 - \frac{u}{b - a} \tag{4.74}$$

with b and a the cell and nucleus radius, respectively, the axial stretch at resonance is in the range λ=0.88-1.22. However, far away from the resonant frequency, the stretch can be as low as 0.98-1.02, i.e., the cell behaves in the small strain regime.

In addition, there exists a phase lag of the displacement with respect to the driving force as result of the viscosity.

Damage evolution The simulated displacements, stresses and damage evolution for one cycle is shown in Fig. 4.16, Fig. 4.17, Fig. 4.18, Fig. 4.19, and Fig. 4.20. We exhibit the meridional section of each state of the cancerous cell through level contours. The damage at the element $\bar{q}_e$ is computed as the weighted average of the damage in each direction ξ at the material point.

Shortly after initiation, the damage on the cytoskeleton propagates from the outside of the cell to its interior, driven by the local stretch of the fiber at direction ξ. Eventually, the cell structure reaches regions of large damage along the path of the nucleus displacement. These regions correspond to the location of the highest axial tensile and compressive stresses, as shown in Fig. 4.18. After the release of the load, the healing process occurs at constant recuperation time until the following pulse initiates. Even though the cell damage relaxes during each off-cycle, it accumulates due to the recovery time being longer. This slow damage accumulation over many (thousands or millions) of cycles is known as *fatigue*, and it will be treated in the following chapter.

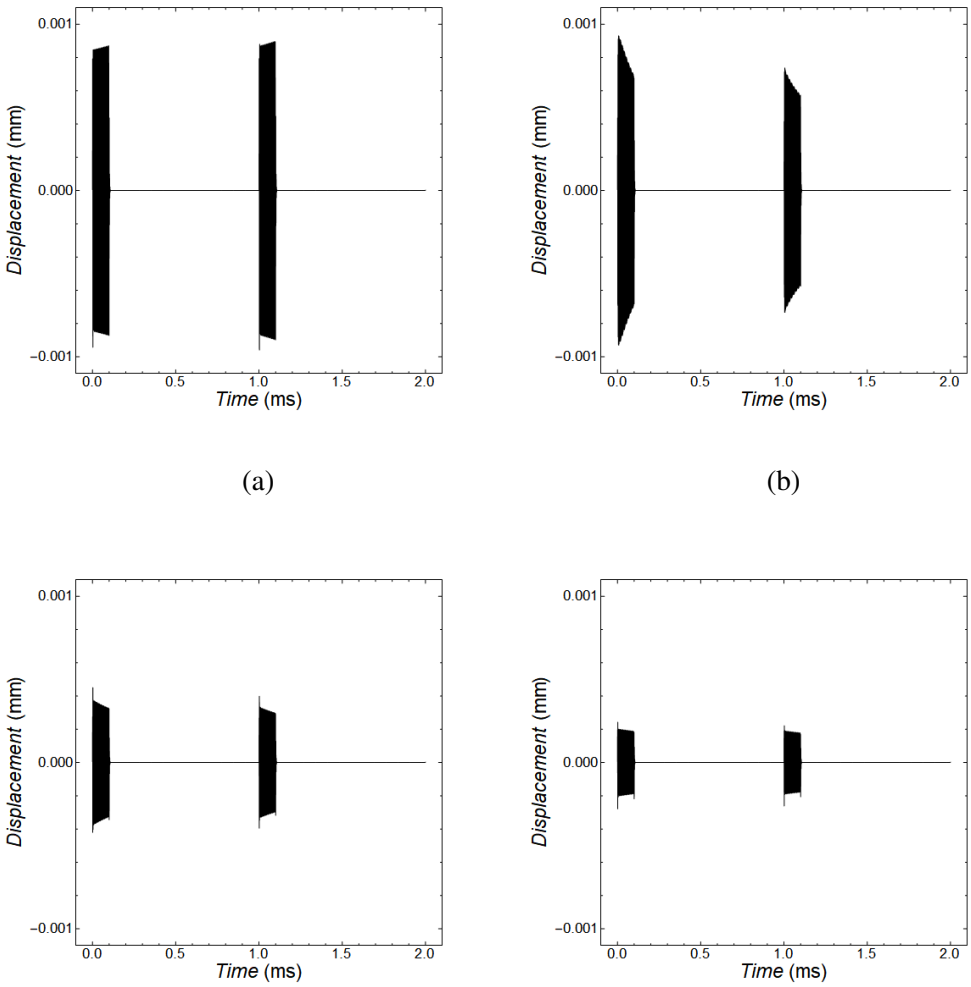

Figure 4.14: Nucleus displacement for a cancerous cell between t = 0 ms and 2 ms, with pulse duration 0.1ms and pressure 1.4MPa. The response shows resonant behavior at 500 kHz. (a) f = 300 kHz. (b) f = 500 kHz. (c) f = 670 kHz. (d) f = 800 kHz.

We proceed to study the influence of the process parameters, i.e., pressure, frequency, pulse duration, and duty cycle, on the oncotripsy effect:

- *Frequency*: In Fig. 4.21, we compare the damage evolution for a cancerous and healthy cell in the frequency range 300 to 800 kHz. For each cell, the damage is the highest in the neighborhood of their respective resonance frequency: 500kHz for the cancerous cell and 700kHz for the healthy cell. Far away from

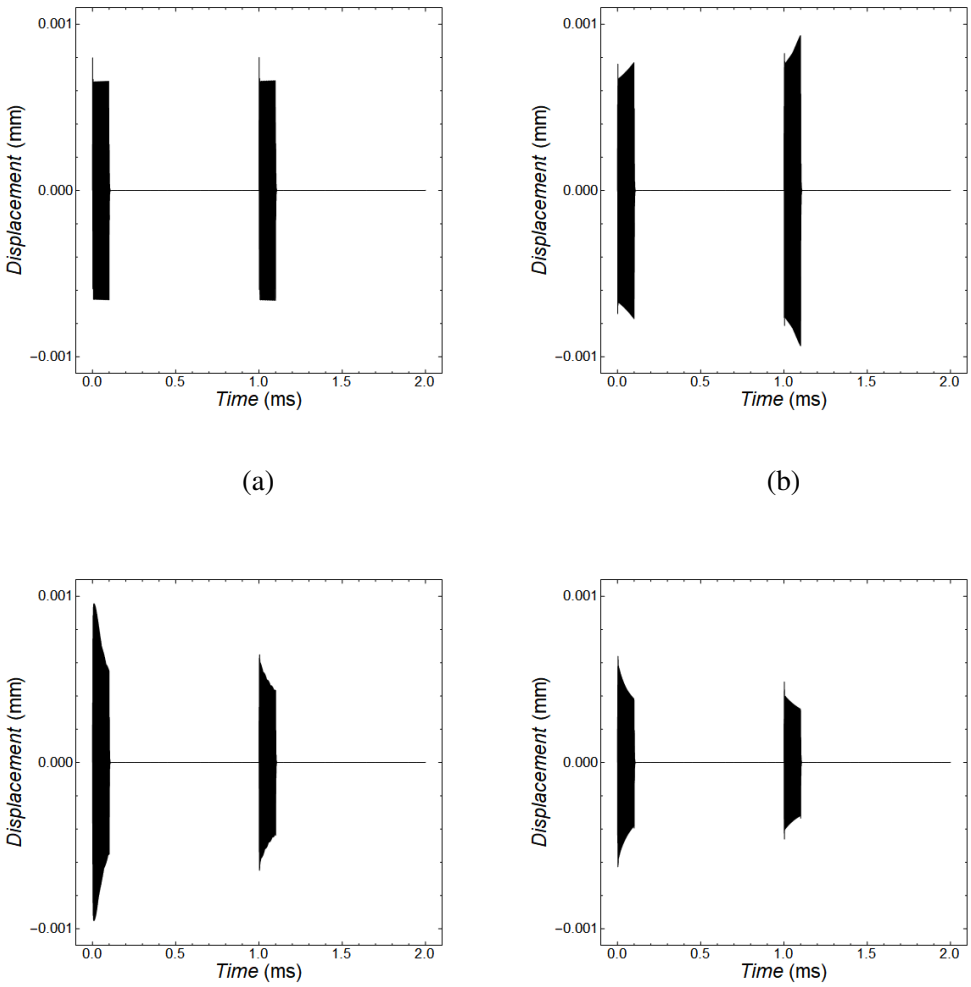

Figure 4.15: Nucleus displacement for a healthy cell between t = 0 ms and 2 ms, with pulse duration 0.1ms and pressure 1.4MPa. The response shows resonant behavior at 670 kHz. (a) f = 300 kHz. (b) f = 500 kHz. (c) f = 670 kHz. (d) f = 800 kHz.

resonance, the maximum damage attained is reduced. These results indicate that cancerous cells could be targeted at their eigenfrequencies while keeping healthy cells mostly intact.

- *Pressure*: In Fig. 4.22, we show the damage evolution for different pressures. Recall that the pressure increases the particle velocity of the field and, therefore, the axial load on the cell. As expected, the effect of increasing the pressure results in much greater accumulated damage, which implies that large pressures could lead to the death of both cancerous and healthy cells. There-

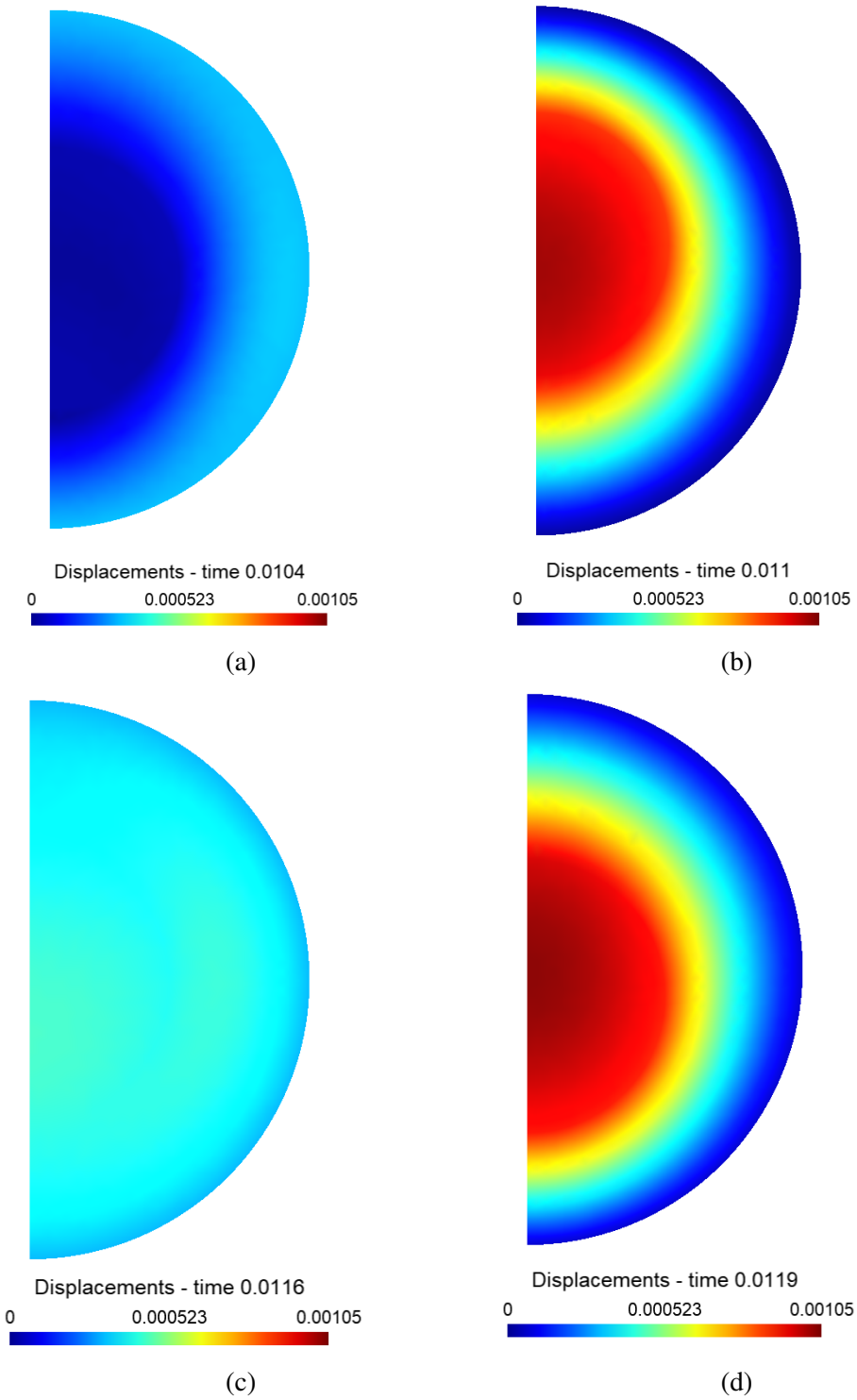

Figure 4.16: Displacements evolution (in mm) in a cycle for a cancerous cell at 500kHz, P=1.4MPa, DC=10% and PD=0.1ms. (a) t=0.0104 ms (b) t=0.0110 ms; (c) t=0.0116 ms; and (d) t=0.0119 ms.

fore, the pressure selection should guarantee that the accumulated damage on the cell is lower than the critical damage.

- *Pulse duration and duty cycle*: In Fig. 4.23a, we show the damage evolution for different pulse duration and equal duty cycle. As regards the duration of the pulse, it can be observed that even though the sinusoidal load exerts the same number of cycles on the cell at the same intensity, the cell reaches a different final state. At long pulse durations, the cell accumulates more damage than at a shorter pulse duration. This implies that, for a given critical damage q_c, a cell under a longer pulse duration would fail at a shorter time. This is a possible explanation for the same observation in the experimental results of Mittelstein *et al.* [54] work.
  In Fig. 4.23b, we show the damage evolution for different duty cycles and equal pulse duration. It is clear from these that increasing the duty cycle increases the accumulated damage.

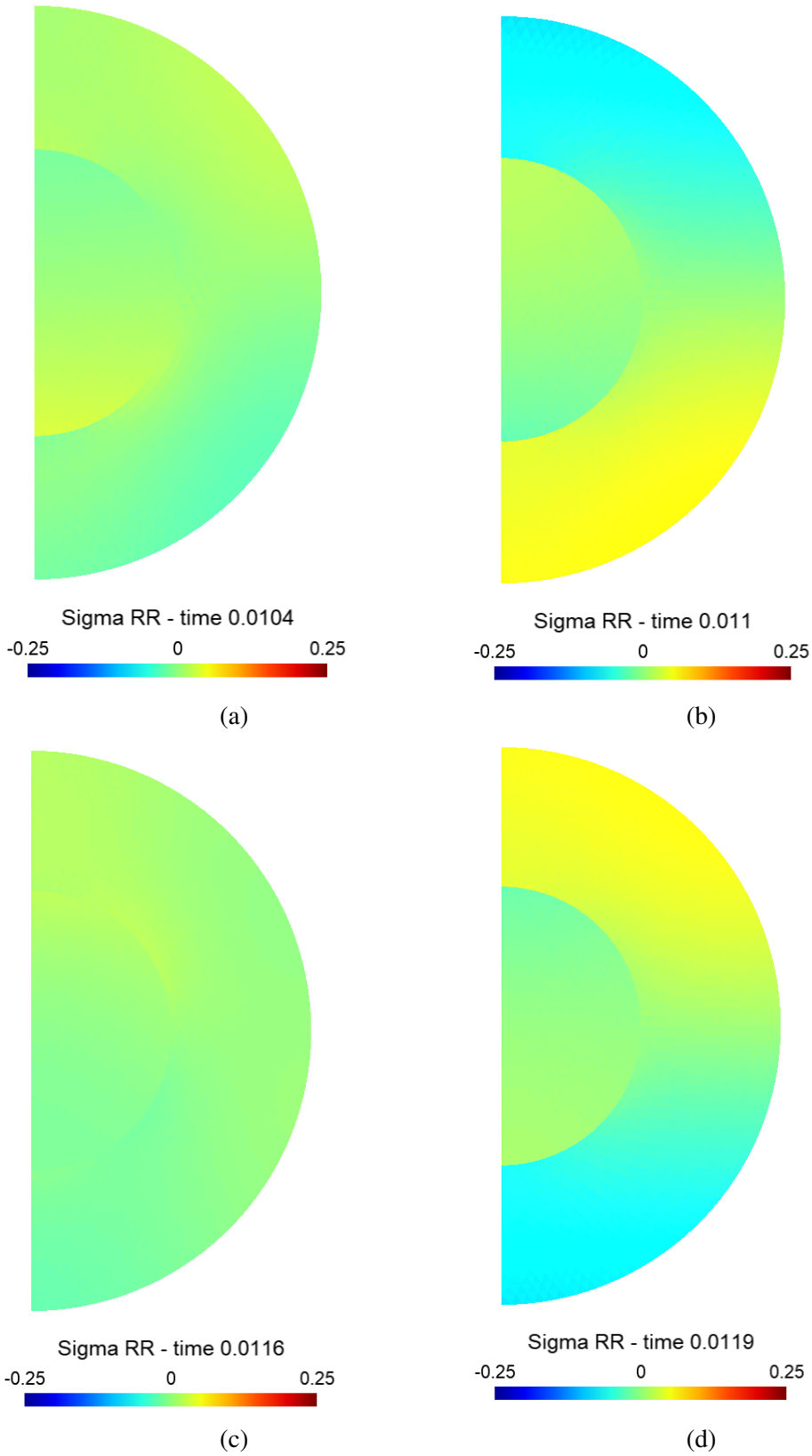

Figure 4.17: Evolution of the cauchy radial stress σ_{rr} (in MPa) in a cycle for a cancerous cell at 500kHz, P=1.4MPa, DC=10% and PD=0.1ms. (a) t=0.0104 ms (b) t=0.0110 ms; (c) t=0.0116 ms; and (d) t=0.0119 ms.

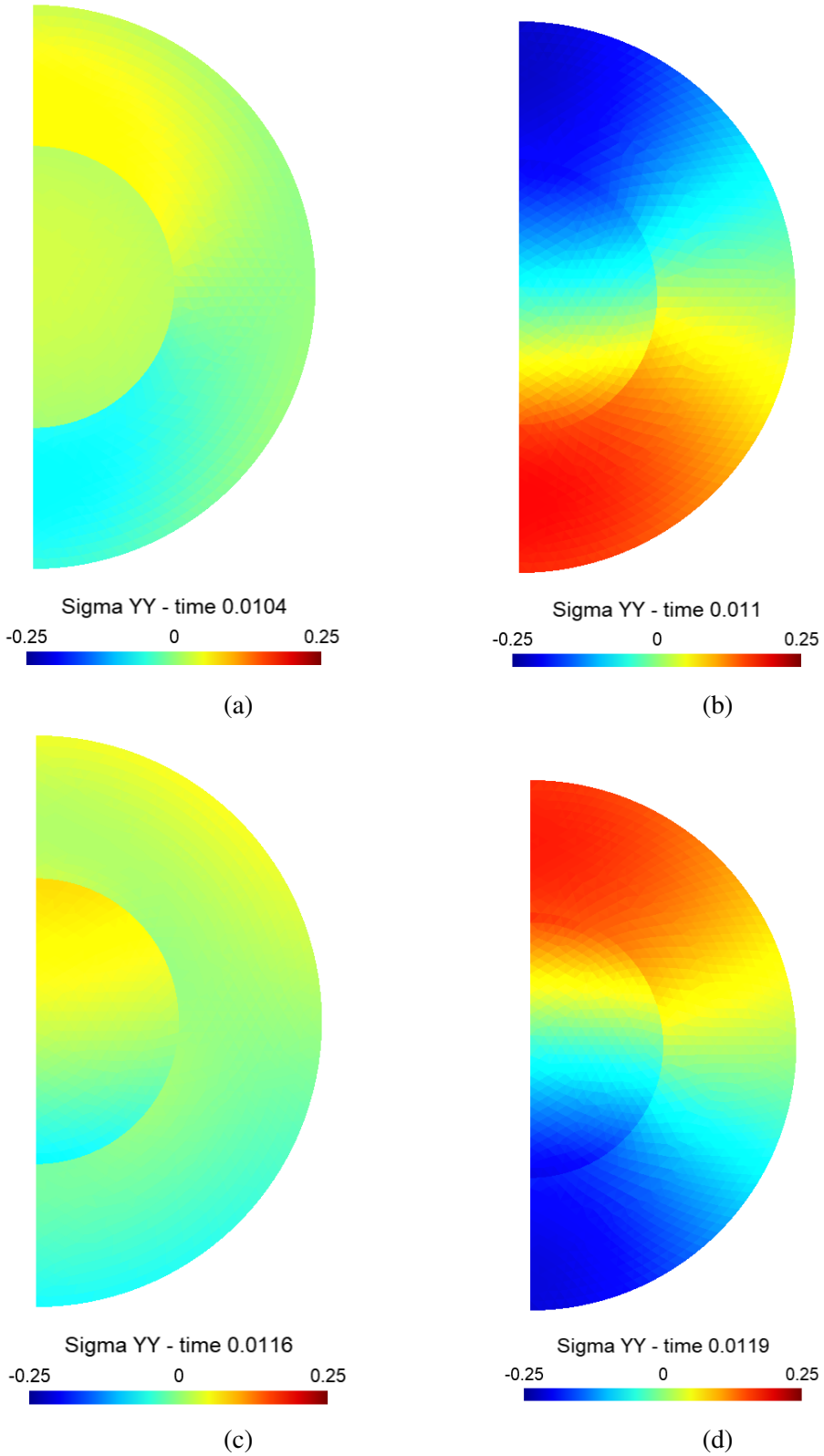

Figure 4.18: Evolution of the axial cauchy stress σ_{yy} (in MPa) in a cycle for a cancerous cell at 500kHz, P=1.4MPa, DC=10% and PD=0.1ms. (a) t=0.0104 ms (b) t=0.0110 ms; (c) t=0.0116 ms; and (d) t=0.0119 ms. The maximum stresses are located back and forth of the nucleus.

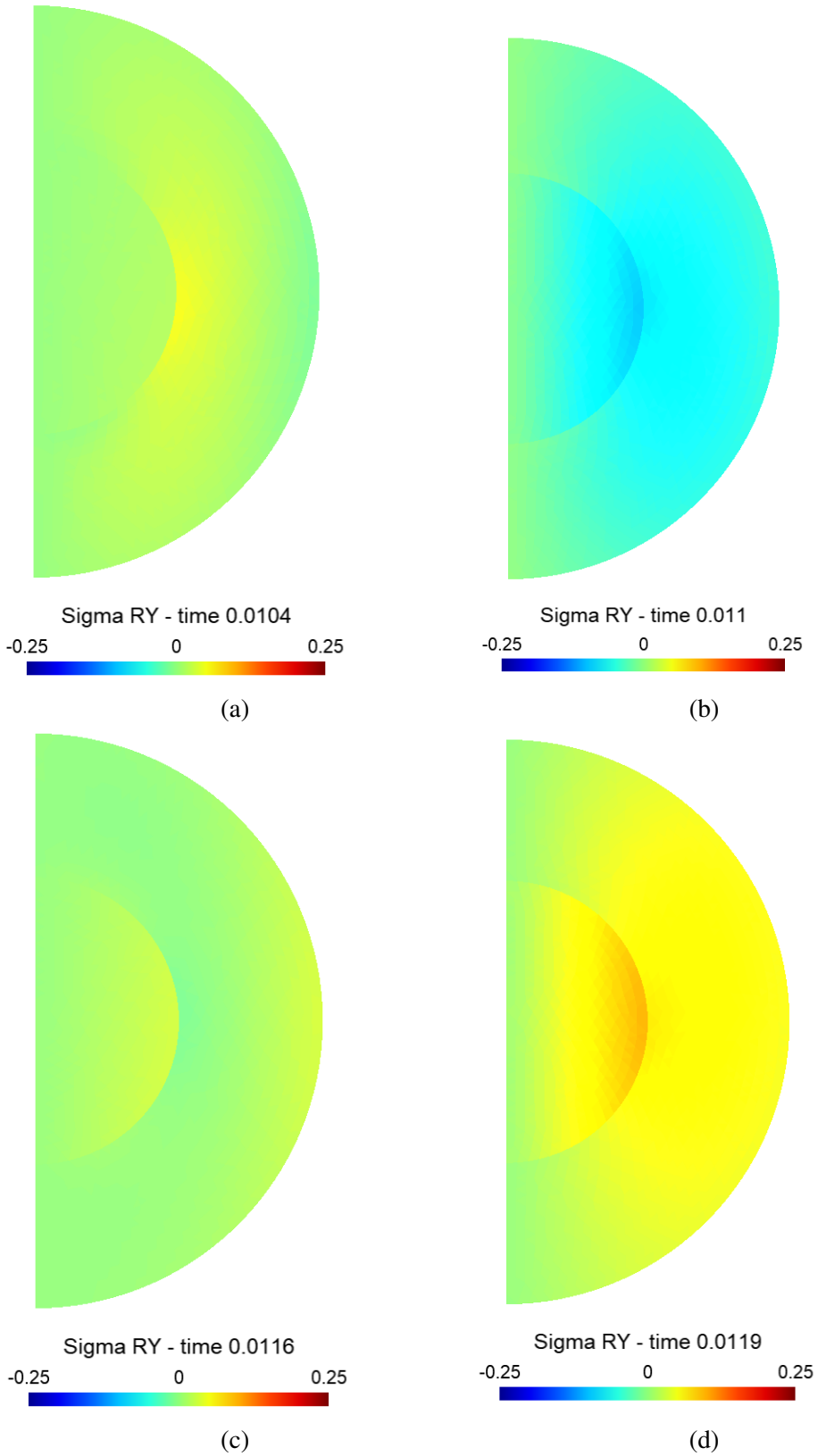

Figure 4.19: Evolution of the cauchy shear stress σ_{ry} (in MPa) in a cycle for a cancerous cell at 500kHz, P=1.4MPa, DC=10% and PD=0.1ms. (a) t=0.0104 ms (b) t=0.0110 ms; (c) t=0.0116 ms; and (d) t=0.0119 ms. The maximum shear stress attained is located at (x,y)=(0,0.0045)mm.

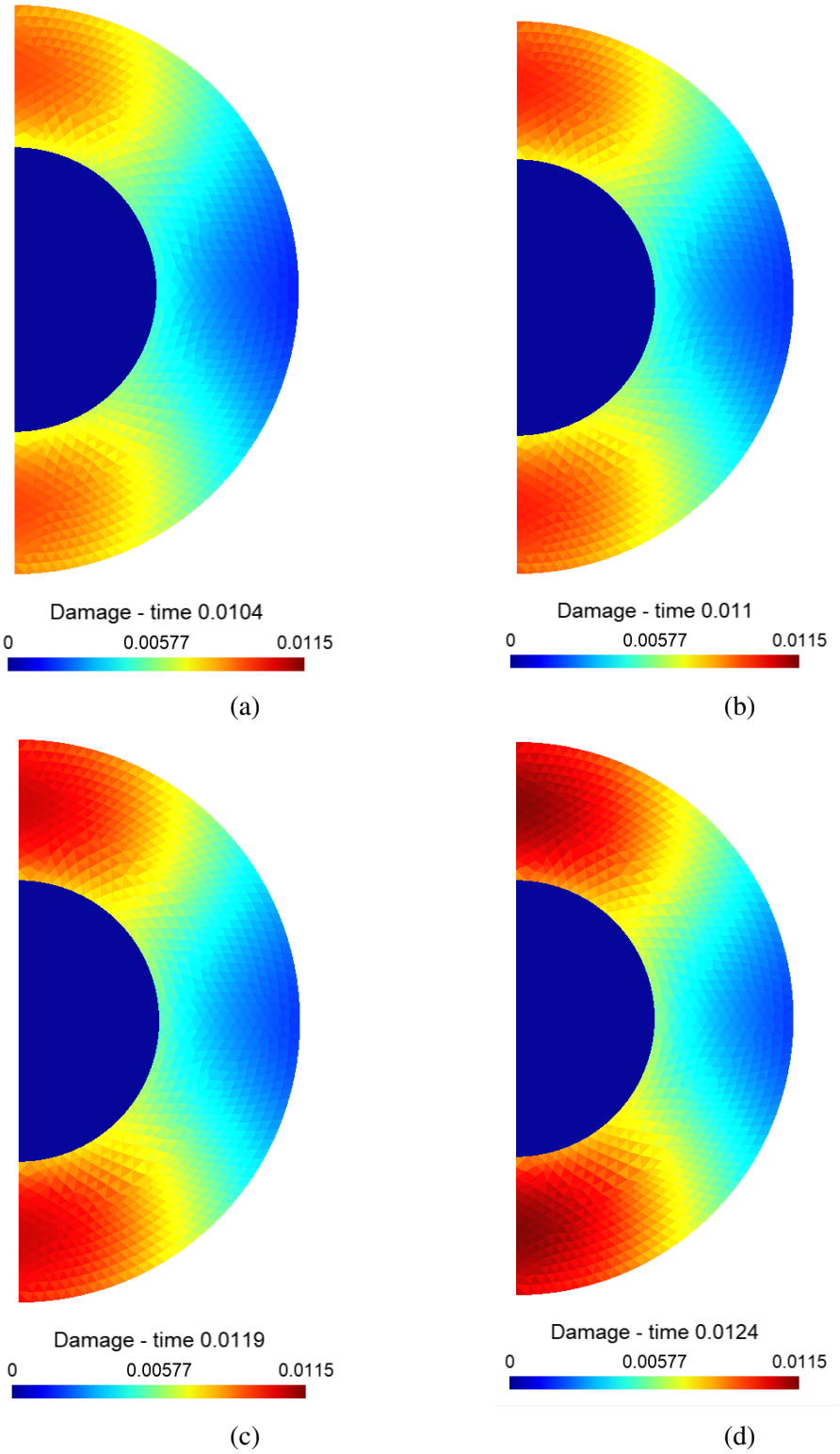

Figure 4.20: Evolution of the damage state in a cycle for a cancerous cell at 500kHz, P=1.4MPa, DC=10% and PD=0.1ms. (a) t=0.0104 ms (b) t=0.0110 ms; (c) t=0.0116 ms; and (d) t=0.0119 ms. The damage is non-uniform, propagating from the outside of the cell to the interior, and has maximums along the direction of the displacement of the nucleus.

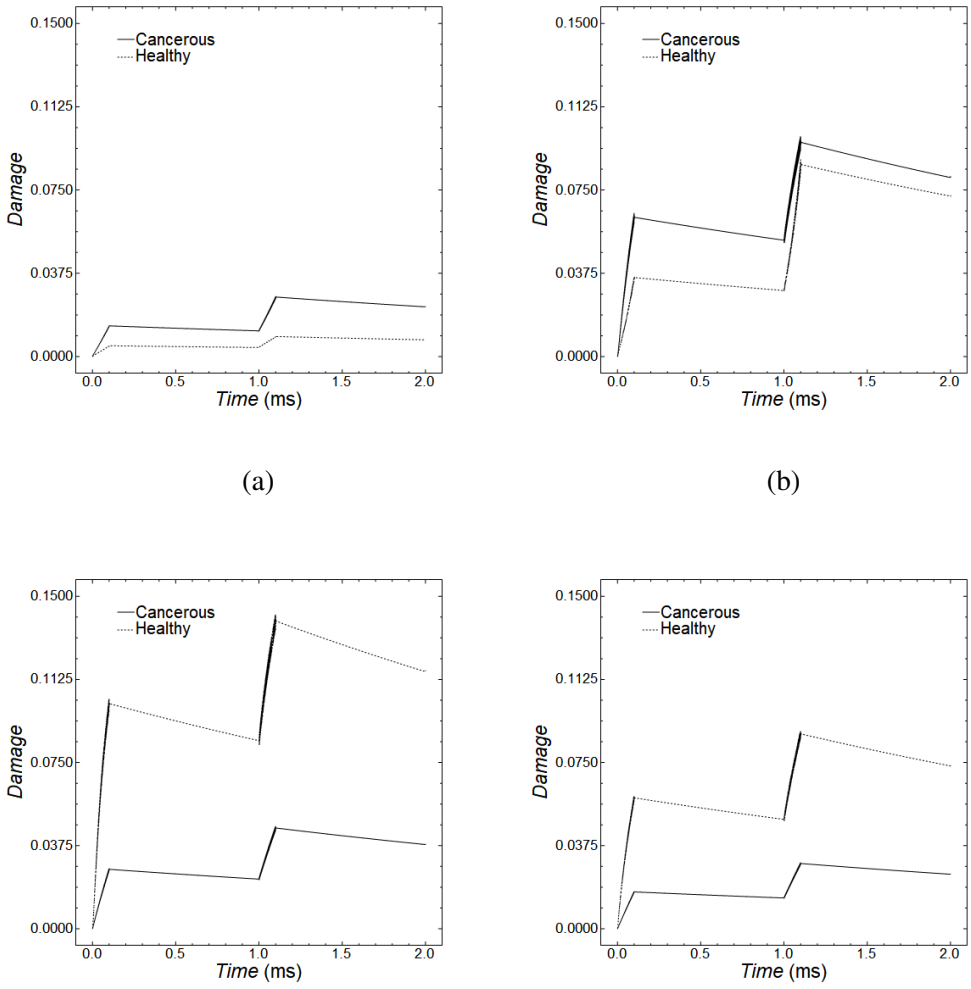

Figure 4.21: Mean damage for a cancerous and healthy cell between t = 0 ms and 2 ms, with pulse duration 0.1ms and pressure 1.4MPa. The response shows resonant in the neighborhood of 500 kHz for the cancerous cell and 700 kHz for the healthy cell. (a) f = 300 kHz. (b) f = 500 kHz. (c) f = 670 kHz. (d) f = 800 kHz.

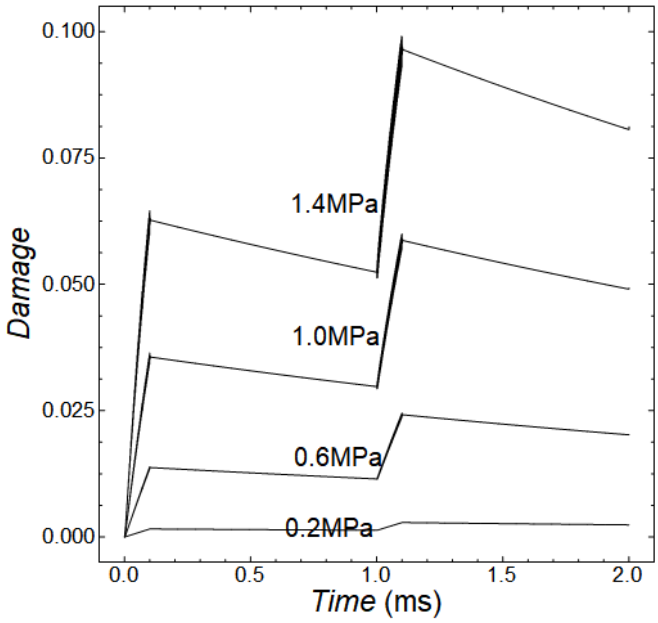

Figure 4.22: Mean damage for a cancerous and healthy cell between t = 0 ms and 2ms, with pulse duration 0.1ms and pressures 0.6 and 1.4MPa.

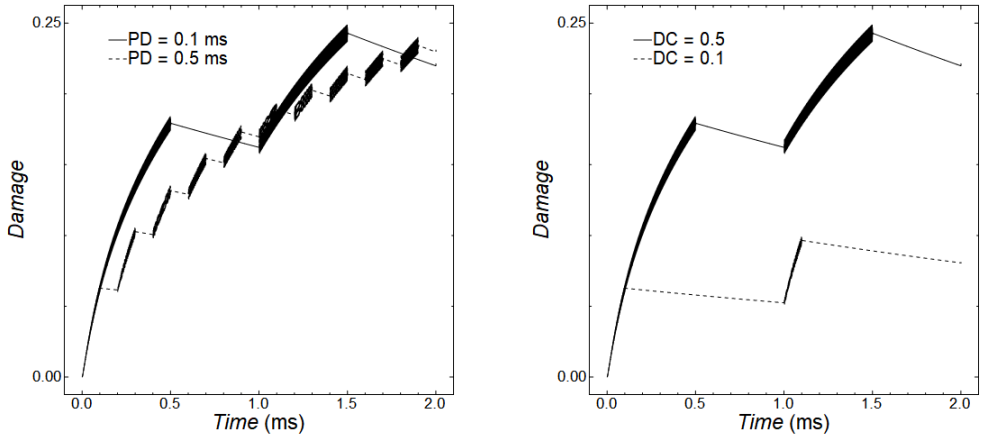

(a) (b)

Figure 4.23: Mean damage for a cancerous cell between t = 0 ms and 2 ms, under 1.4MPa and at 500kHz. (a) duty cycle 50% and pulse durations 0.1 and 0.5 ms with pulse repetition time of 0.2 and 1 ms, respectively. (b) duty cycle of 10% and 50% and pulse duration of 0.1ms with pulse repetition time of 1 and 0.2 ms, respectively.

4.7 Discussion and concluding remarks

In this chapter, we proposed a dynamical model that provides a rational basis for understanding the oncotripsy effect posited by Heyden and Ortiz [29] under the conditions of the experiments of Mittelstein *et al*. [54]. An important difference between those experiments and the scenario initially contemplated in [29] is that in the experiments of Mittelstein *et al*. [54] the cells are in aqueous suspension, whereas the analysis of Heyden and Ortiz [29] is concerned with cells embedded in a solid extracellular matrix (ECM). In aqueous suspension, the cells experience an exceedingly vicious environment, which is likely to suppress any vibrations of the cell membrane. The response of the cells to ultrasound stimulation is thus reduced to that of an internal resonator.

We also develope a finite element model (FEM) of oncotripsy mechanics. The FEM has the capability of examining the damage onset on the cytoskeleton, as well as detailed analysis of the local damage, strain, and stresses on the cell. The dynamical model exhibits the oncotripsy effect, i.e., the insonation-frequency dependence of the cell response and the window of opportunity for selective cell killing. In addition, it predicts the dependence of the dead-cell fraction curves on pulse duration observed experimentally, Fig. 2.5. Indeed, this trend is exhibited by the damage evolution curves shown in Fig. 4.23. A careful inspection of these curves shows that the maximum level of damage attained within the insonation cycles decreases as the pulse duration decreases. Thus, for long pulses, the cells have time to accumulate large amounts of damage during the on-period of the pulse. For shorter pulses, the extent of damage accumulation is comparatively less. If the pulse duration is comparable to—or smaller than—the recovery time for healing, the cell does not have sufficient time to recover during the off-period of the cycle, and the trend persists over repeated cycles. Therefore, according to the model the dependence of the dead-cell fraction curves on pulse duration is the result of a delicate interplay between the pulse repetition period and pulse duration, the cell dynamics, which determines the rate at which damage accumulates and the kinetics of cell healing, which determines the rate at which damage is restored.

The nature of the slow degeneration of the cell in the experiments is unknown. As observed in our computations, relative nucleus translation with respect to the plasma membrane probably plays an important role. Damage may onset in the plasma membrane of the cell, in particular along the direction of wave propagation, with the rupture of F-Actin and membrane failure. Sloshing of the nucleus may produce

a breakage of the internal structure. Subsequently, this complex damage evolution, which is heterogeneously distributed, implies that a cell could face several modes of death: membrane rupture, rapid cytoskeleton degeneration, or even nucleus fragmentation.

Nevertheless, this model has some limitations. One the one hand, the theoretical analysis is performed for a very simplified cell structure. For instance, the cytoskeleton was considered to respond with an effective elasticity. However, the network is far more complex, with fibers varying in thickness, length, and stiffness. The plasma membrane, nuclear envelope, and other large organelles were not considered either. On the other hand, the calculations at high frequencies and a long time of exposure are very expensive. As a reference, a simulation of the coarse axisymmetric mesh that solves for 2ms of exposure at 500kHz takes ~ 4 hours in the high-performance computer at Caltech. Thus, sensitivity analysis and calibration should be performed by means of a reduced model and, subsequently, use these results as parameters for the full finite element model calculation.

Chapter 5

REDUCED MODEL OF ONCOTRIPSY

In this chapter we develop a reduced dynamical model that approximates the three-dimensional dynamics of the cell and facilitates parameter studies, including sensitivity analysis and process optimization. The reduced dynamical system encompasses the relative motion of the nucleus with respect to the cell membrane and a state variable measuring the extent of damage to the cytoskeleton. The cell membrane is assumed to move rigidly according to the particle velocity induced in the water by the insonation. The dynamical system evolves in time as a result of structural dynamics and kinetics of cytoskeletal damage and repair. The resulting dynamics is complex and exhibits behavior on multiple time scales, including the period of vibration and attenuation, the characteristic time of cytoskeletal healing, the pulsing period and the time of exposure to the ultrasound. We show that this multi-time scale response can effectively be accounted for by recourse to WKB asymptotics and methods of weak convergence. We also account for cell variability and estimate the attendant variance of the time-to-death of a cell population using simple linear sensitivity analysis. The reduced dynamical model predicts, analytically up to quadratures, the response of a cell population to LIPUS as a function of fundamental cell properties and process parameters. We show, by way of partial validation, that the reduced dynamical model indeed predicts—and provides a conceptual basis for understanding—the oncotripsy effect and other trends in the data of Mittelstein *et al.* [54], including the dependence of cell-death curves to pulse duration and duty cycle.

5.1 Reduced model of Oncotripsy

Elasticity

In Chapter 4, we obtained the free-energy density per unit volume of the cytoskeleton as

$$A(\mathbf{F},T)=\frac{\mu(T)}{2}K_{IJ}(C_{IJ}+C_{IJ}^{-1}), \tag{5.1}$$

where $\mu(T)$ is a temperature-dependent shear modulus, $\mathbf{F}$ is the local deformation gradient, $\mathbf{C}=\mathbf{F}^T\mathbf{F}$ is the right Cauchy-Green deformation tensor, and T is the

absolute temperature. In addition, the structure tensor **K** in (5.1) follows as

$$K_{IJ} = \int_{S^2} p(\xi)\xi_I\xi_J \, d\Omega, \tag{5.2}$$

where ξ is the unit vector pointing from one end of the fiber to the other, or *fiber direction*, $p(\xi)$ is the fraction of chains in the ensemble of direction ξ, S^2 is the unit sphere and $d\Omega$ is the element of solid angle. The density $p(\xi)$ is subject to the normalization condition

$$\int_{S^2} p(\xi) \, d\Omega = 1. \tag{5.3}$$

The distribution function $p(\xi)$ describes the structure of the cytoskeletal network and is assumed fixed and known. In addition, the thermodynamic driving forces for damage followed as

$$f(\xi) = -\frac{\partial A}{\partial q(\xi)} = -\alpha^* q(\xi) = p(\xi)\Big(\mu(T)(1-q(\xi))(\lambda^2(\xi)+\lambda^{-2}(\xi)-2) - \beta^* q(\xi)\Big) \tag{5.4}$$

with α^* and β^* the kinematic parameters.

Viscosity

Another source of resistance to cell deformation arises from the viscosity of the cytoplasm. Assuming linear viscosity, the viscous Cauchy stress in the cytoplasm follows as

$$\sigma^v_{ij} = \eta(v_{i,j} + v_{j,i}) + \left(\kappa - \frac{2}{3}\eta\right) \operatorname{div} v \, \delta_{ij}, \tag{5.5}$$

where η is the shear viscosity, κ is the bulk viscosity, v is the velocity field, a comma denotes partial differentiation, and div v is the divergence of the velocity field.

Displacements

We develop a reduced dynamical model of cell deformation and damage based on the following assumptions:

i) Spherical geometry of cell and nucleus.

ii) Rigid translational motion of the cell membrane.

iii) Heavy and rigid nucleus.

iv) *Ansätze* for the cytoplasm deformation and damage fields.

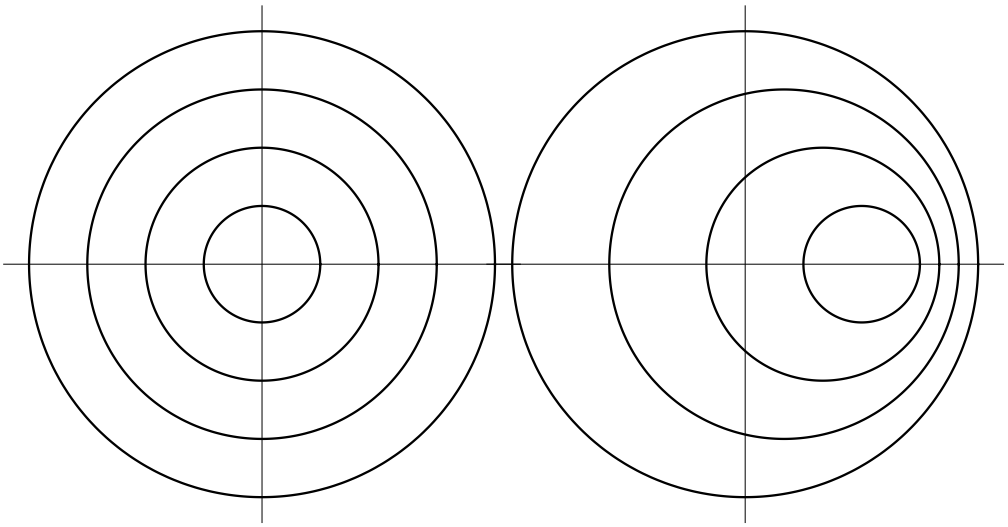

(a) (b)

Figure 5.1: Deformation *ansatz* used in model reduction. a) Cross section of the reference configuration of the cell, showing nucleus (inner circle) and two concentric material spheres to aid in the visualization of the deformation. b) Deformed configuration of the cell after a displacement of the nucleus.

We note that, under the conditions of interest here, a Rayleigh treatment of the cell dynamics is justified in view of the large wavelength of the ultrasound waves compared to the cell size.

We specifically consider a spherical cell of radius b containing a concentric spherical nucleus of radius a. We assume that the cell moves under the action of planar waves and executes a translational motion according to the particle velocity of the aqueous medium. We attach a moving cartesian reference frame to the center of the cell such that the x_3 axis is aligned with the direction of motion. We additionally introduce a spherical coordinate system (r, φ, θ), such that

$$x_1 = r\ \sin\theta\ \cos\varphi, \qquad x_2 = r\ \sin\theta\ \sin\varphi, \qquad x_3 = r\ \cos\theta, \tag{5.6}$$

where r is the radius, φ is the azimuthal angle, and θ is the inclination. In these spherical coordinates, the domain of the cytoplasm in its undeformed configuration is $\varphi \in [0, 2\pi)$, $\theta \in [0, \pi)$, and $r \in [a, b]$. The nucleus is assumed to translate rigidly through a time-dependent displacement $u(t)$ relative to the cell membrane. In addition, a material point in the cytoplasm initially at location (x_1, x_2, x_3) in the undeformed configuration is assumed to be at location

$$y_1 = x_1, \qquad y_2 = x_2, \qquad y_3 = x_3 + \frac{b - r}{b - a}\, u(t), \tag{5.7}$$

following the displacement of the nucleus. In this *ansatz*, a spherical material shell of radius r in the undeformed configuration translates rigidly to another spherical shell of the same radius centered at $u(t)\,(b-r)/(b-a)$ following the displacement of the nucleus, cf. Fig. 5.1.

Dynamics without damage

Inserting this *ansatz* into the free-energy density (5.1) and assuming small relative displacements $u(t)$, we obtain, after a trite calculation,

$$A = \frac{\mu}{2}\frac{u^2(t)}{(b-a)^2}(3+\cos\theta), \tag{5.8}$$

and the total free energy of the cytoskeleton evaluates to

$$\mathcal{A}(u(t)) = \int_0^{2\pi}\int_0^{\pi}\int_a^b Ar^2\sin\theta\,dr\,d\theta\,d\varphi = \frac{16\pi}{9}(b^3-a^3)\mu\frac{u^2(t)}{(b-a)^2}, \tag{5.9}$$

which, in the absence of damage, supplies a potential for the relative displacement of the nucleus. Likewise, the velocity field of the cytoplasm follows by time differentiation of the *ansatz* (5.7), with the result

$$v_1 = 0, \qquad v_2 = 0, \qquad v_3 = \frac{b-r}{b-a}\,\dot{u}(t). \tag{5.10}$$

Inserting this velocity field into the viscosity law (5.5) and assuming small relative displacements of the nucleus gives, after a straightforward calculation, the dissipation per unit undeformed volume is

$$D = \frac{1}{2}\sigma_{ij}v_{i,j} = \frac{1}{24}\big(5\eta+6\kappa-(\eta-6\kappa)\cos(2\theta)\big)\frac{\dot{u}^2(t)}{(b-a)^2}, \tag{5.11}$$

and the total dissipation follows as

$$\mathcal{D}(\dot{u}(t)) = \int_0^{2\pi}\int_0^{\pi}\int_a^b Dr^2\sin\theta\,dr\,d\theta\,d\varphi = \frac{2\pi}{27}(b^3-a^3)(4\eta+3\kappa)\frac{\dot{u}^2(t)}{(b-a)^2}. \tag{5.12}$$

Finally, the total kinetic energy of the cell follows as

$$\mathcal{K}(t,\dot{u}(t)) = \frac{1}{2}\Big(m_0+\frac{2\pi}{15}\rho(b-a)(6a^2+3ab+b^2)\Big)(v(t)+\dot{u}(t))^2, \tag{5.13}$$

where m_0 is the mass of the nucleus, ρ is the density of the cytoplasm and $v(t)$ is the prescribed velocity of the cell membrane. An appeal to the Lagrange-D'Alembert principle gives the equation of motion

$$\frac{d}{dt}\frac{\partial\mathcal{K}}{\partial\dot{u}}(t,\dot{u}(t)) + \frac{\partial\mathcal{D}}{\partial\dot{u}}(\dot{u}(t)) + \frac{\partial\mathcal{A}}{\partial u}(u(t)) = 0. \tag{5.14}$$

Inserting (5.9), (5.12) and (5.13) into (5.14), we obtain

$$m\ddot{u}(t) + c\dot{u}(t) + ku(t) = -m\dot{v}(t), \tag{5.15}$$

where

$$m = m_0 + \frac{2\pi}{15}\rho(b-a)(6a^2+3ab+b^2), \quad c = \frac{4\pi}{27}\frac{b^3-a^3}{(b-a)^2}(4\eta+3\kappa), \quad k = \frac{32\pi}{9}\frac{b^3-a^3}{(b-a)^2}\mu, \tag{5.16}$$

are the total mass, damping coefficient and stiffness of the cell. Eq. (5.15) represents a damped and forced harmonic oscillator, with the material velocity $v(t)$ of the aqueous medium supplying the forcing.

Dynamics with damage

Suppose now that the cell undergoes damage. In general, damage patterns may be expected to arise at two levels: inhomogeneously over the cytoplasm; and damage along with preferential directions at every material point. Such a degree of complexity requires a full three-dimensional analysis for its elucidation. In order to simplify the dynamics, we simply assume that damage is isotropic at all material points, i.e., the damage parameter q is independent of direction ξ; and independent of position over the cytoskeleton. By this simple *ansatz*, the state of damage of the cell is characterized by a single state variable $q(t)$. An immediate extension of (5.9) then gives the total free energy of the cell as

$$\mathcal{A}(u(t), q(t)) = \frac{16\pi}{9}(b^3-a^3)(1-q(t))^2\mu\frac{u^2(t)}{(b-a)^2} + \frac{4\pi}{3}(b^3-a^3)\frac{\beta^*}{2}q^2(t). \tag{5.17}$$

Likewise, the total dissipation (5.12) extends to

$$\mathcal{D}(\dot{u}(t), \dot{q}(t)) = \frac{2\pi}{27}(b^3-a^3)(4\eta+3\kappa)\frac{\dot{u}^2(t)}{(b-a)^2} + \frac{4\pi}{3}(b^3-a^3)\frac{\alpha^*}{2}\dot{q}^2(t). \tag{5.18}$$

The Lagrange-D'Alembert principle then gives the coupled equations

$$\frac{d}{dt}\frac{\partial\mathcal{K}}{\partial\dot{u}}(t,\dot{u}(t)) + \frac{\partial\mathcal{D}}{\partial\dot{u}}(\dot{u}(t),\dot{q}(t)) + \frac{\partial\mathcal{A}}{\partial u}(u(t),q(t)) = 0, \tag{5.19a}$$

$$\frac{\partial\mathcal{D}}{\partial\dot{q}}(\dot{u}(t),\dot{q}(t)) + \frac{\partial\mathcal{A}}{\partial q}(u(t),q(t)) = 0. \tag{5.19b}$$

Inserting (5.17), (5.18) and (5.13) into (5.19), we now obtain

$$m\ddot{u}(t) + c\dot{u}(t) + (1-q(t))^2ku(t) = -m\dot{v}(t), \tag{5.20a}$$

$$\alpha\dot{q}(t) + \beta q(t) = (1-q(t))ku^2(t), \tag{5.20b}$$

with m, c and k as before, and the kinematic parameters, α and β are

$$\alpha = \frac{4\pi}{3}(b^3 - a^3)\alpha^* \quad \text{and} \quad \beta = \frac{4\pi}{3}(b^3 - a^3)\beta^*. \tag{5.21}$$

The first of these equations represents a forced and damped harmonic oscillator in which the stiffness depends on the instantaneous state of damage. The second governs the kinetic evolution of damage state, including damage accumulation and healing.

WKB dynamics

Under the conditions of interest here, the dynamics described by the system (5.19) is characterized by two disparate time scales: the period of oscillation and the characteristic time for damage evolution, the former much smaller than the latter. This two-time structure suggests analyzing the problem by means of WKB asymptotics [6].

We consider a generic duty cycle such as shown inset in Fig. 2.3a, starting at time t_0 and consisting of an on-period ending at time t_1 and an off-period ending at time t_2. The duration of the on-period, or pulse duration, is $T_1 = t_1 - t_0$, the duration of the off-cycle, or listening time, is $T_2 = t_2 - t_1$ and the total duration of the duty cycle, or pulse repetition period, is $T = t_2 - t_0$. We specifically assume harmonic excitation of the form

$$v(t) = V\mathrm{e}^{i\omega t}, \tag{5.22}$$

during the on-period and $v(t) = 0$ during the off-period. In (5.22), V is a complex amplitude and ω is the insonation frequency.

We begin by analyzing the equation of motion (5.20a), which we rewrite in the form

$$\ddot{u}(t) + 2\zeta\omega_0\dot{u}(t) + (1 - q(t))^2\omega_0^2 u(t) = -\dot{v}(t), \tag{5.23}$$

where $\omega_0 = \sqrt{k/m}$ is the *natural frequency* of the undamaged cell and ζ is the *damping ratio*. During the on-period of the duty cycle, we have

$$\ddot{u}(t) + 2\zeta\omega_0\dot{u}(t) + (1 - q(t))^2\omega_0^2 u(t) = -i\omega V\mathrm{e}^{i\omega t}, \tag{5.24}$$

where, for convenience, we extend the equation to the complex domain. Assume now that the period of oscillation $T_0 = 2\pi/\omega_0$ is much smaller than the pulse duration T_1. Assume additionally that the frequency ω of insonation is comparable to ω_0. Finally, suppose that the variation of the damage state variable $q(t)$ is slow and on

the scale of the pulse duration of T_1. Under these conditions, the solution $u(t)$ can be obtained by performing a WKB asymptotic analysis in the small parameter T_0/T_1. We note that for fixed $q(t)$, eq. (5.24) is a linear second-order ordinary differential equation and, therefore, its solution is the sum of the general homogeneous solution and a particular solution. Because of the presence of damping, with damping coefficient ζ of $O(1)$, the homogeneous solution decays on the scale of T_0 and can be safely neglected. We seek a particular equation of the form

$$u(t) = A(t)\mathrm{e}^{i\omega t}, \tag{5.25a}$$

$$\dot{u}(t) = (\dot{A}(t) + i\omega A(t))\mathrm{e}^{i\omega t}, \tag{5.25b}$$

$$\ddot{u}(t) = (\ddot{A}(t) + 2i\omega\dot{A}(t) - \omega^2 A(t))\mathrm{e}^{i\omega t}. \tag{5.25c}$$

Inserting these expressions into (5.24) and retaining leading-order terms only, we obtain

$$-\omega^2 A(t) + 2i\zeta\omega_0\omega A(t) + (1 - q(t))^2\omega_0^2 A(t) = -i\omega V. \tag{5.26}$$

Solving for the amplitude $A(t)$, we find

$$A(t) = \frac{i\omega V}{\omega^2 - (1 - q(t))^2\omega_0^2 - 2i\zeta\omega_0\omega}. \tag{5.27}$$

Finally, inserting into (5.25a) we obtain

$$u(t) = \frac{i\omega V\mathrm{e}^{i\omega t}}{\omega^2 - (1 - q(t))^2\omega_0^2 - 2i\zeta\omega_0\omega}, \tag{5.28}$$

asymptotically as $T_0/T_1 \to 0$. We observe from (5.28) that the nucleus executes rapid oscillations relative to the cell membrane over the pulse duration in sync with the ultrasound excitation, with amplitude modulated by the damage variable $q(t)$.

Next, we turn to the damage evolution equation (5.20b). Inserting solution (5.28) into (5.20b) gives

$$\alpha\dot{q}(t) + \beta q(t) = k\frac{(1 - q(t))\omega^2|V|^2}{\left(\omega^2 - (1 - q(t))^2\omega_0^2\right)^2 + 4\zeta^2\omega_0^2\omega^2}, \tag{5.29}$$

which is now fully expressed in terms of the damage variable $q(t)$. Conveniently, eq. (5.29) is separable and admits the explicit solution

$$t = t_0 + \int_{q_0}^{q} \frac{\alpha\, d\xi}{k\dfrac{(1 - \xi)\omega^2|V|^2}{\left(\omega^2 - (1 - \xi)^2\omega_0^2\right)^2 + 4\zeta^2\omega_0^2\omega^2} - \beta\xi}, \tag{5.30}$$

where we write $q_0 = q(t_0)$. Alternatively, the equation of evolution (5.29) can be recast in terms of dimensionless variables as

$$\frac{dq}{d\tau}(\tau) + q(\tau) = \frac{(1 - q(t))w^4\varepsilon}{\left(w^2 - (1 - q(\tau))^2\right)^2 + 4\zeta^2 w^2}, \tag{5.31}$$

where

$$\tau = \frac{t - t_0}{t_r}, \qquad t_r = \frac{\alpha}{\beta}, \qquad w = \frac{\omega}{\omega_0}, \qquad \varepsilon = \frac{k|V|^2}{\beta\omega^2} \tag{5.32}$$

whereupon (5.30) becomes

$$\tau = \int_{q_0}^{q} \frac{d\xi}{\dfrac{(1 - \xi)w^4\varepsilon}{\left(w^2 - (1 - \xi)^2\right)^2 + 4\zeta^2 w^2} - \xi}. \tag{5.33}$$

From this reparametrization, we observe that the evolution of damage depends on the following dimensionless parameters: i) the ratio of the elapsed time to the relaxation time t_r for healing, ii) the ratio w between the frequency of insonation and the undamaged natural frequency, iii) the energy deposited by insonation relative to the energy cost of repair, and iv) the cell damping ratio. It is also interesting to note that the damage state variable attains a steady-state maximum value $q_{\max}$ when

$$q_{\max} = \frac{(1 - q_{\max})w^4\varepsilon}{\left(w^2 - (1 - q_{\max})^2\right)^2 + 4\zeta^2 w^2}, \tag{5.34}$$

which expresses a balance between damage accumulation and healing. From this relation, the energy intensity required to attain a maximum level of damage $q_{\max}$ follows as

$$\varepsilon(q_{\max}) = \frac{\left(w^2 - (1 - q_{\max})^2\right)^2 + 4\zeta^2 w^2}{w^4} \frac{q_{\max}}{1 - q_{\max}}. \tag{5.35}$$

As expected, $\varepsilon(q_{\max})$ reduces to zero as $q_{\max} \to 0$ and diverges to infinity as $q_{\max} \to 1$. We also note that, by virtue of the existence of a steady state at $q_{\max}$, the integral in (5.33) is well-defined and finite in the range $q_0 \leq q < q_{\max}$ and diverges to infinity at $q = q_{\max}$, indicating that the steady state is attained only asymptotically at infinite time.

Fig. 5.2 shows an example of the WKB dynamics just elucidated for parameters: $t_r = 1$, $\omega = \omega_0 = 100$, $\zeta = 1$, $q_{\max} = 1/2$. As may be seen from Fig. 5.2, the state of damage of the cell evolves on the scale of the relaxation time t_r for healing and tends asymptotically to $q_{\max}$. The relative displacement of the nucleus is damped out on the shorter time scale $1/\zeta\omega_0$ and simultaneously amplified by the loss of stiffness due to damage on the time scale t_r. The competition between these two opposing

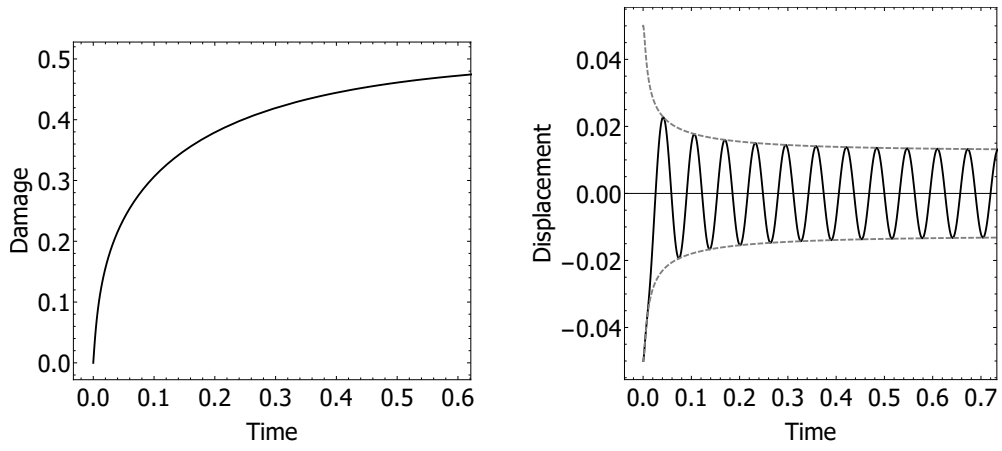

(a) (b)

Figure 5.2: Example of cell response to harmonic excitation. a) Damage state variable *vs*. time. b) Relative nucleus displacement and amplitude *vs*. time. Parameters: $t_r = 1$, $\omega = \omega_0 = 100$, $\zeta = 1$, $q_{\max} = 1/2$.

effects results in a well-defined steady-state amplitude, which follows from (5.26) by taking the limit of $q(t) \to q_{\max}$. Correspondingly, the phase-space trajectory $(u(t), \dot{u}(t))$ converges to a stable limit cycle. The ability of WKB asymptotics to characterize the fast oscillations of the system and their slow modulation in time is remarkable.

During the off period, the governing equations (5.20) reduce to

$$m\ddot{u}(t) + c\dot{u}(t) + (1 - q(t))^2 ku(t) = 0, \tag{5.36a}$$

$$\alpha\dot{q}(t) + \beta q(t) = 0. \tag{5.36b}$$

Again, we assume that the duration T_2 of the off-period is much larger than the natural period of vibration T_0. Under these assumptions, in off-period we have

$$u(t) = 0, \qquad q(t) = q_1 \mathrm{e}^{-(t-t_1)/t_r}, \tag{5.37}$$

outside a short transient decaying on the scale of T_0 immediately following t_1. Thus, modulo short transients during the off-period the cell is quiescent and repairs itself exponentially on the time scale of t_r.

Fractional-step approximation of high-cycle limit

Of special interest is the case in which the amount of damage accumulated over each duty cycle is small. Thus, in the experiments of Mittelstein *et al*. [54] the death of a significant fraction of the population requires the application of a large

number of duty cycles of insonation. Correspondingly, the number of insonation pulses required to cause cell death is large, i.e., $T/t_r \ll 1$. We proceed to obtain a combined equation of evolution describing the evolution of the system over larger numbers of duty cycles, or high-cycle limit. The combined equation of evolution follows by an appeal to the method of fractional steps [83].

We recall that the duty cycle under consideration consists of an on-period of scaled duration $\tau_1 = T_1/t_r$ and an off-period of scaled duration $\tau_2 = T_2/t_r$. The entire scaled duration of the duty cycle is $\tau_1 + \tau_2$. Assuming $\tau_1 \ll 1$, over a single on-period (5.31) gives

$$q_1 \approx q_0 + \tau_1 \left(\frac{(1-q_0)w^4\varepsilon}{\left(w^2-(1-q_0)^2\right)^2 + 4\zeta^2 w^2} - q_0 \right). \tag{5.38}$$

Likewise, with $\tau_2 \ll 1$ over the subsequent off-period (5.36b) gives

$$q_2 \approx (1-\tau_2)q_1. \tag{5.39}$$

Compounding the preceding relations and keeping terms of first order in τ_1 and τ_2 gives

$$q_2 \approx q_0 + \tau_1 \left(\frac{(1-q_0)w^4\varepsilon}{\left(w^2-(1-q_0)^2\right)^2 + 4\zeta^2 w^2} - q_0 \right) - \tau_2 q_0. \tag{5.40}$$

Rearranging terms gives the relation

$$\frac{q_2 - q_0}{\tau_1 + \tau_2} \approx \lambda \left(\frac{(1-q_0)w^4\varepsilon}{\left(w^2-(1-q_0)^2\right)^2 + 4\zeta^2 w^2} - q_0 \right) - (1-\lambda)q_0, \tag{5.41}$$

where

$$\lambda = \frac{\tau_1}{\tau_1 + \tau_2}, \qquad 1 - \lambda = \frac{\tau_2}{\tau_1 + \tau_2}, \tag{5.42}$$

are the on-time fraction of the duty cycle, or duty factor, and the off-time fraction, respectively. Formally passing to the limit in (5.41) gives the differential equation

$$\frac{dq}{d\tau}(\tau) + q(\tau) = \frac{\lambda(1-q(\tau))w^4\varepsilon}{\left(w^2-(1-q(\tau))^2\right)^2 + 4\zeta^2 w^2}, \tag{5.43}$$

which approximates slow damage evolution over larger numbers of duty cycles, or high-cycle limit. Again, the differential equation (5.43) is separable with solution

$$\tau = \int_0^q \frac{d\xi}{\dfrac{\lambda(1-\xi)w^4\varepsilon}{\left(w^2-(1-\xi)^2\right)^2 + 4\zeta^2 w^2} - \xi}, \tag{5.44}$$

which is explicit up to a quadrature. As in the case of persistent insonation, we note that the system attains a steady state at a maximum level of damage

$$q_{\max} = \frac{\lambda(1-q_{\max})w^4\varepsilon}{\left(w^2-(1-q_{\max})^2\right)^2+4\zeta^2w^2}, \tag{5.45}$$

at which point damage accumulation and healing balance each other. The energy intensity required to attain a maximum level of damage $q_{\max}$ follows as

$$\varepsilon(q_{\max},\lambda) = \frac{\left(w^2-(1-q_{\max})^2\right)^2+4\zeta^2w^2}{\lambda w^4}\frac{q_{\max}}{1-q_{\max}}. \tag{5.46}$$

As expected, $\varepsilon(q_{\max},\lambda)$ reduces to zero as $\lambda \to 0$ and reduces to (5.35) for $\lambda = 1$. We also note that the integral in (5.44) is well-defined and finite in the range $q_0 \le q < q_{\max}$ and diverges to infinity at $q = q_{\max}$, indicating that the steady state is attained only asymptotically.

The convergence of the damage evolution to the high-cycle limit as the pulse repetition period T becomes much smaller than the characteristic time t_r for healing is illustrated in Fig. 5.3, which corresponds to the choice of parameters: $t_r = 10$, $\lambda = 1/10$, $\omega = \omega_0 = 100$, $\zeta = 1/10$, $q_{\max} = 1/2$. Figs. 5.3a-c show the evolution of the damage state variable obtained by solving directly the WKB eq. (5.31) and eq. (5.36b) for $T = 1$, $1/10$ and $1/100$, respectively. As expected, damage accumulates during the off-period and otherwise relaxes at all times, resulting in a characteristic saw-tooth profile. Fig. 5.3d shows the corresponding evolution of the damage state variable predicted by the effective fractional-step eq. (5.43). Evidently, the high-cycle limiting curve is smooth and represents a weak limit of the damage evolution curves as the number of duty cycles tends to infinity, respectively, the pulse duration cycle tends to zero.

Cell death

We recall that the state variable $q(t)$ measures the amount of damage sustained by a cell at time t. A plausible assumption is that a cell becomes unviable and dies when $q(t)$ attains a critical value q_c. In light of our previous discussion, this condition cannot be met if $q_{\max} \le q_c$, i.e., if the maximum accumulated damage induced by insonation is less that the critical value. Conversely, it follows from (5.46) that cell death requires a minimum level of energy deposition

$$\varepsilon \ge \varepsilon(q_c,\lambda). \tag{5.47}$$

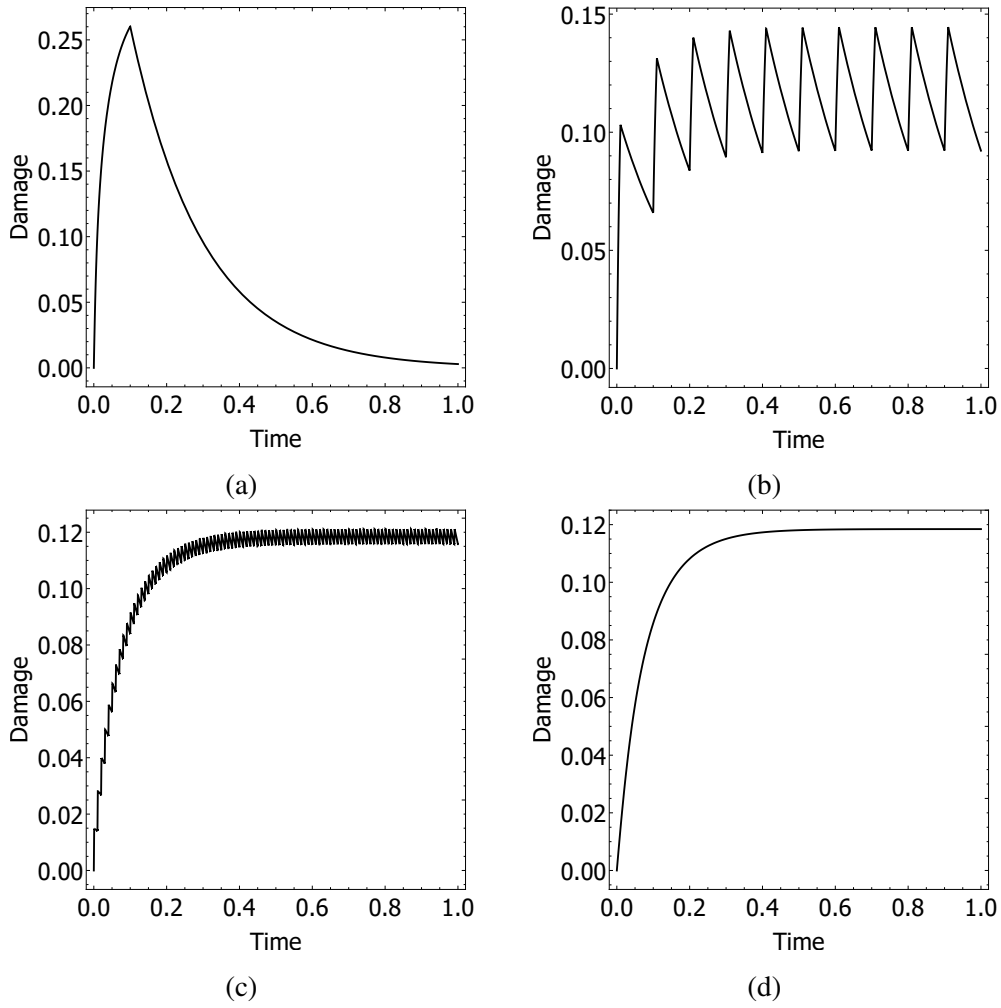

Figure 5.3: Convergence of the damage evolution to the high-cycle limit as pulse repetition period T becomes much smaller than the characteristic time t_r for healing, cf. Fig. 2.3a (inset). Parameters: $t_r = 10$, $\lambda = 1/10$, $\omega = \omega_0 = 100$, $\zeta = 1/10$, $q_{\max} = 1/2$. a) $T = 1$. b) $T = 1/10$. c) $T = 1/100$. d) Damage evolution predicted by the high-cycle limit equation (5.43).

If this condition is met, then in the high-cycle limit the time-to-death of a cell follows from (5.44) as

$$\tau_c = \int_0^{q_c} \frac{d\xi}{\dfrac{\lambda(1-\xi)w^4\varepsilon}{\left(w^2-(1-\xi)^2\right)^2+4\zeta^2w^2} - \xi}, \tag{5.48}$$

otherwise $\tau_c = +\infty$ and the cell survives for all time. The corresponding number of insonation pulses is

$$N_c = \frac{\alpha}{\beta}\frac{\tau_c}{T}, \tag{5.49}$$

where T is the total pulse duration.

As noted in the introduction, this type of system failure by slow damage accumulation over many cycles is observed in other systems, notably inert structural materials, in which context it is known as *high-cycle mechanical fatigue*. The number of loading cycles to failure is correspondingly known as the *fatigue life* of the material. In this analogy, cell death by slow damage accumulation over many cycles may be thought of as a form of *mechanical cell fatigue*, and the number of cycles N_c to death as the *fatigue life* of the cell.

Variability within a cell population

A typical population of cancerous cells exhibits broad variation in geometry and mechanical properties. This variability is strongly suggested by the cell-death curves observed by Mittelstein *et al.* [54], which show that some cells die much earlier than others. In order to capture this gradual cell necrosis, we regard the parameters governing the evolution of the cells as random and a cell population as a sample drawn from the probability distribution of the parameters. By virtue of the variability of the sample, parts of the population have a relatively short time-to-death and die early, whereas other parts have a comparatively longer time-to-death and die later, resulting in the gradual estimated cell death curves observed experimentally, Fig. 2.6.

The statistics of the time-to-death can be estimated simply by means of a linear sensitivity analysis (cf., e. g., [73]). We see from (5.62) that the time-to-death $t_c = \tau_c t_r$ depends on the cell parameters $(t_r, \omega_0, \zeta, q_c)$, respectively, the relaxation time for healing, the natural frequency of vibration, and the damping ratio; and on the process parameters $(\varepsilon, \omega, \lambda)$, respectively, the energy intensity, frequency, and on-period fraction of the insonation. For simplicity, we assume that the process parameters can be controlled exactly and are uncertainty-free. Contrariwise, the cell parameters define a random variable $X \equiv (t_r, \omega_0, \zeta, q_c)$, with probability distribution reflecting the variability of the cell population.

Owing to the randomness of the cell population, the time-to-death t_c itself defines a random variable Y. In terms of these random variables, (5.62) defines a relation of the form

$$Y = f(X). \tag{5.50}$$

In order to estimate the variability in the time-to-death random variable Y, we make a small-deviation approximation

$$Y \approx f(\bar{X}) + Df(\bar{X})(X - \bar{X}) + h.o.t., \tag{5.51}$$

where

$$\bar{X} = \mathbb{E}(X) \equiv (\bar{t}_r, \bar{\omega}_0, \bar{\zeta}, \bar{q}_c) \tag{5.52}$$

is the mean value of the cell parameters and $Df(\bar{X})$ are sensitivity parameters. The average time-to-death then follows as

$$\bar{Y} = \mathbb{E}(Y) \approx f(\bar{X}) + h.o.t. \tag{5.53}$$

In addition, a measure of the variability of Y is given by the variance

$$\sigma^2 = \mathbb{E}((Y - \bar{Y})^2) = Df(\bar{X})^T \mathbb{E}((X - \bar{X}) \otimes (X - \bar{X}))Df(\bar{X}) = Df(\bar{X})^T \Sigma Df(\bar{X}), \tag{5.54}$$

where

$$\Sigma = \mathbb{E}((X - \bar{X}) \otimes (X - \bar{X})) \tag{5.55}$$

is the covariance matrix of the cell parameters.

We note that, for small deviations, the mean time-to-death of the cell population is obtained by evaluating (5.62) at the mean value $\bar{X} = (\bar{t}_r, \bar{\omega}_0, \bar{\zeta}, \bar{q}_c)$ of the cell parameters, cf. eq. (5.53), with the result

$$\bar{t}_c = \bar{t}_r \int_0^{\bar{q}_c} \frac{d\xi}{\dfrac{\lambda(1-\xi)\bar{w}^4\varepsilon}{\left(\bar{w}^2 - (1-\xi)^2\right)^2 + 4\bar{\zeta}^2\bar{w}^2} - \xi}, \tag{5.56}$$

where we write $\bar{w} = \omega/\bar{\omega}_0$ and we assume that (5.47) is satisfied with $q_c = \bar{q}_c$. Likewise, the requisite sensitivity parameters $Df(\bar{X})$ follow by differentiating (5.53) with respect to the cell parameters and evaluating the resulting integrals at their mean value.

Simple forms of the probability distribution of t_c are fully determined by the statistics $\bar{Y}$ and σ^2. For instance, if we hypothesize a gamma distribution

$$p(Y) = \frac{1}{\Gamma(k)\theta^k} Y^{k-1} \mathrm{e}^{-Y/\theta}, \tag{5.57}$$

then the parameters of the distribution follow as

$$\bar{Y} = k\theta, \qquad \sigma^2 = k\theta^2. \tag{5.58}$$

The fraction of the cell population with a time-to-death less or equal to t is given by the cumulative distribution function

$$F(t) = P(Y \leq t). \tag{5.59}$$

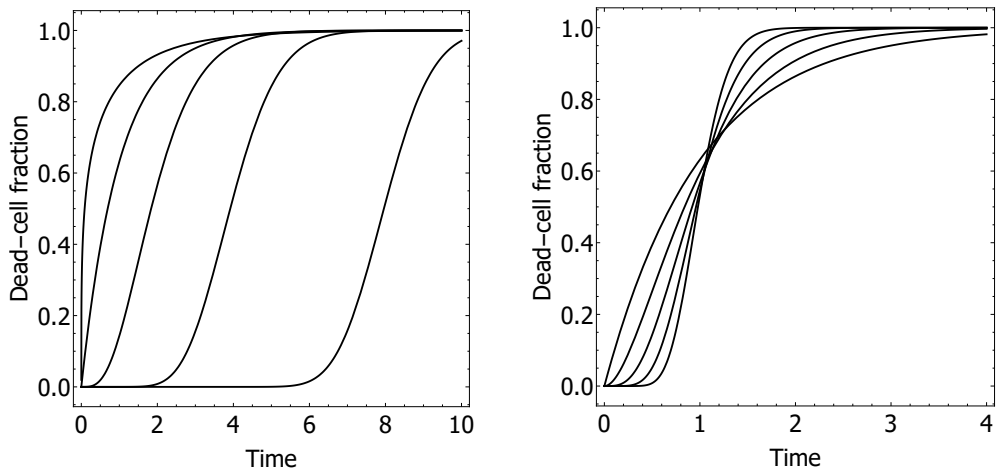

(a) (b)

Figure 5.4: Dead-cell fraction *vs*. time curves obtained from the Gamma-distribution. a) $\sigma^2 = 1$, $\bar{t}_c = 1/2$, 1, 2, 4 and 8. b) $\bar{t}_c = 1$, $\sigma^2 = 1$, 1/2, 1/4, 1/8 and 1/16.

For the gamma distribution (5.57), we have

$$F(t) = 1 - \frac{\Gamma(k, t/\theta)}{\Gamma(k)}, \tag{5.60}$$

where Γ is the gamma function. The resulting dead-cell fraction *vs*. time curves are illustrated in Fig. 5.4.

5.2 Qualitative comparison with experiments

We proceed to assess the ability of the proposed dynamical model to account for the experimentally observed trends summarized in Section 2. Evidently, the experimentally observed dead-cell fraction vs. time curves exhibit the sigmoidal form predicted by the proposed dynamical model, cf. Figs. 2.6 and 5.4, which can be used to fit the experimental curves. More importantly, the model *explains* the observed dead-cell fraction curves as a result of cell-to-cell variability, specifically, the random distribution of times-to-death in the cell population. Furthermore, the time-to-death of an individual cell is predicted by the model explicitly as a function of cell parameters $(t_r, \omega_0, \zeta, q_c)$ and process parameters $(\varepsilon, \omega, \lambda)$, e. g., through eq. (5.62) in the high-cycle limit. Owing to the variability of the cell population, the cell parameters may be assumed to be random and, by an appeal to linear sensitivity analysis, the mean and variance of the cell time-to-death can be related to the mean values and covariance matrix of the cell parameters, eqs. (5.62) and (5.54). Thus, if the statistics of the cell parameters are known, the time-to-death

statistics and, correspondingly, the dead-cell fraction curves, are given explicitly by the model. In this manner, the model relates the observed dead-cell fraction curves to fundamental mechanical properties of the cell such as mass, stiffness, viscosity and damage tolerance.

The dynamical model also predicts the dependence of the dead-cell fraction curves on pulse duration observed experimentally, Fig. 2.5. Indeed, this trend is exhibited by the damage evolution curves shown in Fig. 5.3. A careful inspection of these curves shows that the maximum level of damage attained within the insonation cycles decreases as the pulse duration decreases relative to the characteristic time for healing. Thus, for long pulses the cells have time to accumulate large amounts of damage during the on-period of the pulse. For shorter pulses, the extent of damage accumulation is comparatively less. If the pulse duration is comparable to—or smaller than—the relaxation time for healing, the cell does not have sufficient time to recover during the off-period of the cycle, and the trend persists over repeated cycles. Therefore, according to the model the dependence of the dead-cell fraction curves on pulse duration is the result of a delicate interplay between the pulse repetition period and pulse duration, the cell dynamics, which determines the rate at which damage accumulates and the kinetics of cell healing, which determines the rate at which damage is restored.

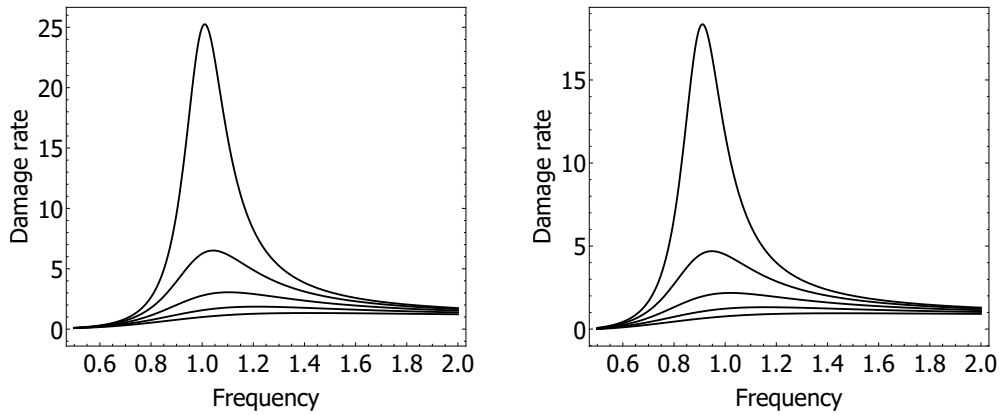

Figure 5.5: Damage accumulation rate as a function of insonation frequency. Parameters: $\omega_0 = 1$, $\varepsilon = 1$, $\lambda = 1$, $t_r = 1$, $\zeta = 1/10, 2/10, 3/10, 4/10, 5/10$. a) Pristine cell, $q = 0$. b) Damaged cell, $q = 1/10$.

The dynamical model also exhibits the oncotripsy effect, i.e., the insonation-frequency dependence of the cell response and the window of opportunity for selective cell killing. Fig. 5.5 shows the damage accumulation rate $\dot{q}$ computed

from (5.43) as a function of insonation frequency, damping ratio, and state of damage. The parameters used in the figure are: $\omega_0 = 1$, $\varepsilon = 1$, $\lambda = 1$, $t_r = 1$, $\zeta = 1/10$, $2/10$, $3/10$, $4/10$, $5/10$, $q = 0$, $1/10$. As may be seen from the figure, the damage rate peaks sharply in the vicinity of the undamped resonant frequency $\omega = \omega_0$. The damage accumulation rate is largest for a pristine cell, $q = 0$, and persists, albeit somewhat reduced, after the cell sustains damage, $q = 1/10$. This frequency dependence is clearly apparent in the experimental data (see Fig. 2.5).

5.3 Quantitative comparison with experiments

In this section, we proceed to simulate cell-death histories by means of the reduced model theory explained throughout this chapter. In this context, we are not interested in the average cell-death time, but rather on its variance due to the variability of the cell parameters.

In particular, we aim to reproduce the cell-death lifetime data of a leukemia cell K-562. Figure 5.6 shows the fit of the Gamma distribution $Y \sim \Gamma(k, \theta)$ to lifetime data obtained in experiments [54] (not published) for the cell line type K-562 at free field peak negative pressure 0.7 MPa, pulse duration of 100 ms and 10% duty cycle. The mean and deviation standard are provided in Table 5.1.

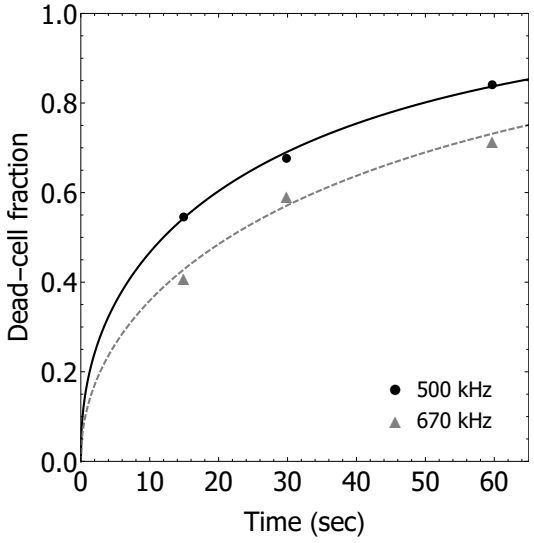

Figure 5.6: Γ-distribution fit of cell-death time data [54] for cell line K-562 at focal pressure 1.4 MPa, pulse duration 100ms, 10% duty cycle at two insonation frequencies 500 kHz and 670 kHz. The mean and deviation standard is tabulated in 5.1

Table 5.1: Mean and deviation standard for cell-death lifetime data for K-562 at PNP=0.7MPa, 100ms pulse duration, 10% duty cycle and frequencies (1) 500kHz and (2) 670kHz

$\bar{Y}_1$	σ_1	$\bar{Y}_2$	σ_2
30.5 sec	46.6 sec	49.4 sec	71.36 sec

Simulation of cell-death time

We model heterogeneous cell responses by simulating the behavior of a population of cells. First, we run sets of many simulations representative of cell-to-cell variability on cell parameters. Let $X_1, ..., X_N$ be the random sampling drawn from the probability distribution of the physiological parameters of the cell given by $\mathcal{F}$, such that

$$X = \{X_1, X_2, ...X_i, ..., X_N\} \quad \text{with} \quad X_i = \{t_{r_i}, \omega_{0_i}, \xi_i, q_{c_i}\}. \tag{5.61}$$

The cell-death time is computed by means of the reduced model with

$$t_c = t_r \int_0^{q_c} \frac{d\xi}{\dfrac{\lambda(1-\xi)w^4\varepsilon}{\left(w^2-(1-\xi)^2\right)^2+4\zeta^2w^2} - \xi}, \tag{5.62}$$

which leads to a vector of cell-death times,

$$t_c = \{t_{c_1}, t_{c_2}, ..., t_{c_i}, ..., t_{c_N}\}. \tag{5.63}$$

Then, the simulated (or empirical) distribution function (SDF), $\hat{Y}$, is a cumulative distribution function,

$$\hat{Y}(T|X) = \frac{\#\text{elements in sample} \leq T}{N} = \frac{1}{N}\sum_{i=1}^{N} I(t_i < T), \tag{5.64}$$

where $I(\cdot)$ is the indicator function. The SFD first and second moments can then be compared to the experimental CDF.

Ideally, the distribution for each parameter would come from independent tests at the conditions of the experiments. However, as this information is not available, we will assign independent log-normal distributions with mean and variance based on the following information gathered from the biological literature:

1. The highest cell fraction death of the cell K-562 occurs at 500kHz as observed in Fig. 2.6.b;

2. For Human Airway Smooth Muscle (HASM) cells affected by LIPUS, the net contractile moment drops to 50% of its initial value and recuperates almost completely in 200sec when insonated at moderate acoustic pressures [55].

3. Cells are highly viscous structures. For example, the apparent viscosity for fibroblast and endothelial cells is $\sim 10^4$ Pa.s. [58]. However, the apparent viscosity has been shown to decrease in cancerous cells, and it has been associated with the disorganized arrangement of the F-actin filaments [79].

4. Probability densities of cells stiffness and viscosity are skewed and usually show large deviations from the mean [58].

These hypotheses lead to search for the mean value of the parameters in the neighborhood of $\bar{t_r}$ = 200 sec, $\bar{\omega_0}$ = 500 kHz and $\bar{\xi}$ = 0.8. In addition, as both damage parameters, α and β are unknown, we assume ε to be larger than the capability of the cytoskeleton to repair itself (i.e., β small) and we set ($\omega^2\varepsilon$)=10.

We search for the mean value of the parameters X by solving a least squares (LSQ) optimization problem. This is, we search for the parameter values that minimize the squared differences between the model and the observations,

$$\bar{X^*} = \arg\min_{\bar{X}} \quad \frac{1}{2}\left\|\bar{Y_1} - \hat{Y_1}(\bar{X})\right\|_2^2 + \frac{1}{2}\left\|\bar{Y_2} - \hat{Y_2}(\bar{X})\right\|_2^2 \tag{5.65}$$

with $\hat{Y_1}(\bar{X})$ and $\hat{Y_2}(\bar{X})$ the estimated values of the experimental mean at 500 and 670 kHz, respectively. Finally, we find $\bar{X^*} \equiv$ (100sec, 2π 500kHz, 0.70, 0.136) with $\hat{Y_1}$ = 30.5 sec and $\hat{Y_2}$ = 40.3 sec (see Table 5.3). The resulting mean damage curves $\bar{q}(t)$ can be seen in Fig. 5.7, as well as the change of natural frequency with respect to time. As expected, the damage increases along time and impacts on the natural frequency as it deviates from the excitation. In particular, the mean critical damage refers to a 26% change of the initial stiffness and a 14% decrease of the natural frequency upon cell-death.

To asses the influence of the recuperation time, natural frequency, damping and critical damage over the mean value of cell-death time, we compute the dimensionless sensitivity coefficients (see Table 5.4) as

$$S_p = Df(\bar{X}_p)\frac{\bar{X}_p}{f(\bar{X})} \tag{5.66}$$

with $\bar{X}_p$ the parameter of interest in the vector $(\bar{t}_r, \bar{\omega}_0, \bar{\zeta}, \bar{q}_c)$ while the other parameters are held constant. The coefficients show the fraction of change in the mean cell-death by the fraction of change of a cell parameter. Under the process parameters of the study, the sensitivity analysis shows that cell-death time is the most sensitive to the critical damping of the cell, followed by the critical damage and natural frequency. Contrary, small deviations from the recuperation time do not have a major effect on the mean time-to-death.

Next, we are interested in assesing the variability of the cell-death fraction, and not only in its mean value. We carefully select a deviation standard for each parameter based on the literature and constraint the maximum deviation of the parameters to be $\sigma^2_{\omega_0} < 0.25\ \omega_0$, $\sigma^2_{\xi} < 0.25\ \xi$, $\sigma^2_{t_r} < 0.1\ t_r$ and $\sigma^2_{q_c} < 0.1\ q_c$. The standard deviation for the cell parameters is optimized such that,

$$X^*_\sigma = \arg\min_{X_\sigma} \quad \frac{1}{2}\left\| Y_1(t) - \hat{Y}_1(\bar{X}, t)\right\| + \frac{1}{2}\left\| Y_2(t) - \hat{Y}_2(\bar{X}, t)\right\|. \tag{5.67}$$

The parameters t_r, ω_0, ξ and q_c follow a log-normal distribution (see Fig. 5.2) with mean and variance listed in Table 5.2. It is worth noticing that the fit parameters are not unique, and further data collection should be gathered to reduce the uncertainty and validate these probability densities.

Finally, we are in a position to compare predicted cell-death curves with the experimental data. Fig. 5.8 shows computed cell-death curves for log-normal independent cell population parameters, with mean values and standard deviations as in Table 5.2, together with experimental data from [54]. The predicted curves are computed directly via Monte Carlo based on a sample of size $N = 1000$ and by means of the linearized-sensitivity approximation. As may be seen from the figure, the linearized-sensitivity curve closely approximates the Monte Carlo curve, which establishes the validity of the linearized-sensitivity approximation under the conditions of the experiments. In addition, both the linearized-sensitivity and the Monte Carlo curves match closely the experimental data, which provides a measure of validation of the model.

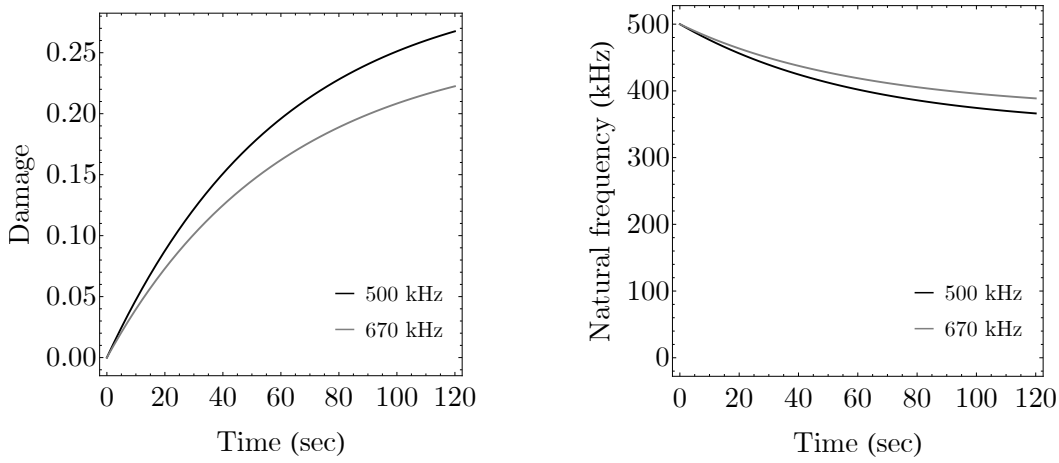

Figure 5.7: Cytoskeleton damage along exposure time with parameters $\bar{X} \equiv (105\text{sec}, 2\pi\ 500\text{kHz}, 0.5, 0.285)$ with $\bar{Y} = 40.5$ sec for the process parameters $(\varepsilon, \omega, \lambda) = (10, 2\pi\ 500\text{kHz}, 0.1)$.

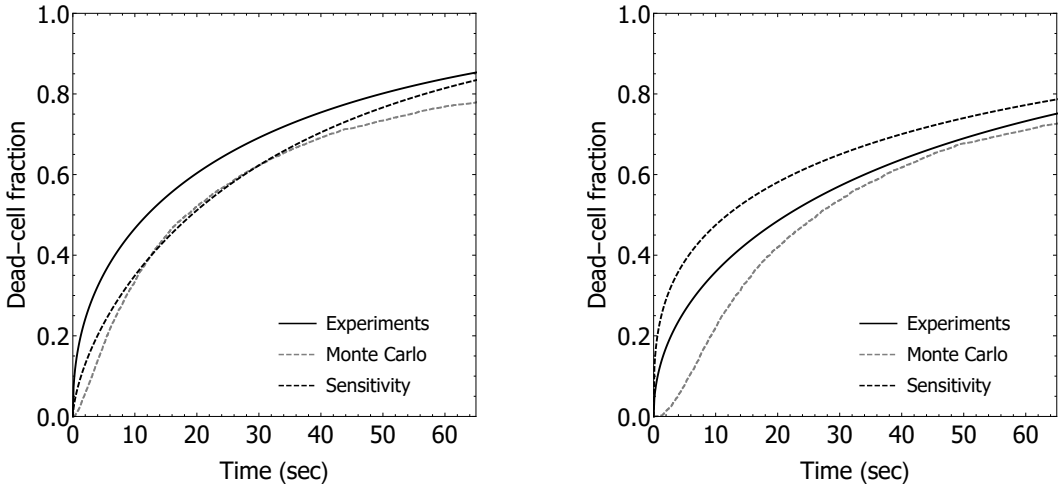

Figure 5.8: Comparison of predicted cell-death fraction with experimental data from [54] for a focal pressure of 1.4MPa, pulse duration 100ms, duty cycle 10% and frequencies 500kHz and 670kHz. The experimental data is represented through the Γ-distribution fit shown in Fig. 5.6.

Table 5.2: Mean and variance for the simulation parameters t_r, ω_0, ξ and q_c.

	t_r	ω_0	ζ	q_c
Mean	100 sec	1000π kHz	0.7	0.136
Variance	10 sec^2	125 π kHz^2	0.175	0.0136

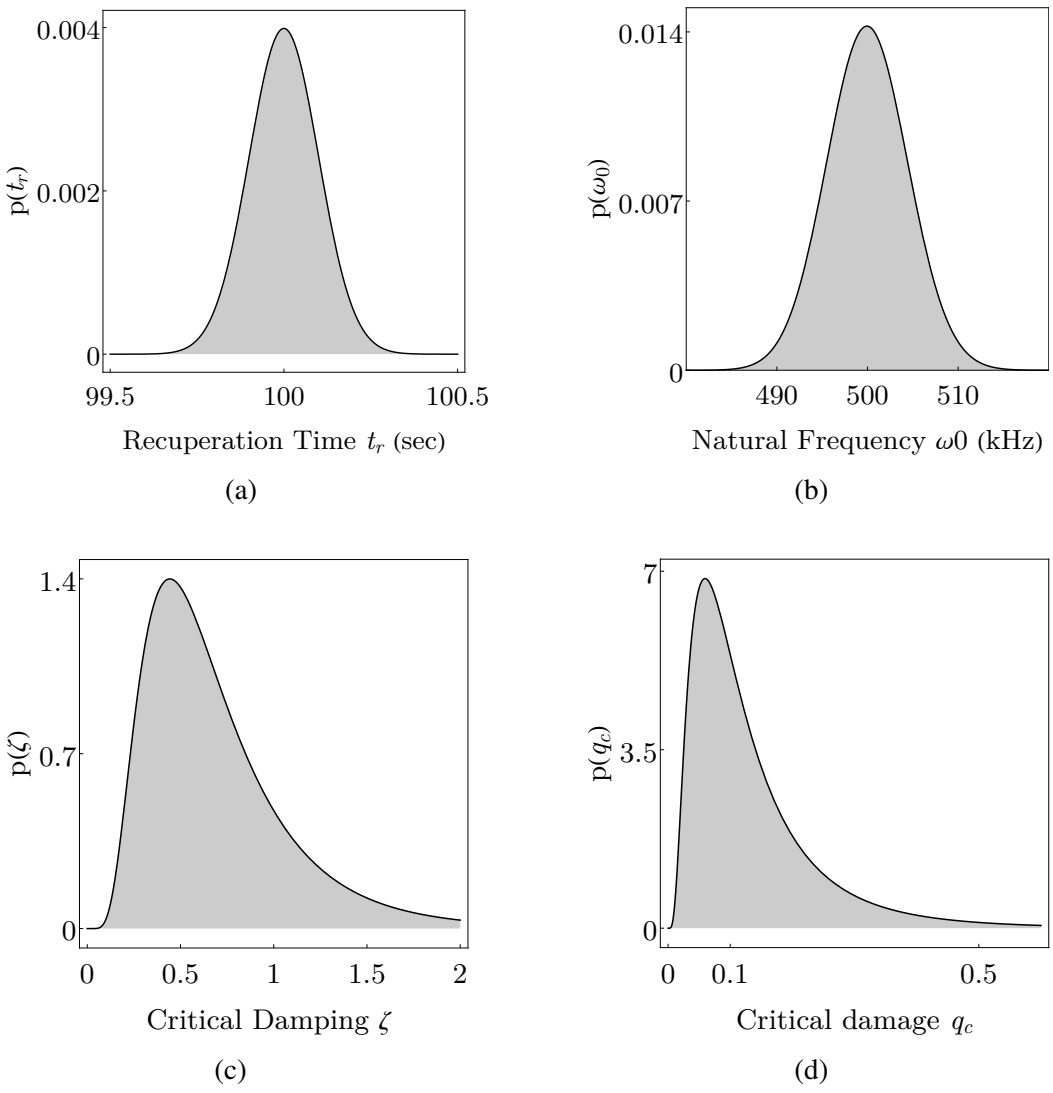

Figure 5.9: The parameters t_r, ω_0, ξ and q_c are assumed to be random variables log-normally distributed with mean and variance in Table 5.2 . (A) Recuperation time in seconds, (B) natural frequency in KHz, (c) critical damping and (D) critical damage.

Table 5.3: Simulated mean parameters with $\hat{Y}_1 = f(\bar{X})$ and $\hat{Y}_2 = f(\bar{X})$ the estimated mean value of the experiments at 500 and 670 kHz, respectively.

$\bar{t}_r$	$\bar{\omega}_0$	$\bar{\zeta}$	$\bar{q}_c$	$\hat{Y}_1$	$\hat{Y}_2$
100 sec	1000π kHz	0.7	0.136	34.6 sec	45.3 sec

Table 5.4: Normalized sensitivity parameters Df

$Df_{\bar{t}_r}$	$Df_{\bar{\omega}_0}$	$Df_{\bar{\zeta}}$	$Df_{\bar{q}_c}$
1.0	1.48	2.34	1.71

5.4 Comparison to the finite element model

This section addresses the domain of validity of the reduction hypotheses against simulations of the finite element model. We simulate the cell under a variety of frequencies, and we compare the damage state variable between the finite element model (FEM) and reduced model (RM). The comparison is made under the same conditions of mass, stiffness, damping and kinetic parameters using the conversion equations 5.16 and 5.21. These are shown in Table 5.5. For an explanation on how to setup the finite element model, please refer to Chapter 4.

Table 5.5: Geometry, mass and effective mechanical properties used in the comparison of the reduced model to the finite element model.

Characersitic		**Value**	**Unit**
a	nucleus radius	0.0045	mm
b	cell radius	0.009	mm
m	effective cell mass	1.18e-9	gr
k	effective cell stiffness	0.012	MPa
c	effective cell viscosity	5.86e-7	MPa ms
α^*	kinetic damage parameter 1	1.0	MPa ms
β^*	kinetic damage parameter 2	0.5	MPa
μ_c	shear modulus of the cytoskeleton	0.033	MPa
μ_n	shear modulus of the nucleus	0.3	MPa
η	shear viscosity of the cell	1e-5	MPa ms
ρ_c	density of the cytoskeleton	0.001	gr/mm^3
ρ_n	density of the nucleus	0.0015	gr/mm^3
P	pressure	1.4	MPa
λ	duty cycle	0.1	

For dynamic models, the corresponding of the eigenfrequencies is crucial. For the case of a leukemia cell, we compute the relative error of the finite element eigenfrequencies ω^*, obtained in EurekaLite,

$$e = \frac{|\omega - \omega^*|}{\omega^*}. \tag{5.68}$$

Likewise, the finite element solutions $q^*(t)$ and $u_y^*(t)$, obtained in EurekaLite, were considered as reference values for computing the relative errors for damage and displacements of the reduced model.

We compute the error of the finite element model displacements $u_y^*(t)$ against the reduced model displacements $u_y(t)$ on the time (0,T),

$$error = \sqrt{\int_0^T (u_y(t) - u_y^*(t))^2 \frac{dt}{t^2}}. \tag{5.69}$$

We nondimensionalize this error with respect to the finite element excitation frequency ω^*, the applied displacements U and the time T, so that

$$\frac{error}{factor} = \frac{1}{\omega^* \sqrt{T} U} \sqrt{\int_0^T (u_y(t) - u_y^*(t))^2 \frac{dt}{t^2}}. \tag{5.70}$$

Notice that the applied displacements depend on the excitation frequency through $U = \frac{V}{\omega *}$, where V is the particle velocity.

$$\frac{error}{factor} = \frac{1}{\sqrt{T} V} \sqrt{\int_0^T (u_y(t) - u_y^*(t))^2 \frac{dt}{t^2}}. \tag{5.71}$$

Similarly, we compute the error of the finite element model damage $q^*(t)$ against the reduced model displacements $q(t)$ on the time (0,T),

$$error = \sqrt{\int_0^T (q(t) - q^*(t))^2 \frac{dt}{t}}. \tag{5.72}$$

We nondimensionalize this error with respect to the finite element the time T and the relaxation time t_r, so that

$$\frac{error}{factor} = \frac{t_r}{\sqrt{T}} \sqrt{\int_0^T (q(t) - q^*(t))^2 \frac{dt}{t}} \tag{5.73}$$

with t_r the recuperation time. The damage corresponds to maximum at the end of the time. The damage in the finite element model corresponds to the damage of the fiber on the direction of the nucleus translation.

The computed relative error for the resonance frequencies, displacements and damage are shown in Table 5.6 through 5.8. For the cancerous cell, the resulting frequency of resonance is located at 450kHz (FEM) and 500kHz (RM), which results in an 11% error. The healthy cell has its eigenfrequency at 675kHz (FEM) and 705 (RM), which leads to an error of 4%. As regards the nuclear displacements and average cytoskeletal damage predicted by the reduced model, the errors are found

to be within 7% of the full-field finite-element calculations. The frequency in the RM seems to be concentrated around resonance, whereas the FEM spreads out over the frequency domain. This is not observed in the FEM at a lower pressure and no viscosity (see Fig. 5.10), indicative of the higher viscous dissipation in the FEM.

Table 5.6: Frequency shift between the finite element model and the reduced model. The displacement and damage were obtained from a frequency response analysis up to 0.1ms. There is a shift in frequency between the maximum of the displacement and the damage. The maximum damage occurs at the undamped frequency.

	Displacement		Damage	
	Cancerous	Healthy	Cancerous	Healthy
Finite Element Model	455	675	490	700
Reduced Model	499	705	499	705
Error	0.096	0.044	0.017	0.007

Table 5.7: Error in the displacement between the finite element model and the reduced model, with T=0.1ms, V=1mm/ms and t_r=2ms. This comparison is performed at each model respective frequency of resonance.

	Displacement	
	Cancerous	Healthy
Error	0.021	0.019
Error/Factor	0.066	0.0599

Table 5.8: Error in the damage between the finite element model and the reduced model, with T=0.1ms, V=1mm/ms and t_r=2ms. This comparison is performed at each model respective frequency of resonance.

	Damage	
	Cancerous	Healthy
Error	0.00043	0.00087
Error/Factor	0.0027	0.0054

Further on, the damage evolution for the finite and reduced element models can be found in Fig. 5.11. It can be noticed that the damage in the direction of the wave propagation Y has a higher fidelity than with the mean damage. Fig. 5.12 shows the comparison of the models for the frequency response of the maximum damage in a pulse of 0.1ms. Evidently, the maximum damage between models is different pointwise.

Overall, the results presented in this section shows that the reduced model follows the trends of the finite element model. The nuclear displacements and average

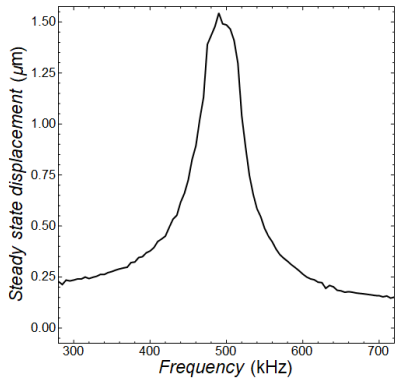

Figure 5.10: Displacement of the nucleus at T=0.1ms for P=0.2MPa and no viscous effects.

cytoskeletal damage predicted by the finite element model is smaller than that for the reduced model. The difference is mostly associated to (a) large displacements during resonance, (b) gap betwen the resonant frequencies and (c) non-homogeneous damage on the finite element model in contrast to homogeneously distributed in the reduced model. Given the level of observational error, this accuracy may reasonably be deemed adequate for all practical purposes.

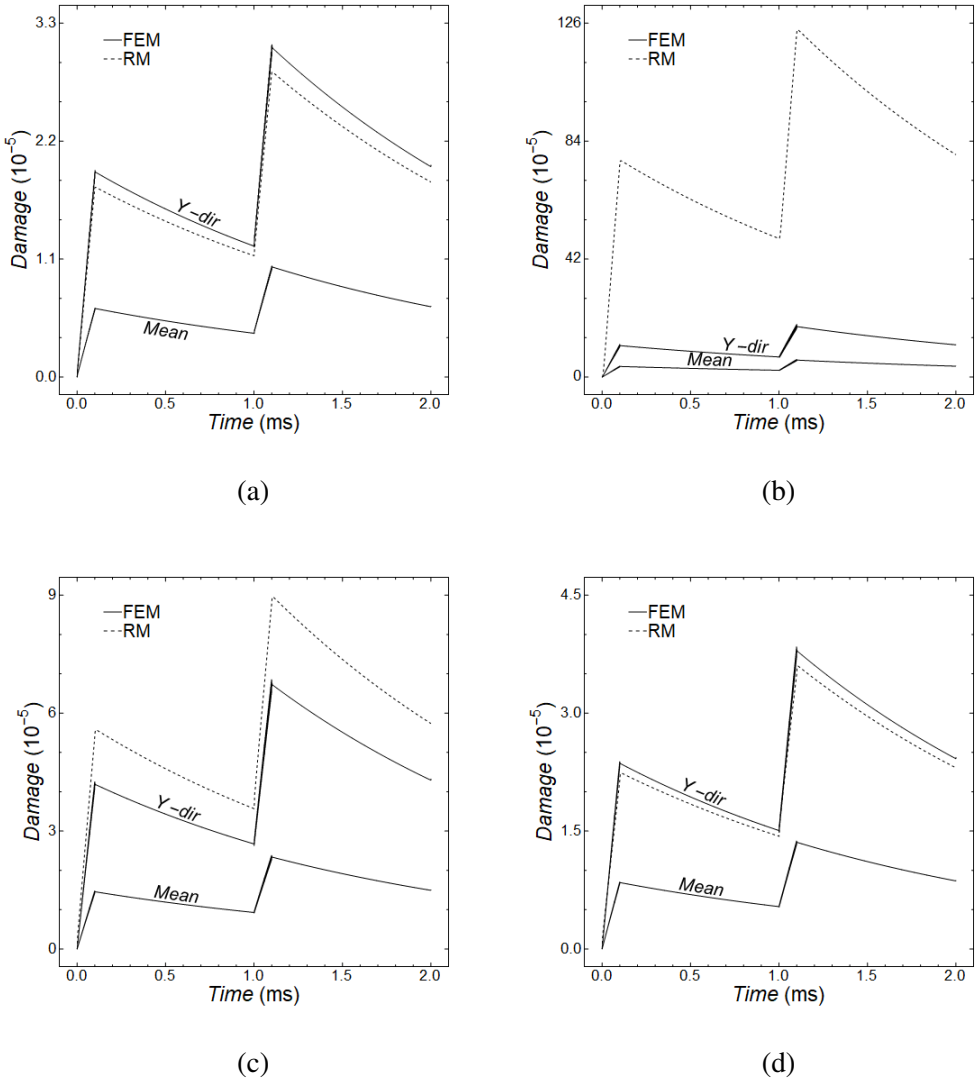

Figure 5.11: Mean damage for a cancerous and healthy cell between t = 0 ms and 2 ms, with pulse duration 0.1ms and pressure 1.4MPa. The response shows resonant in the neighborhood of 500 kHz for the cancerous cell and 700 kHz for the healthy cell. (a) f = 300 kHz. (b) f = 500 kHz. (c) f = 670 kHz. (d) f = 800 kHz.

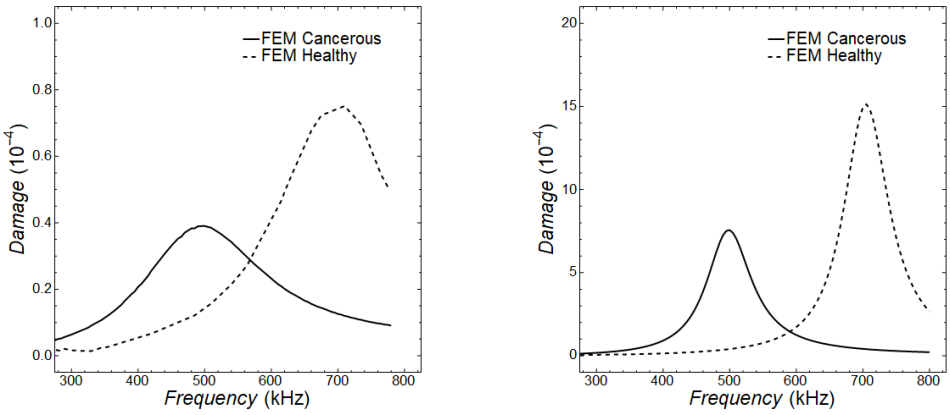

(a) (b)

Figure 5.12: Displacement of the nucleus at T=0.1ms for P=1.4MPa. (a) FEM. (b) RM.

5.5 Discussion and concluding remarks

The proposed dynamical model provides a rational basis for understanding the oncotripsy effect posited by Heyden and Ortiz [29] under the conditions of the experiments of Mittelstein *et al*. [54]. An important difference between those experiments and the scenario initially contemplated in [29] is that in the experiments of Mittelstein *et al*. [54] the cells are in aqueous suspension, whereas the analysis of Heyden and Ortiz [29] is concerned with cells embedded in a solid extracellular matrix (ECM). In aqueous suspension, the cells experience an exceedingly viscous environment, which is likely to suppress any vibrations of the cell membrane. The response of the cells to ultrasound stimulation is thus reduced to that of an internal resonator. Heyden and Ortiz [29] pointed out that the spectral gap between cancerous and healthy cells depends sensitively on the mechanical properties of the ECM and that the changes in those properties experienced by the cancerous tissue are a key contributing factor to the opening of a spectral gap. In addition, for cells embedded in an ECM, membrane rupture provides an additional lysis mechanism which is absent in cells in suspension. These considerations suggest the need for an independent experimental assessment of the oncotripsy effect in cancerous tissues, preferrably *in vivo*.

The proposed dynamical model also reveals the dependence of oncotripsy on fundamental cell parameters and on process parameters. The cell parameters of the model can be calibrated from cell-death data for specific cell lines. Alternatively, fundamental cell properties such as stiffness and viscosity can be measured independently. The calibrated model can then be used as a tool for optimizing process parameters for maximum therapeutic effect. Most importantly, theoretical understanding such as provided by the proposed dynamical model is key for interpreting experimental observations and formulating new and improved clinical therapies.

Chapter 6

METHOD OF ONCOTRIPSY

6.1 Introduction

In this chapter, we develop a theoretical framework to evaluate the effect of Oncotripsy employing the reduced model presented in Chapter 5.

The first section is dedicated to reviewing the reduced dynamical model of Oncotripsy. The reduced model of oncotripsy is a mathematical tool that facilitates parameter studies, including sensitivity analysis and process optimization of the oncotripsy effect. The model predicts the response of a cell population to Low-Intensity Pulsed Ultrasound (LIPUS) as a function of fundamental cell properties and process parameters. Dead-cell fraction curves can be obtained as a result of cell-to-cell variability.

The second section is dedicated to numerical experiments for different process parameters. We discuss damage, mean time-to-death, and a cell-dead fraction under a wide variety of pressures, frequencies of excitation, and duty cycle. The study offers valuable insight into understanding the complex interaction of these parameters influence on cell death.

Next, we propose a framework to determine the optimal process parameter that maximizes the oncotripsy effect. Based on the idea of Ashby charts for the design and selection of materials, we create charts for oncotripsy with the aim of selection of process parameters for in-vitro and, potentially, tissue applications.

Finally, this section provides a comprehensive Ashby-type process parameter selection charts to maximize the oncotripsy effect. Due to the variability of mechanical and kinetic properties, it is excepted that some overlap of natural frequencies exists between healthy and cancerous cells. For a given set of free parameters — i.e., pressure, duty cycle and exposure time — a performance index can be plotted into the chart to show the efficiency of each frequency for a given cell population.

6.2 Theory

In this section, we present a summary of the theoretical basis of the oncotripsy effect. While Subsection 6.2 is concerned with the derivation of the damage state and time-to-death of a single cell, details on the resulting cell-dead fraction of a

population of cells is given in Subsection 6.2. Further details may be consulted in Chapter 5.

Damage and time-to-death of a single cell

In our previous work, we developed a reduced model of oncotripsy as an application of cell dynamics, statistical mechanical theory of network elasticity and 'birth-death' kinetics to describe processes of damage and repair of the cytoskeleton. The failure mechanism of oncotripsy is the damage accumulation over many (million) of insonation cycles under which a progressive disruption of the actin fibers occurs.

The reduced dynamical model of cell deformation and damage was based on the following assumptions:

i) Spherical geometry of cell and nucleus.

ii) Rigid translational motion of the cell membrane.

iii) Heavy and rigid nucleus.

iv) *Ansätze* for the cytoplasm deformation and damage fields.

Based on the *network theory of elasticity* in statistical mechanics, an energy density per unit volume for the cytoskeleton was proposed. We introduced a damage variable $q(\xi)$ whereby accounts for the attendant loss of stiffness of the cytoskeleton. This variable ranges from 0 to 1 such that $q(\xi)$=0 when all fibers in direction (ξ) are intact and $q(\xi)$=1 when all fibers in direction (ξ) are broken. Further, we assume a linear viscosity uniformly distributed over the cytoplasm.

Assuming the damage is isotropic, i.e., q is independent of direction ξ, and that the cell translates rigidly through a time-dependent displacement u(t) relative to the cell membrane, one can compute the total free energy, dissipation, and kinetic energy of the system. Finally, an appeal to the Lagrange-D'Alambert principle gives the following system of coupled equations:

$$m\ddot{u}(t) + c\dot{u}(t) + (1 - q(t))^2 ku(t) = -m\dot{v}(t), \tag{6.1a}$$

$$\alpha_v \dot{q}(t) + \beta_v q(t) = (1 - q(t))u^2(t), \tag{6.1b}$$

with m, c, k, α_v and β_v the total mass, damping coefficient, stiffness, and kinetic parameters of the cell given by,

$$m = m_0 + \frac{2\pi}{15}\rho(b-a)(6a^2+3ab+b^2),\ c = \frac{4\pi}{27}\frac{b^3-a^3}{(b-a)^2}(4\eta+3\kappa),\quad k = \frac{32\pi}{9}\frac{b^3-a^3}{(b-a)^2}\mu, \tag{6.2}$$

with a as the nucleus radius, b the cell radius, m_0 the nucleus mass, η the shear viscosity, κ the bulk viscosity, and μ the shear modulus. In particular, eq. (6.1a) represents a damped and forced harmonic oscillator, with the material velocity $v(t)$ of the aqueous medium supplying the forcing which the stiffness depends on the instantaneous state of damage. The second eq. (6.1b) governs the kinetic evolution of damage state, including damage accumulation and healing.

We note that under the conditions of interest here, the dynamics described by the system (6.1) is characterized by two disparate time scales: the period of oscillation and the characteristic time for damage evolution, the former much smaller than the latter. This two-time structure suggests analyzing the problem by means of WKB asymptotics [6], which reduces the damage evolution equation to be fully expressed in terms of the damage variable q(t)

$$\alpha\dot{q}(t) + \beta q(t) = \frac{k}{2}\frac{(1-q(t))\omega^2|V|^2}{\left(\omega^2-(1-q(t))^2\omega_0^2\right)^2 + 4\zeta^2\omega_0^2\omega^2}, \tag{6.3}$$

where ω is the excitation frequency and ω_0 is the undamaged natural frequency. Conveniently, eq. (6.3) is separable and admits the explicit solution

$$t = t_0 + \int_{q_0}^{q} \frac{\alpha\, d\xi}{\frac{k}{2}\frac{(1-\xi)\omega^2|V|^2}{\left(\omega^2-(1-\xi)^2\omega_0^2\right)^2 + 4\zeta^2\omega_0^2\omega^2} - \beta\xi}, \tag{6.4}$$

where we write $q_0 = q(t_0)$. Alternatively, the equation of evolution (6.3) can be recast in terms of dimensionless variables as

$$\frac{dq}{d\tau}(\tau) + q(\tau) = \frac{(1-q(t))w^4\varepsilon}{\left(w^2-(1-q(\tau))^2\right)^2 + 4\zeta^2w^2}, \tag{6.5}$$

where

$$\tau = \frac{t-t_0}{t_r},\qquad t_r = \frac{\alpha}{\beta},\qquad w = \frac{\omega}{\omega_0},\qquad \varepsilon = \frac{k|V|^2}{2\beta\omega^2} \tag{6.6}$$

whereupon (6.4) becomes

$$\tau = \int_{q_0}^{q} \frac{d\xi}{\frac{(1-\xi)w^4\varepsilon}{\left(w^2-(1-\xi)^2\right)^2 + 4\zeta^2w^2} - \xi}. \tag{6.7}$$

From this reparametrization, we observe that the evolution of damage depends on the following dimensionless parameters: i) the ratio of the elapsed time to the relaxation time t_r for healing, ii) the ratio w between the frequency of insonation and the undamaged natural frequency, iii) the energy deposited by insonation relative to the energy cost of repair, and iv) the cell damping ratio.

In particular, eq. 6.7 and 6.5 result in the damage evolution for one insonation pulse of LIPUS. To obtain a combined equation of evolution describing the evolution of the system over larger numbers of duty cycles, we analyze the problem by means of fractional time stepping. The duty cycle under consideration consists of an on-period of scaled duration $\tau_1 = T_1/t_r$ and an off-period of scaled duration $\tau_2 = T_2/t_r$. The entire scaled duration of the duty cycle is $\tau_1 + \tau_2$. Finally, it can be shown that the time-to-death of a single cell is given by

$$t = t_r \int_0^{q_c} \frac{d\xi}{\dfrac{\lambda(1-\xi)w^2\varepsilon}{\left(w^2-(1-\xi)^2\right)^2 + 4\zeta^2 w^2} - \xi}, \tag{6.8}$$

where

$$\lambda = \frac{\tau_1}{\tau_1+\tau_2}, \qquad 1-\lambda = \frac{\tau_2}{\tau_1+\tau_2}, \tag{6.9}$$

are the on-time fraction of the duty cycle, or duty factor, and the off-time fraction, respectively.

Cell-dead fraction due to cell-to-cell variability

A typical population of cancerous cells exhibits broad variation in geometry and mechanical properties. In order to capture this gradual cell necrosis, we regard the parameters governing the evolution of the cells as random and a cell population as a sample drawn from the probability distribution of the parameters.

We see from eq. (6.8) that the time-to-death $t_c = \tau_c t_r$ depends on the cell parameters $(t_r, \omega_0, \zeta, q_c)$, respectively, the relaxation time for healing, the natural frequency of vibration, and the damping ratio; and on the process parameters $(\varepsilon, \omega, \lambda)$, respectively, the energy intensity, frequency, and on-period fraction of the insonation. For simplicity, we assume that the process parameters can be controlled exactly and are uncertainty-free. Contrariwise, the cell parameters define a random variable $X \equiv (t_r, \omega_0, \zeta, q_c)$, with probability distribution reflecting the variability of the cell population.

Owing to the randomness of the cell population, the time-to-death t_c itself defines a random variable Y. In terms of these random variables, (6.8) defines a relation of

the form

$$Y = f(X). \tag{6.10}$$

In order to estimate the variability in the time-to-death random variable Y, we make a small-deviation approximation

$$Y \approx f(\bar{X}) + Df(\bar{X})(X - \bar{X}) + h.o.t., \tag{6.11}$$

where

$$\bar{X} = \mathbb{E}(X) \equiv (\bar{t}_r, \bar{\omega}_0, \bar{\zeta}, \bar{q}_c) \tag{6.12}$$

is the mean value of the cell parameters and $Df(\bar{X})$ are sensitivity parameters. The average time-to-death then follows as

$$\bar{Y} = \mathbb{E}(Y) \approx f(\bar{X}) + h.o.t. \tag{6.13}$$

We note that, for small deviations, the mean time-to-death of the cell population is obtained by evaluating (6.14) at the mean value $\bar{X} = (\bar{t}_r, \bar{\omega}_0, \bar{\zeta}, \bar{q}_c)$ of the cell parameters, cf. eq. (6.13), with the result

$$\bar{t}_c = \bar{t}_r \int_0^{\bar{q}_c} \frac{d\xi}{\dfrac{\lambda(1-\xi)\bar{w}^4\varepsilon}{\left(\bar{w}^2 - (1-\xi)^2\right)^2 + 4\bar{\zeta}^2\bar{w}^2} - \xi}, \tag{6.14}$$

where we write $\bar{w} = \omega/\bar{\omega}_0$ and we assume that (5.47) is satisfied with $q_c = \bar{q}_c$.

However, for large deviations, we model heterogeneous cell responses by simulating the behavior of a population of cells. First, we run sets of many simulations representative of cell-to-cell variability on cell parameters. Let $X_1, ..., X_N$ be the random sampling drawn from the probability distribution of the physiological parameters of the cell given by $\mathcal{F}$, such that

$$X = \{X_1, X_2, ...X_i, ..., X_N\} \quad \text{with} \quad X_i = \{t_{r_i}, \omega_{0_i}, \xi_i, q_{c_i}\}. \tag{6.15}$$

The cell-death time is computed by means of the reduced model with

$$t_c = t_r \int_0^{q_c} \frac{d\xi}{\dfrac{\lambda(1-\xi)w^4\varepsilon}{\left(w^2 - (1-\xi)^2\right)^2 + 4\zeta^2 w^2} - \xi}, \tag{6.16}$$

which leads to a vector of cell-death times,

$$t_c = \{t_{c_1}, t_{c_2}, ..., t_{c_i}, ..., t_{c_N}\}. \tag{6.17}$$

Then, the simulated (or empirical) distribution function (SDF), $\hat{Y}$, is a cumulative distribution function,

$$\hat{Y}(T|X) = \frac{\#\text{elements in sample} \leq T}{N} = \frac{1}{N}\sum_{i=1}^{N} I(t_i < T), \tag{6.18}$$

where $I(\cdot)$ is the indicator function. The SFD first and second moments can then be compared to the experimental CDF. Ideally, the distribution for each parameter would come from independent tests at the conditions of the experiments.

6.3 Influence of cell and process parameters on the oncotripsy effect

In this section, we aim to understand the influence of the mechanical properties and process parameters on the response of a single cell and cell population. We perform numerical experiments on healthy and cancerous cells for different conditions of pressure (or deposited energy), duty cycle, excitation frequency, and time of exposure and observe the influence on damage and cell-death fraction. First, we provide a summary of the cell parameters and its variability obtained in Chapter 5 by fitting the simulated cell-dead fraction to the empirical cell-dead fraction. Next, we analyze pressure *vs.* damage, damage *vs.* time and cell-dead fraction *vs.* frequency ratio, which provide bounds to the ultrasound insonation parameters.

Definition of cell parameters

The cell parameters exhibits a broad variability in geometry and mechanical properties. To capture the cell-death evolution in a cell population, we estimated the mean of cell parameters $\bar{X}$ to the experimental cell-death fraction of Mittelstein *et al.* [54] presented in Chapter 2. Subsequently, the variability of the cell parameters was calibrated to the experimental variance by establishing suitable upper and lower bounds from the biological literature. Finally, the cancerous cell parameters follow a log-normal distribution with mean and variance tabulated in 6.1.

As regards the healthy cell parameters, we do not count with cell-death fraction experiments for healthy cells. However, we know that at 500kHz, P=1.4MPa and $\lambda = 1/10$, the T-cell death is of 39.5%. In addition, experimental observations have shown that the viscosity of healthy cells is higher than for cancerous cell. Further, we assume that the healing kinetics of the cell are faster. Even though healthy cells posses less variability than cancerous cell, for this analysis we will consider them to be the same, and the mean values to be a shifted from the cancerous cell. In addition, we assume that β, and therefore ε, is equal among this cells. This implies

that, for the same energy deposited, the healthy cell will attain larger damage, but with faster recovery. Finally, for a healthy cell, we obtain the parameters tabulated in 6.2.

Table 6.1: Mean and variance for the cancerous cell parameters from calibration to experiments t_r, ω_0, ξ and q_c.

	t_r	ω_0	ζ	q_c
Mean	100 sec	1000π kHz	0.7	0.136
Variance	10 sec^2	125 π kHz^2	0.175	0.0136

Table 6.2: Proposed mean and variance for the healthy cell parameters t_r, ω_0, ξ and q_c.

	t_r	ω_0	ζ	q_c
Mean	50 sec	2000 π kHz	1.0	0.2
Variance	10 sec^2	125 π kHz^2	0.175	0.0136

Bounds on the insonation parameters through numerical simulations

Figure 6.1 shows the total damage *vs.* pressure (in MPa) at 60 seconds of exposure, for a duty cycle of 10% and 50% and different frequency ratios w. In general, the healthy cell attains less damage than the cancerous cell. Cell death will only occur if the total damage surpasses a critical value of q_c. At low pressures, the maximum damage is reached at resonance, i.e., w=1. On the contrary, at high pressures — 2 MPa ($\lambda = 1/10$) for the cancerous cell and 2.25 MPa ($\lambda = 1/10$) for the healthy cell — the total damage is large enough to shift the damaged natural frequency of the cell to be in resonance with the excitation. Increasing the duty cycle brings forward the frequency shift to 1 MPa for the cancerous and healthy cells. Figure 6.2 shows a closer inspection of the damage evolution at 3MPa. At 60 seconds, for the cancerous and healthy cell, the greatest damage occurs at a natural frequency above resonance. The previous figures imply that, depending on the time of exposure and insonation pressure, different strategies could be considered. For low pressures/low insonation times one may expect the change of the damaged natural frequency to be small, i.e., $\mathrm{w}_d \approx$w —with w_d the excitation to damaged natural frequency ratio— and not influence the oncotripsy effect. Furthermore, the gap between healthy and cancerous cells is not expected to change. On the contrary, for large pressures/exposure times, the damaged ratio will drastically change so that $\mathrm{w}_d \ll$ w and affect the frequency

gap between the cells. In this case, the best solution would be to work further away from the resonant frequency of the healthy cell.

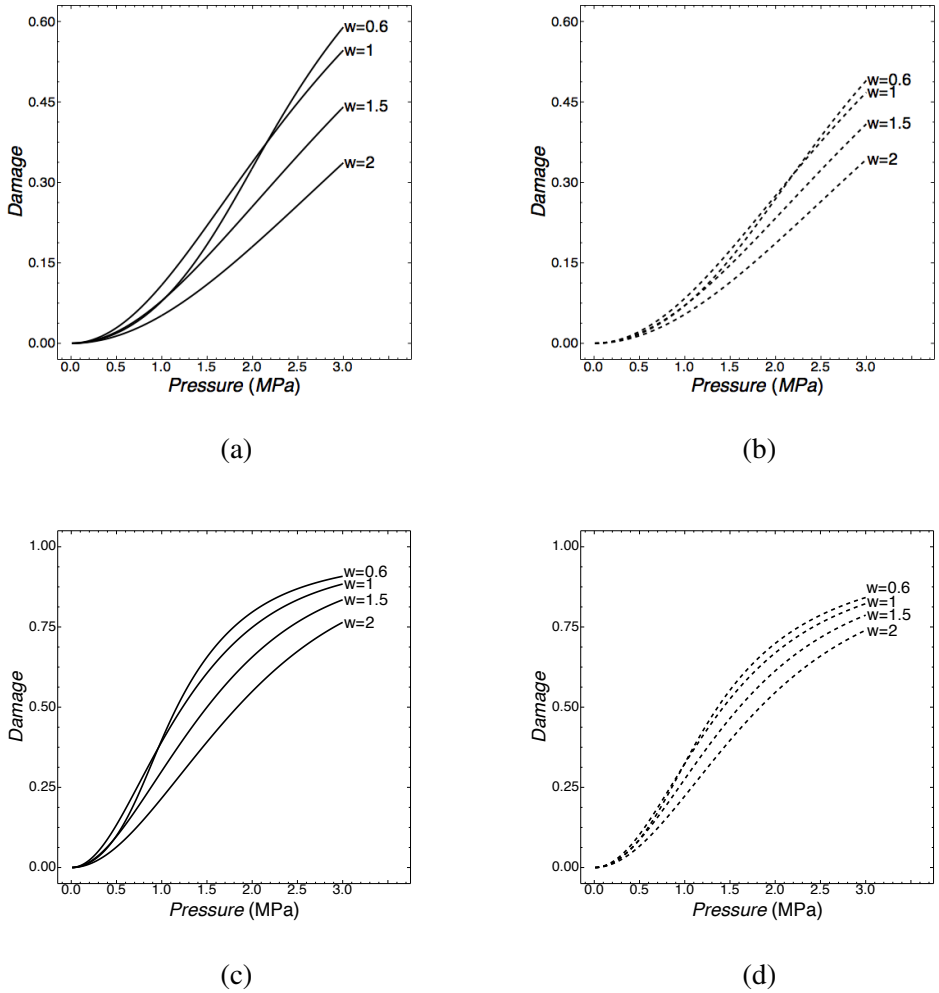

Figure 6.1: Total damage *vs.* pressure (in MPa) at 60sec exposure time and duty cycles of $\lambda = 1/10$ and $\lambda = 1/50$ for a cancerous cell with parameters $\xi = 0.7$, $t_r = 100$sec, $q_c = 0.1$ and a healthy cell with parameters $\xi = 1$, $t_r = 50$sec, $q_c = 0.2$. The damage is shown for different ratio w. (a) Cancerous and (b) healthy at $\lambda = 1/10$. (c) Cancerous and (d) healthy at $\lambda = 1/50$.

Figure 6.3 presents the mean time-to-death (in sec) *vs.* pressures (in MPa) for a duty cycle of 10% and 50% for the ratio w=1. These plots remind us of the typical S-N or W*ö*hler curve for high-cycle fatigue, which describes the relationship between the cyclic stress amplitude (S) and the number of cycles to failure (N). Here, we choose to represent a curve given by the cyclic pressure amplitude at the focus (P) and mean time-to-death (t_c). The P-t_c curve presents some important

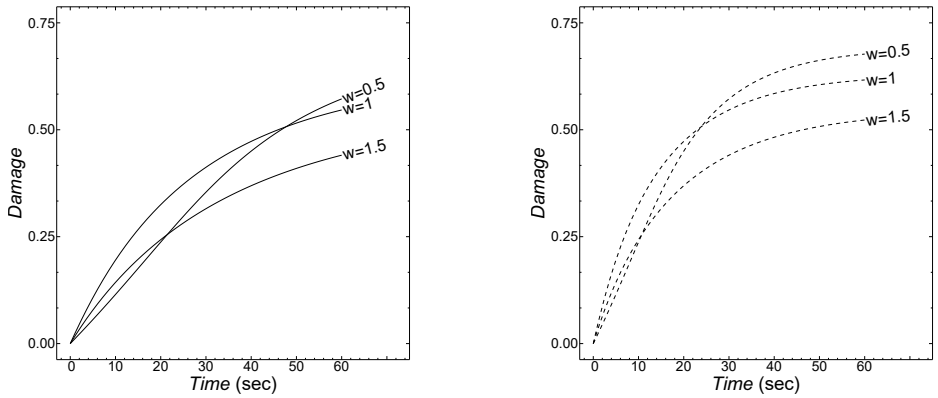

Figure 6.2: Damage *vs.* time on a cancerous cell with parameters $w = 0.5, 1, 1.5$, $\xi = 0.7$, $t_r = 100$sec, $q_c = 0.1$ and a healthy cell with parameters $w = 0.5, 1, 1.5$, $\xi = 1$, $t_r = 50$sec, $q_c = 0.1$. The process parameters are P=3MPa and $\lambda = 1/10$. a) Cancerous. b) Healthy.

characteristics. For both cancerous and healthy cells, even if both have the same natural frequency, it is suggested that there is a pressure level or threshold below the which cell death would not be observed (in the mean sense). In these particular examples, the pressure limit is ~1.5MPa for healthy and ~0.75MPa for cancerous. In mechanics, this threshold is known as the *fatigue limit* or *endurance limit*, and it depends on the cell parameters, the process parameters, and other factors not considered in the model, such as residual damage from a previous process or the chemical composition of the environment. Below this limit, the cell exhibits an "infinite" life. In engineering, this "infinite" life is considered to be 1 million cycles, beyond which the material would fail. For a cell initially in resonance, i.e., $w = 1$, the limit would be located at $N = \frac{2\pi}{\omega}\lambda t_\infty$ where t_∞ is the infinite time-to-death. Thus, for our test cases and considering 300 sec to be at infinity, the limit would be at $N_c = 15$million and $N_h = 21$million cycles for cancerous ($f_0 = 500$kHz) and healthy ($f_0 = 1000$kHz) cells, respectively. This observation implies that healthy and cancerous cells will eventually die after very long exposure times. A comparison of both limits displays a significant pressure gap, implying there are pressures for which one could kill abnormal cells while leaving the normal intact (in the mean sense). Moving on to the effect of the duty cycle, Figure 6.3a and b show that the limit threshold and pressure gaps decrease while increasing the duty cycle. It can also be observed that the fatigue limit initiates at an earlier time, suggesting that the

infinite time-to-death has been reduced. These observations are related to the duty cycle increasing the on-period, thus increasing the total damage on the fibers, while decreasing the off-period, i.e., reducing the time to recover.

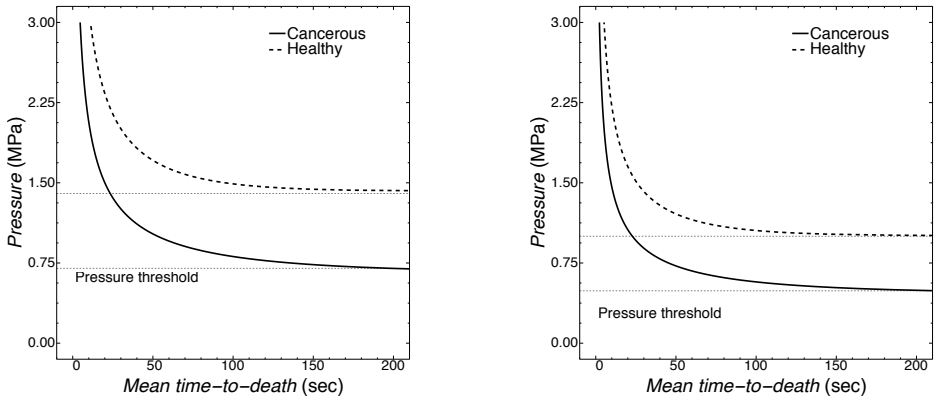

(a) (b)

Figure 6.3: Mean time-to-death (in sec) at different pressure (in MPa) for a cancerous cell with parameters $w = 1$, $\xi = 0.7$, $t_r = 100$sec, $q_c = 0.1$ and a healthy cell with parameters $w = 1$, $\xi = 1$, $t_r = 50$sec, $q_c = 0.1$ a) $\lambda = 1/10$. b) $\lambda = 1/2$.

Lastly, Figure 6.4a. and b. shows the cell-dead fraction *vs.* excitation frequency for the duty cycle and pressure of the experiments [54]. As expected, the viability of the cell population decreases towards resonance. Even at resonance, the healthy population shows larger survival because of its higher viscosity. Regardless of the frequency gap between cells, as the applied pressure is near the pressure limit of the healthy cell at 1.5MPa (see Fig. 6.3), its cell-dead fraction at 60 seconds is not negliglible (∼37%). An optimized solution will require to work at lower exposure time or pressures (see Figure 6.4 c and d). Table 6.3 shows different possibilities to guarantee the demise of the cancerous without damage of healthy cells. In this particular example of only two unimodal cells, the best option is to reduce the frequency of the excitation to 270kHz which leads to 60% to 0.2% cell-dead of cancerous to healthy. However, if the healthy cell has another resonant frequency below the cancerous cell, then the optimal solution would be to reduce the pressure to 1MPa.

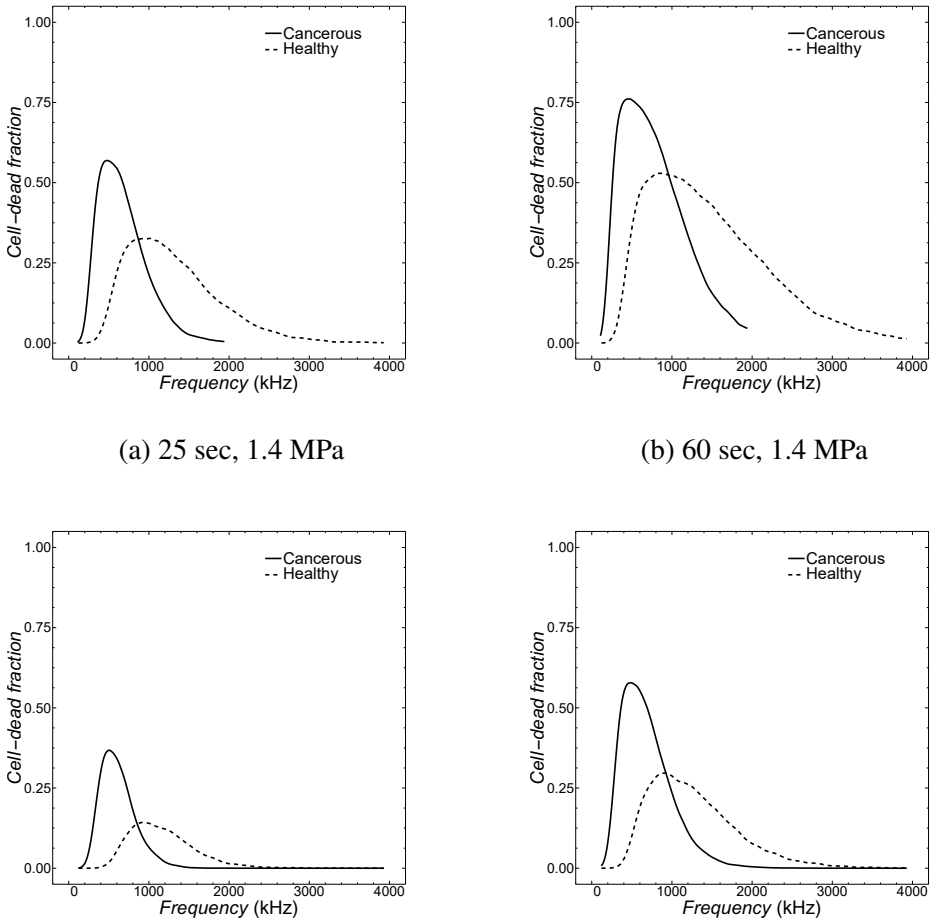

(a) 25 sec, 1.4 MPa

(b) 60 sec, 1.4 MPa

(c) 25 sec, 1 MPa

(d) 60 sec, 1 MPa

Figure 6.4: Cell-dead fraction for a cancerous and healthy cell for a duty cycle 10, exposure times of 25 and 60 seconds, and pressures of 1 and 1.4 MPa.

Table 6.3: Variability in cell-dead (CD) ratio of healthy (h) to cancerous cell (c) for different conditions of frequency, pressure and exposure time.

Frequency (kHz)	**Pressure (MPa)**	**Exposure Time (sec)**	λ	$\mathbf{CD}_h$	$\mathbf{CD}_c$	Δ**CD**	$\mathbf{CD}_h/\mathbf{CD}_c$
500	1	25	0.1	0.018	0.376	0.358	0.05
500	1	60	0.1	0.104	0.583	0.479	0.18
500	1.4	25	0.1	0.121	0.569	0.447	0.21
500	1.4	60	0.1	0.366	0.758	0.392	0.482
270	1.4	60	0.1	0.02	0.609	0.589	0.03

6.4 Quantitative oncotripsy

In this section we study which values of ultrasound frequency are more desirable to minimize death of healthy cells. As observed in the experiments of Mittelstein *et al.* [54], even thought healthy cells present minimal death at the frequencies studies, their death still occurs and is also frequency and time dependent. Therefore, given two cells, one cancerous and another healthy, we ask the question: which is the best combination of pressure, time of exposure, and frequency, such that we minimize the death of healthy cells and we maximize the one for cancerous cells.

In this study, our attention will be focused on understanding the susceptibility of the cell-dead fraction through contour plots on the frequency domain. Our observations will be based on the following assumptions:

- The ultrasound loading parameters are known and deterministic.
- The probability distribution, mean and standard deviation of the material parameters are known.
- The cancerous and healthy cell are unimodal, i.e., they only have one principal natural frequency.
- The damage q(t) on the cell is homogeneous and follows the dynamical reduced model of oncotripsy.
- The range of pressures is below the cavitation threshold. If inertial cavitation is present, we consider that amplifies the effect of oncotripsy by modifying the pressure surrounding the cells, which effectively affects the coefficients α and β.

Oncotripsy charts

To aid the selection of ultrasound parameters, this section provides a comprehensive Ashby-type ultrasound parameter selection charts to maximize the therapeutic effect on cell populations. Due to the variability of mechanical and kinetic properties, it is expected that some overlap of natural frequencies exist between healthy and cancerous cells. For instance, under the same ultrasound conditions, Mittelstein *et al.* [54] found 100% cell-dead fraction of leukemia cell lines K-562 and U-937 and $\approx$50% of breast normal cells. As observed in Fig. 6.4, the cell-dead amplification due to resonance extends along with the frequency domain which suggests that any frequency in the neighbor of the natural frequency could potentially be used for

oncotripsy. What is more, as seen in Fig. 6.1, high enough pressures or duty cycles leads to high cell-dead fraction on normal and unhealthy cells, overshadowing the oncotripsy effect.

To address the difficulty of ultrasound parameter selection, we create *Oncotripsy charts*, where we employ the previously explained reduced dynamical model to quantify the effectiveness of oncotripsy in the frequency domain under several process attributes. Through numerical simulations, we analyze the cell-dead fraction on the frequency domain under the influence of several process parameters. The cells are modeled following the properties presented in section 6.3. Through these charts, we will be able to quantify the frequencies that results in maximum demise of cancerous cells while keeping healthy cells intact. We define this region as the *optimal therapeutic ultrasound frequency*. Generally, this can be represented as an optimization problem of the form,

$$\min_{\omega \in \Omega, p \in P} f(\omega) = \frac{f_h(\omega)}{f_c(\omega)}, \tag{6.19}$$

where $f_c(\omega), f_h(\omega)$ are positive, continuous and concave and represent the cell-dead fraction of the cancerous and healthy cells for a excitation frequency ω in a nonempty convex set Ω and certain process parameters p in a set P. For a collection of cell types, this optimization is multi-objective.

Contours plots showing the cell-dead fraction in the frequency domain for three different pressures, P = 0.5MPa, P = 1MPa, and P = 1.5MPa, for 10% duty cycle and after 10, 25 and 60 seconds of exposure to ultrasound are presented next. The plots indicate the dead-cell fraction against the ratio between the excitation and resonance frequencies, at constant pressure, duty cycle, and exposure time. We recall that the cell-dead fraction ranges from 0 to 1, where 1 represents the full demise of the cell. We remark that the dead-cell fraction is computed with the aforementioned reduced model by sampling the random variable X = $(\omega_0, t_r, \xi, q_c)$ from a log-normal distribution. The ranges for both therapeutic and natural frequencies span from 100 kHz to 1.5 MHz. These charts demonstrate several patterns in the demise of both healthy and cancerous cells that are targeted by therapeutic ultrasound. For a fixed set of ultrasound parameters, the maximum dead-cell fraction in cancerous cells is higher compared to healthy cells (see Fig.6.5, 6.6, and 6.7). We also observe that for longer exposure to ultrasound frequency and higher pressure increases the probability of cell death. Moreover, we observe the highest cell-dead fraction occurs

along the resonance line $f/f_0 = 1$. Additionally, it is shown that the susceptibility to the oncotripsy effect increases with increasing excitation frequency.

We remark that the quantitative results could be partially altered by changing certain assumptions in the computational model. This could stem from different physical, biological, or mathematical considerations. These possible changes, originating from employing a distinct model or set of assumptions, in turn, might lead to a different set of oncotripsy charts. Nevertheless, similar patterns will prevail.

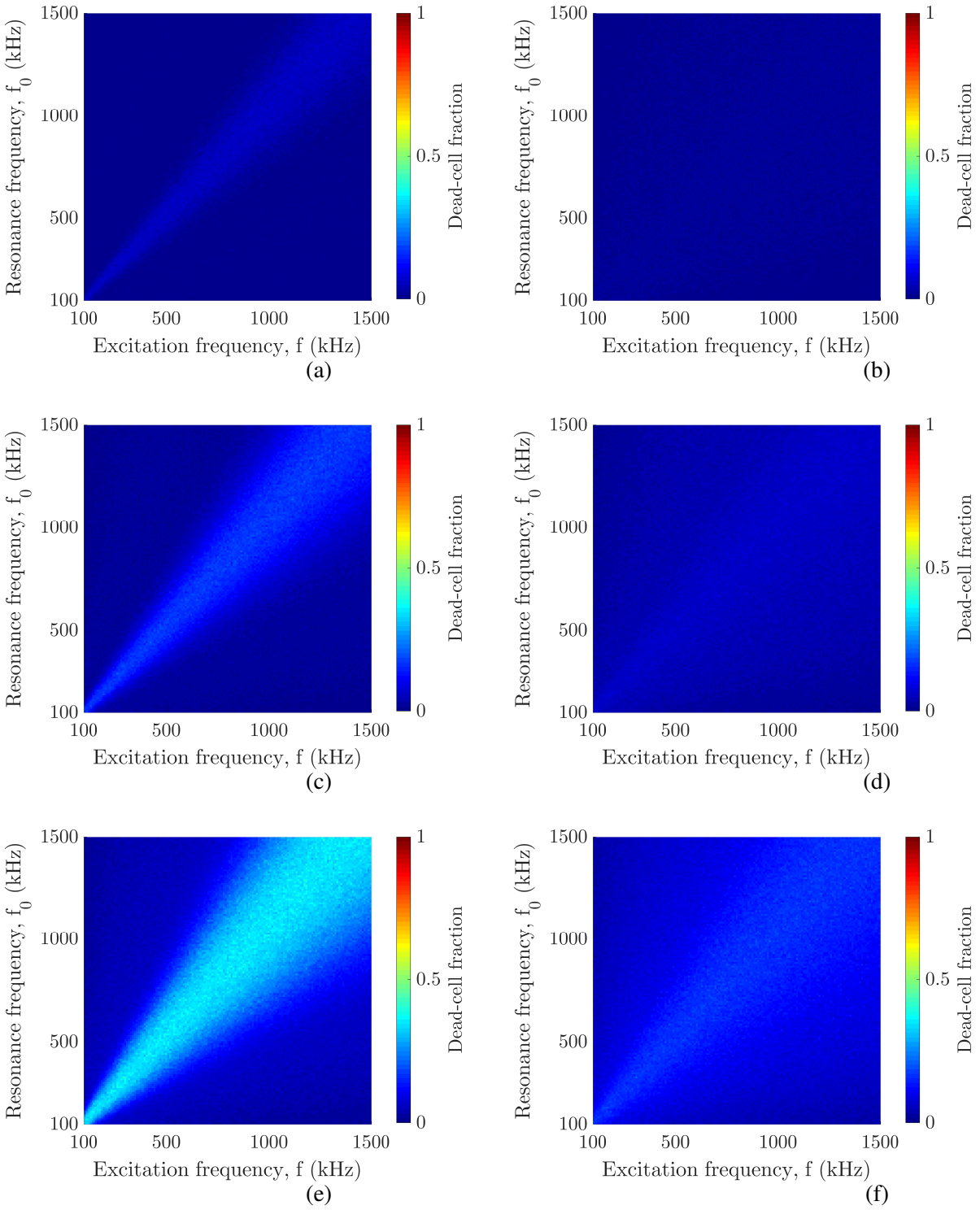

Figure 6.5: Oncotripsy charts for ultrasound pressure $P = 0.5$ MPa. (a), (c) and (e) demonstrate the dead-cell fractions for cancerous cells after 10, 25 and 60 seconds of exposure to ultrasound, respectively. Similarly, (b), (d) and (f) demonstrate the dead-cell fractions for healthy cells after 10, 25 and 60 seconds of exposure to ultrasound, respectively.

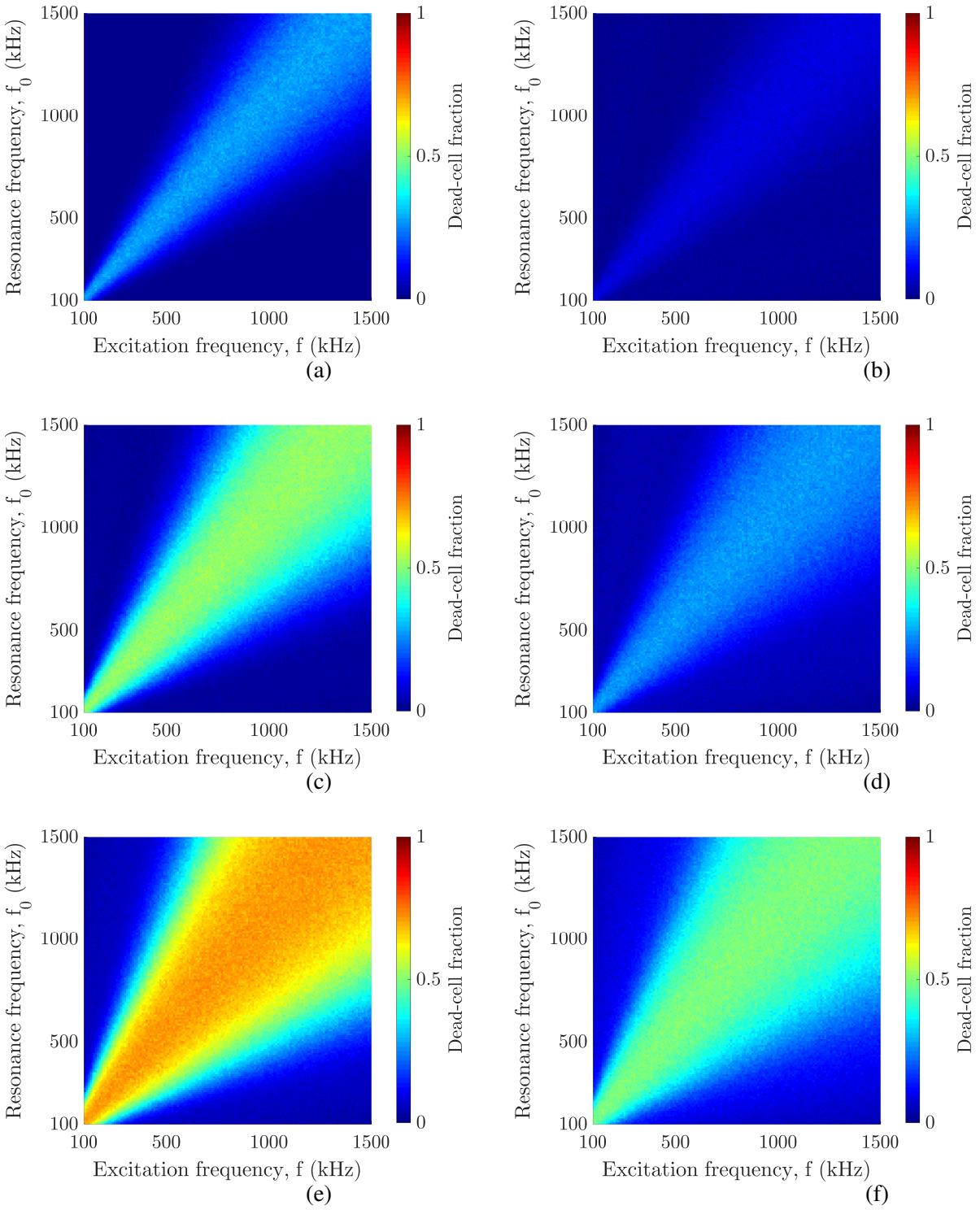

Figure 6.6: Oncotripsy charts for ultrasound pressure P = 1 MPa. (a), (c) and (e) demonstrate the dead-cell fractions for cancerous cells after 10, 25 and 60 seconds of exposure to ultrasound, respectively. Similarly, (b), (d) and (f) demonstrate the dead-cell fractions for healthy cells after 10, 25 and 60 seconds of exposure to ultrasound, respectively.

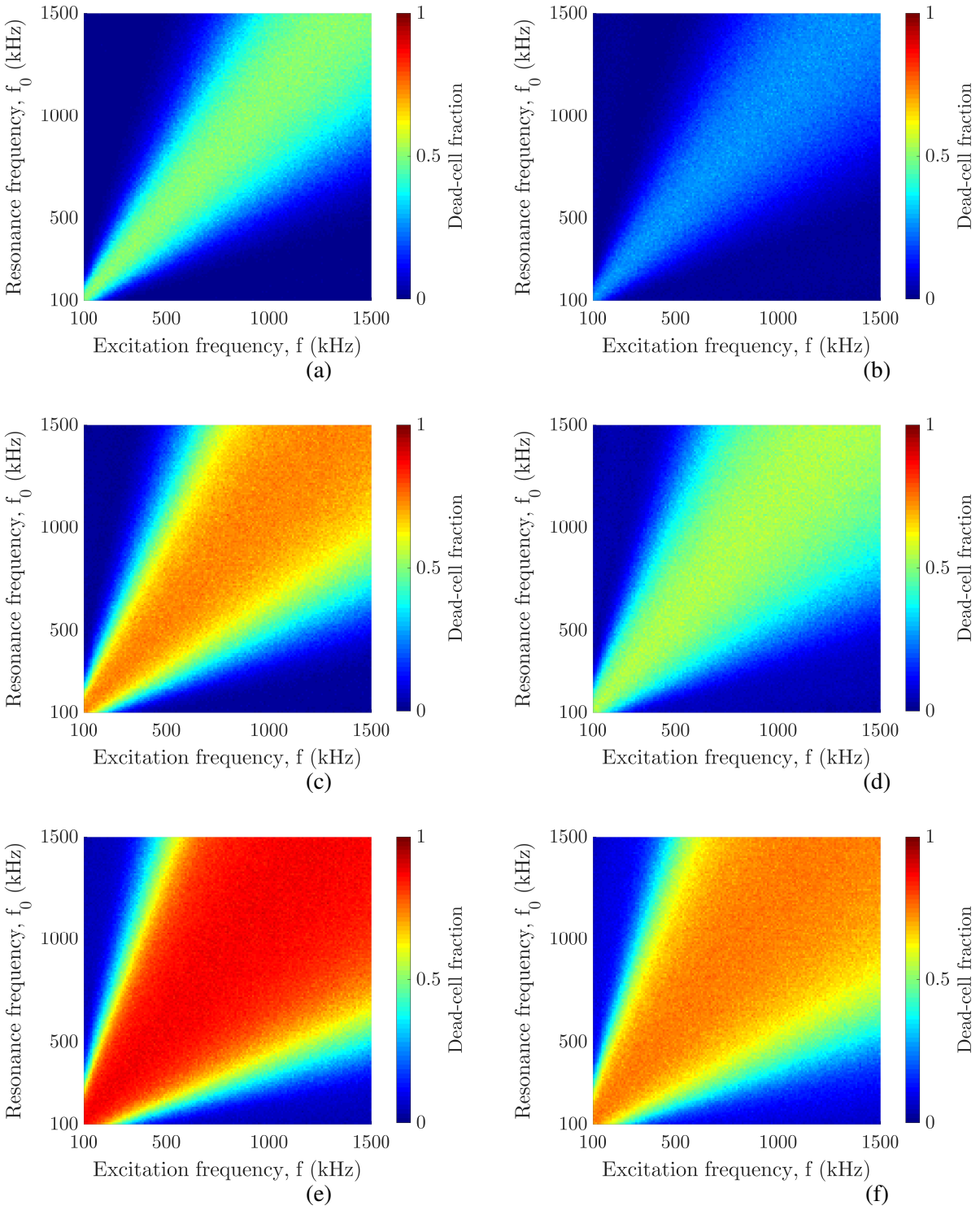

Figure 6.7: Oncotripsy charts for ultrasound pressure P = 1.5 MPa. (a), (c) and (e) demonstrate the dead-cell fractions for cancerous cells after 10, 25 and 60 seconds of exposure to ultrasound, respectively. Similarly, (b), (d) and (f) demonstrate the dead-cell fractions for healthy cells after 10, 25 and 60 seconds of exposure to ultrasound, respectively.

6.5 Discussion:parameters selection and performance indices

The objective of this section is to demonstrate the means of incorporating oncotripsy analysis into realistic and clinical applications. While we primarily deal with human cells and tissues, oncotripsy procedures are general and potentially applicable to other living organisms. We will focus on constructing an index which could be utilized in determining optimal therapeutic ultrasound frequencies, for a given type of cell or tissue. We then present *clinical oncotripsy charts* as a potential guide for treating different tissues in human subjects.

DHCR: death of healthy to cancerous cell ratio

As mentioned in the previous section, we aim to characterize the optimal therapeutic ultrasound frequency for *in vivo* clinical applications. In clinical cases that the cancerous cells are clustered at a region, that region would be the target of ultrasound focus, and healthy cells would remain intact for the most part. In this case, which dominates the advanced stages of cancer, oncotripsy charts could be utilized to treat the cancerous cells with an ultrasound frequency that leads to the maximum demise of cancerous cells. Based on the results presented in the previous section, for a given cell type, therapeutic ultrasound frequencies that are equal or very close to the corresponding resonant frequency will cause maximum death in the cancerous cells.

On the other hand, particularly in the early stages of cancer, cancerous cells are not segregated from the healthy ones [77]. The ultrasound focus will target both cancerous and healthy cells in this case, whereas we naturally aim to minimize the annihilation of healthy cells. This raises up the question of '*what is the optimal therapeutic ultrasound frequency?*' where we define optimal therapeutic frequency as the excitation frequency that simultaneously maximizes the demise of cancerous cells and minimizes the healthy cell deaths.

Prior to obtaining the optimal frequency for a specific tissue, one needs to characterize the frequencies of resonance for both the corresponding cancerous and healthy cells. Additionally, it often occurs that several types of cells are adjacent to each other, in which case obtaining the optimal frequency requires a multi-objective analysis. For instance, if cancerous and healthy cells of a specific tissue -such as breast- lie adjacent to each other in a neighborhood where white blood cells and other cell types exist, one needs to obtain the resonant frequencies for all of them and look for optimal frequencies that lead to the minimal demise of healthy cells.

Here we consider the case that only one pair of cancerous and healthy cells with similar frequency of resonance exists at the focus of therapeutic ultrasound. In this case, response to the above question, for the case, lies in defining an index I which represents the death of healthy to cancerous cells ratio (DHCR)

$$I = \frac{D_h}{\sqrt{D_c}}, \tag{6.20}$$

where D_c and D_h respectively represent the death-cell fraction for cancerous and healthy cells. This index prevents D_h from outweighing D_c by including the square root in the denominator. Note that since $0 \leq D_h < D_c < 1$, we will have $\sqrt{D_c} > D_c$. Let us clarify this with an example. Consider the comparison of two cases, one with $D_h = 0.03$ and $D_c = 0.15$ and the other with $D_h = 0.1$ and $D_c = 0.5$. Had we defined the ratio as a simple ratio of the cell-dead fractions, i.e., $I = D_h/D_c$, then both cases would be labeled identically. Yet in the second case, half of the cancerous cells are demolished with ultrasound, which is very desirable. The current definition of the healthy-to-cancerous death ratio leads to values of 0.0775 and 0.1414 for the first and second cases, respectively. Therefore, the index presented favors the second scenario.We emphasize that the choice of index is non-unique. We then compute this index for three different pressures: P=0.5 MPa, P=1 MPa, and P=1.5 MPa. We choose a threshold value, I_m, which corresponds to the maximum desirable DHCR. Without loss of generality, we have chosen $I_m = 0.1$ meaning that all the scenarios (i.e., ultrasound parameters) that lead to $I < I_m$ are labeled as desirable, and anything above that value is considered as unfavorable. The results for each pressure after 10 and 60 seconds of exposure to ultrasound are presented in Fig. 6.8, where the desired frequency ranges are shown in black.

Our results essentially show that optimal frequency ranges lie in a region away from the $f = f_0$ line. As shown previously, increasing the pressure will significantly increase the death probability of both cancerous and healthy cells. This occurs in a way that leads to a shrinkage of the optimal therapeutic frequencies, as seen in Fig. 6.8. We remark here that the size of this optimal region evidently depends on pressure level and threshold value I_m. In fact, we repeated our calculations for different values of I_m and observed that the demonstrated patterns remain invariant. We thus propose a new framework for the oncotripsy procedure in which, for the case of desegregated cancerous and healthy cells or when the cluster of cancerous cells is 'smaller' than the ultrasound focus, the optimal frequencies lie in a region distinct from the $f = f_0$ neighborhood.

For this optimization problem, the maximum pressure threshold for minimum healthy cell-dead fraction can be found by computation of the P-t_c curve, as shown in Fig. 6.3 in section 6.3. Simultaneously, the damage curves — parameterized by the frequency ratio — can be compared between healthy and cancerous cell.

Clinical Charts

Frequency of resonance, which is rarely measured directly in the experiments, is the primary physical property of a cell which plays the key role in the oncotripsy analysis. Therefore, in order to incorporate the oncotripsy procedure and the corresponding charts in clinical applications, one needs to compute the resonance frequency for the cell of interest indirectly. This significantly hinges on gathering accurate experimental data for the elastic properties and geometry of each cell. In this section, we aim to look into resonance frequencies for both cancerous and healthy cells in certain tissues of human subjects and adopt the previously obtained oncotripsy charts to suggest effective therapeutic ultrasound frequencies for each type of cell.

In order to compute the resonance frequency, we borrowed experimental data for elastic properties and cell diameter from the literature. We also made the following relevant assumptions: (i) we assume that cells have spherical shapes, and (ii) their densities are identical to water. Based on the diameters reported in experiments, we then compute mass for each type of cell. Moreover, among the elastic properties of a cell, its Young modulus is often computed from the experiments. With recourse to the linear elasticity theory, we can obtain the corresponding shear modulus as

$$\mu = \frac{E}{2(1+\nu)}, \tag{6.21}$$

where E, μ and ν are the Young modulus, shear moduli, and Poisson ratio, respectively. For these computations, we consider the shear modulus from experiments is the effective modulus of the cell. Finally, we compute the frequency of resonance for several cell types by incorporating the data acquired from literature, as summarized in Table 6.4. Note that each type of cell has a non-negligible variation in its mechanical properties. This primarily stems from the complexity of conducting mechanical experiments, such as atomic force microscopy, on the cellular level as well as the biphasic nature of cells.

With recourse to the data presented in Table 6.4 and our previous findings, we propose oncotripsy clinical charts. The primary idea in this approach is to map the

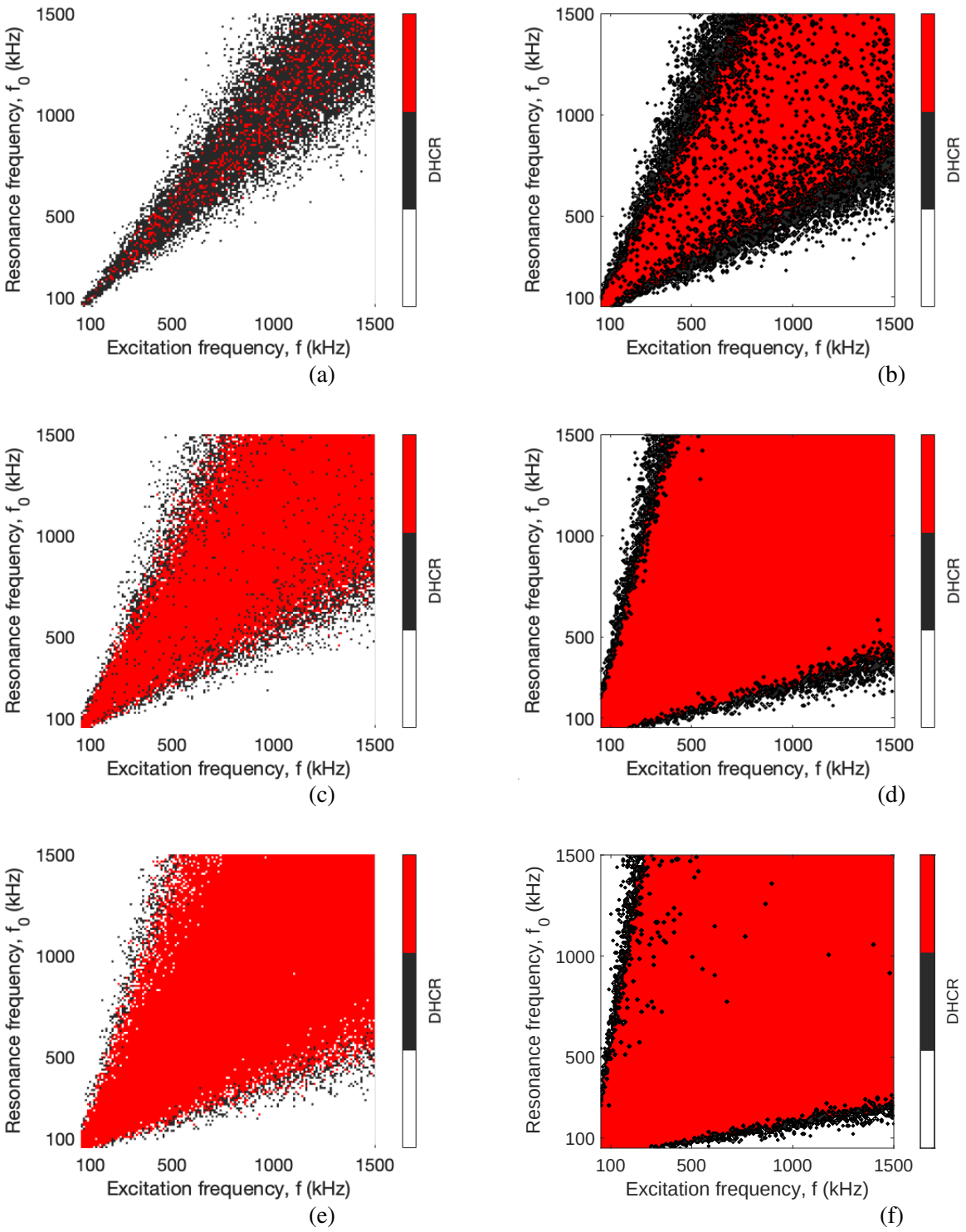

Figure 6.8: Death of healthy to cancerous cell ratio (DHCR) plots. The ultrasound values leading to DHCR less than 10% are shown in black, while the red region corresponds to larger values. In the white region, cells with the corresponding resonant frequency are not affected by the therapeutic ultrasound. (a) P=0.5 MPa and after 10 seconds of exposure; (b) P=0.5 MPa and after 60 seconds of exposure; (c) P=1 MPa and after 10 seconds of exposure; (d) P=1 MPa and after 60 seconds of exposure; (e) P=1.5 MPa and after 10 seconds of exposure; (e) P=1.5 MPa and after 60 seconds of exposure,

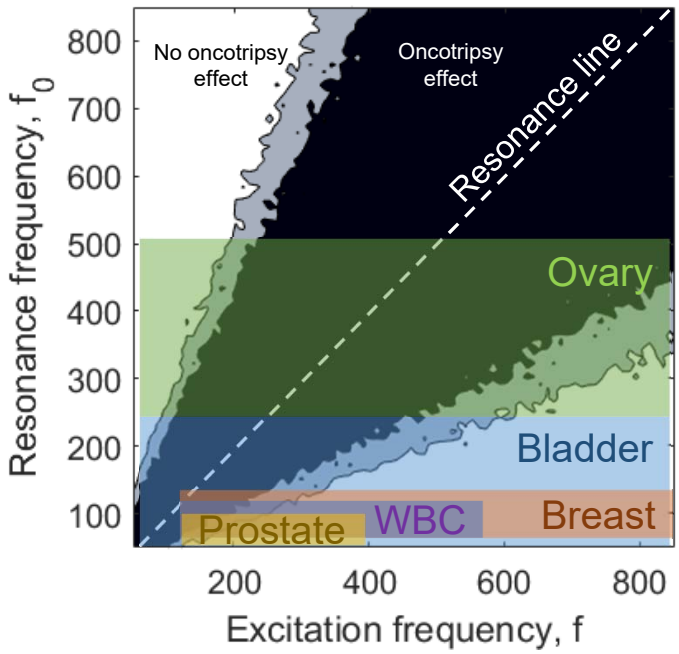

Figure 6.9: Sketch presenting delimitation of resonance frequencies (in kHz) for different tissues, combining healthy and cancerous. The resonant ranges were obtained theoretically using mechanical properties and sizes from the biological literature. The area is delimited in colors: (black) cell-dead fraction larger than a desired threshold D_t, (gray) cell-dead fraction in the range 0-D_t and (white) no oncotripsy effect.

resonance frequencies computed from experimental data to the oncotripsy charts and determine the effective ranges for excitation frequency in therapeutic ultrasound procedures. Fig. 6.9 represents schematics of this interpretation, where each band demonstrates a type of cell within tissue in human subjects.

Table 6.4: Summary of cell properties and the corresponding resonant frequencies f_0. Note: when the diameter of a specific cell line was not found in the literature, we use the diameter of another cell from the same tissue. We also compute a second frquency of resonance, related to a two-degrees of freedom system.

Tissue	Cell line	Young modulus (kPa)	Diameter (μm)	f_0 (kHz)	References
Bladder	Healthy- HCV29	7.5 ± 3.6	20	123-213	[36, 42]
	Healthy- Hu 609	9.7 ± 3.6	20	140-242	[36, 42]
	Cancerous- BC3726	1.4 ± 0.7	20	53-92	[36, 42]
	Cancerous- T24	1 ± 0.5	20	45-77	[36, 42]
	Cancerous- Hu 456	0.4 ± 0.3	20	28-50	[36, 42]
Breast	Healthy- 184A	2.4 ± 0.3	18	81-141	[3, 41]
	Cancerous- MCF7	1.5 ± 0.4	18 ± 2	64-112	[3, 41]
	Cancerous- T47D	1 ± 0.1	15	69-120	[3, 41]
Prostate	Healthy- PZHPV-7	3 ± 0.5	30	42-13	[34, 41]
	Cancerous- LNCaP	0.5 ± 0.1	30	17-30	[34, 41]
	Cancerous- PC-3	2.4 ± 0.3	30	38-66	[34, 41]
	Cancerous- Du145	2 ± 0.3	30	35-60	[34, 41]
Ovary	Healthy- IOSE	2.5 ± 0.2	8	281-486	[10, 82]
	Cancerous- OVCAR-4	1.1 ± 0.2	8	0.04-0.07	[10, 82]
	Cancerous- HEY	0.9 ± 0.1	8	0.04-0.07	[10, 82]
	Cancerous- OVCAR-3	0.6 ± 0.1	8	0.02-0.03	[10, 82]
White Blood Cells	Healthy-Neutrophil	0.156 ± 0.067	8.3 ± 0.6	70-121	[65]
	Lymphoblast-Jurkat	0.855 ± 0.670	11.5 ± 1.5	102-176	[65]
	Lymphoblast-K-562	0.6-0.7	28	23-39	[45]
	Cancerous-U-937	0.130	8.13	62-108	[17]

6.6 Conclusion

In this work, we have presented numerical experiments using a reduced-order model that captures the dynamic response of a cell subjected to ultrasound waves.

The dynamical model is used to study the effect of focused ultrasound on the demise of cancerous cells. Under this framework, we identify a particular cell with its frequency of resonance and encodes both its mechanical and geometrical properties. We showed through pressure *vs.* mean time-to-death curves that working below a specific level of pressure, the viability of normal cells can be maximized. In the same lines, for specific pressures, the frequency of resonance may be shifted by the rate of damage on a given cell-population. Therefore, the optimal frequency gap between two cells may not be given by the simple comparison of their natural frequencies. We then proposed oncotripsy charts as a guide for clinical applications, which demonstrates the probability of cell demise against therapeutic ultrasound frequency, duty cycle, and resonance frequency. We presented these charts for both cancerous and healthy cells at three distinct values of ultrasound pressure and after different exposure times. These Ashby-type plots play a key role in determining the 'optimal' therapeutic ultrasound parameters for a given cell type in a patient-specific manner.

With the objective of maximizing and minimizing the demise of cancerous and

healthy cells, respectively, we have proposed distinct regimes of frequency depending on the stage of cancer in a patient. In the advanced stages of cancer where cancerous cells form clusters larger than the focus size of the incorporated ultrasound system, therapeutic frequencies which are equal to the resonance frequency of the cancerous cells are suggested by oncotripsy analysis. However, in the earlier stages of cancer where it has been shown that the cancerous and healthy cells are desegregated [77], ultrasound can lead to the undesirable death of healthy cells. In this case, oncotripsy charts are crucial to obtain regimes of ultrasound parameters that lead to optimal results. We showed that this regime of optimal parameters may lie away from the resonance line (i.e., $f = f_0$). Finally, we adopted different cell types as presented examples of Oncotripcy clinical charts that could serve as a selection method for the ultrasound parameters, which is based on experimental data for a wide range of cell morphology and types.

We emphasize that while altering the incorporated model might lead to changes in the quantitative results, the observed patterns would remain invariant for the most part. The provided oncotripsy charts suggest a new framework for bridging the chasm between the academic studies and clinical applications, which could be incorporated in further studies with another set of assumptions and models.

Chapter 7

CONCLUSIONS AND FUTURE WORK

In this investigation, the aim was to develop a mathematical framework to effectively target the resonance frequency of the cells under a predetermined pressure, duty cycle, and timing settings as well as to design numerical experiments that lead to medical applications. The goals were to explain the mechanism of resonance of cells in suspension theoretically, determine the control parameters for the low-intensity focused ultrasound, and predict the bounds in which cancerous cell death was likely.

In this work, we propose a damage accumulation constitutive model of the cytoskeleton under high-cycle cell fatigue. The developed model of oncotripsy is an application of cell dynamics, statistical mechanical theory of network elasticity, and 'birth-death' kinetics to describe processes of damage an repair of the cytoskeleton. Based on experiments by Mittelstein *et al.* [54] that show a cell sloshing in suspension and cytoskeleton disruption of cancerous cells while being exposed to low-intensity pulsed ultrasound excitation, we hypothesized that cell death occurs as a progressive disruption of the actin fibers.

The computational model accounts for a competition between the damage and healing of the same fiber during on and off-periods of pulsed ultrasound excitation. Furthermore, we hypothesize that the effect of the filament results in a gradual loss of cytoskeleton stiffness and that after sufficient stiffness degradation, the cell becomes unviable and dies. In addition, we assume that healing occurs predominantly in the off-periods of LIPUS, based on the idea that failed filaments heal faster when unstretched or at slightly stretched configurations and that, conversely, the ability to recover is diminished with increasing filament stretch.

Based on the theory of network elasticity, we introduced a free energy per unit volume which utilizes an internal variable that accounts for damage and recovery of fibers in particular directions. We determine the evolution of the internal variables at each material point by a linear kinetic law. Additionally, we assume a linear viscosity formulation to characterize the viscoelastic behavior of a cell. Further on, we proposed a variational constitutive update and applied the model to the study of a healthy and cancerous cell through the finite element method. We found that the model predicts the trends observed in the experiments of Mittelstein *et*

al. [54]. For a healthy and cancerous cell with different resonant frequencies, but the same viscosity and kinetic parameters, we show that the damage evolution varies concerning the frequency of excitation, pressure, time of exposure, pulse duration, and duty cycle. As expected, each cell was the most susceptible at resonance. The damage is not homogeneous and maximum in the fiber along the nucleus trajectory, and it propagates from the exterior surface of the cell to its interior, implying several potential modes of death: membrane perforation, cytoskeleton degeneration, or even nucleus fragmentation. Increasing the time of exposure, duty cycle, and pressure increases the overall damage on the cell. Nevertheless, the finite element model results to be very expensive, and it is not possible to investigate the long-term cytodisruption, as well as perform sensitivity analysis, parameter space studies, and calibration to experiments. In this regard, we propose a reduced dynamical model of oncotripsy that solves these limitations.

The reduced dynamical model is based on the assumption that the damage is isotropic, i.e., is independent of the direction, and that the cell translates rigidly through a time-dependent displacement relative to the cell membrane. Based on these ideas, the total free energy, dissipation energy and kinetic energy of the system can be computed, and, by an appeal to the Lagrange D'Alambert principle, obtained a system of two coupled equations which accounts for cell dynamics and damage accumulation. The first equation represents a damped and forced harmonic oscillator, with the material velocity of the aqueous medium supplying the forcing, which stiffness depends on the instantaneous state of damage. The second equation governs the kinetic evolution of damage state, including damage accumulation and healing. We note that under the conditions of interest, the dynamics described by the system is a multiscale problem: the period of oscillation is much smaller than the characteristic time for damage evolution. This two-time structure suggests analyzing the system of coupled equations employing WKB asymptotics, which reduces the damage evolution equation to be fully expressed in terms of the damage variable. Furthermore, we can recast the equation of damage evolution for one duty cycle in terms of dimensionless variables and conclude that the damage evolution depends on (a) the ratio of the elapsed time to the relaxation time for healing, (b) the ratio between the frequency of insonation and the undamaged natural frequency, (c) the energy deposited by insonation relative to the energy cost of repair, and (d) the cell damping ratio.

To obtain the combined equation of evolution describing the damage of the system

over many duty cycles, we analyze the problem through fractional stepping. Finally, we obtain a damage evolution equation that accounts for every duty cycle, and that, conveniently, is separable and from which we obtain the time-to-death of a single cell.

The proposed dynamical model reveals the dependence of oncotripsy on fundamental cell and process parameters. The foremost can be calibrated from cell-death data for specific cell lines. Alternatively, structural cell properties such as stiffness and viscosity can be measured independently. Tests to determine the kinetic parameters would measure the evolution of stiffness for different insonation conditions. The calibrated model can then be used as a tool for optimizing process parameters for maximum therapeutic effect.

Through pressure *vs.* mean time-to-death curves, we found that working below a specific level of pressure maximizes the viability of normal cells. In the same lines, for specific pressures, the frequency of resonance may be shifted by the rate of damage on a given cell-population. Therefore, the optimal frequency gap between a healthy and cancerous cell may not be given by the simple comparison of their undamaged resonant frequency. Contour plots of cell-dead fraction over the frequency domain at specific pressures and exposure times showed that there are bands which guarantees the minimum healthy to cancerous cell-dead ratio. The problem is then reduced to an optimization of the healthy to the cancerous cell-dead ratio on the frequency domain over a range of pressures and exposition times.

An extension of the reduced dynamical model would be to include the effects of added mass and virtual friction as proposed by Or & Kimmel [61]. Further studies regarding the role of recovery could explore other kinetic laws that incorporate a restriction in the amount of energy available for healing. Other models could account for thermal fluctuations in the cytoskeleton filaments due to the oscillations and the effect of these fluctuations effect on their rupture. In addition, in order to elucidate the application of oncotripsy in patient-specific treatments, future work should extend the mathematical study to solid tumors. In this regards, the constitutive law proposed here could result useful to model the damage and recovery of fibers. Special care should be taken with the stiffness of the tissue or cells. Such as in reinforced composite materials, the cytoskeleton — in particular the intermediate fillaments — act as a reinforcement at the junctions among cells, increasing their apparent stiffness. Also, adherent cells have smaller nucleus that when in suspension. Both this observations indicate that the frequency of resonance in tissues and gel-models

may be different to those obtained for suspensions.

Further experiments should explore the cell-dead fraction *evolution* in time for different cell populations at lower pressures and a wider variety of frequencies. These curves are essential to calibrate the model and obtain the critical damage and kinetic parameters. These experiments would also serve to identify an optimal ultrasound intensity and validate and verify the reduced model. The issue of cavitation in Mittelstein *et al.* [54] is intriguing and should be explored in further computational and experimental research.

This theoretical and computational contribution will be fundamental to guide laboratory research in the prediction of bounds for targeted frequencies and to develop a patient-specific noninvasive cancer treatment without risking damage to healthy tissue. Theoretical understanding, such as provided by the proposed dynamical model, is critical for interpreting experimental observations and formulating new and improved clinical therapies. In this regard, several possible therapies suggest themselves as potential clinical applications of oncotripsy. Thus, due to genomic instability and being in different states within the cell cycle, cancer cells are highly heterogeneous at any given moment. As such, it is unlikely that a single set of acoustic parameters can kill an entire cancer cell population. This observation suggests exploiting oncotripsy in connection with other synergistic cancer therapies such as immunogenic cell death (ICD). In this combination, oncotripsy does not need to kill every last cancer cell to be effective, as long as it can induce ICD of sufficient cancer cells to trigger the host immune system to destroy the remaining cancer cells (abscopal effect). In this vein, research could usefully explore the effect of oncotripsy on tumor growth to estimate tumor progression and evaluate on the effectivity of oncotripsy against other cancer treatment therapies. Again, these and other fundamental questions suggest helpful directions for further research.

Appendix A

APPENDICES

A.1 Tangent matrix

The tangent matrix can be found as

$$DDW_{iJkL}(F_{n+1},T) = \frac{\partial^2 W_n}{\partial F_{iJ}\partial F_{kL}} = 4\frac{\partial^2 W_n}{\partial C_{IJ}\partial C_{KL}}F_{iI}F_{kK} + \delta_{ik}S_{JL}, \tag{A.1}$$

which leads to

$$DDW_{iJkL}(F_{n+1},T) = 4\mu\sum_{\lambda_{p,n+1}} w_p \frac{\partial}{\partial C_{JL}}\Big((1-q_{p,n+1})^2(1-\lambda_{p,n+1}^{-4})\Big)(F_{n+1}\xi_i)_i(F_{n+1}\xi_i)_k + \delta_{ik}S_{JL}. \tag{A.2}$$

The partial derivative with respect to the first term,

$$\begin{aligned}
&\frac{\partial}{\partial C_{JL}}(1-q_{p,n+1})^2 \\
&= \frac{\partial}{\partial C_{JL}}\left(\frac{A+B\Delta t - A\,q_{p,n}}{A+B\Delta t+\mu(\lambda_{p,n+1}^2+\lambda_{p,n+1}^{-2})\Delta t}\right)^2 \\
&= -\frac{(A+B\Delta t - A\,q_{p,n})^2}{(A+B\Delta t+\mu(\lambda_{p,n+1}^2+\lambda_{p,n+1}^{-2})\Delta t)^3}2\mu\Delta t(1-\lambda_{p,n+1}^{-4})(\xi_p)_J(\xi_p)_L \\
&= -(1-q_{p,n+1})^2\frac{2\mu\Delta t(1-\lambda_{p,n+1}^{-4})(\xi_p)_J(\xi_p)_L}{A+B\Delta t+\mu(\lambda_{p,n+1}^2+\lambda_{p,n+1}^{-2})\Delta t}.
\end{aligned} \tag{A.3}$$

Finally, the tangent matrix results in

$$\begin{aligned}
&DDW_{iJkL}(F_{n+1},T) = \\
&-4\mu\sum_{\lambda_{p,n+1}} w_p\frac{2\mu\Delta t(1-q_{p,n+1})^2(1-\lambda_{p,n+1}^{-4})^2}{A+B\Delta t+\mu(\lambda_{p,n+1}^2-1)\Delta t}(F_{n+1}\xi_p)_i(F_{n+1}\xi_p)_k(\xi_p)_J(\xi_p)_L \\
&+4\mu\sum_{\lambda_{p,n+1}} w_p(1-q_{p,n+1})^2 2\lambda^{-11/2}(1-\lambda^{-4})(F_{n+1}\xi_p)_i(F_{n+1}\xi_p)_k(\xi_p)_J(\xi_p)_L \\
&+\mu\delta_{ik}\sum_{\lambda_{p,n+1}} w_p(1-q_{p,n+1})^2(1-\lambda_{p,n+1}^{-4})(\xi_i)_J(\xi_i)_L.
\end{aligned} \tag{A.4}$$

BIBLIOGRAPHY

[1] Alberts, B., 2015. Molecular biology of the cell, 6th edition. Vol. 36. Garland Science.
URL http://content.wkhealth.com/linkback/openurl?sid=WKPTLP:landingpage{\&}an=00024382-200807000-00020{\%}5Cnhttp://doi.wiley.com/10.1002/bmb.20192

[2] Alberts, B., Johnson, A., Lewis, J., Raff, M., Roberts, K., Walter, P., 2002. Molecular Biology of the Cell, 4th Edition. Garland Science, New York.

[3] Arya, S. K., Lee, K. C., Dah'alan, D. B., Daniel, Rahman, A. R. A., 2012. Breast tumor cell detection at single cell resolution using an electrochemical impedance technique. Lab Chip 12, 2362–2368.
URL http://dx.doi.org/10.1039/C2LC21174B

[4] Balzani, D., Ortiz, M., 2012. Relaxed incremental variational formulation for damage at large strains with application to fiber-reinforced materials and materials with truss-like microstructures. Journal for Numerical Methods in Engineering 92 (6), 551–570.

[5] Barreto, S., Clausen, C. H., Perrault, C. M., Fletcher, D. A., Lacroix, D., 2013. A multi-structural single cell model of force-induced interactions of cytoskeletal components. Biomaterials 34 (26), 6119–6126.
URL http://dx.doi.org/10.1016/j.biomaterials.2013.04.022

[6] Bender, C. M., Orszag, S. A., 1978. Advanced Mathematical Methods for Scientists and Engineers. International series in pure and applied mathematics. McGraw-Hill.

[7] Berman, J. J., 2011. Precancer: The Beginning and the End of Cancer, 1st Edition. Jones & Bartlett Publishers, London, United Kingdom.

[8] Blaber, J., Adair, B., Antoniou, A., 2015. Ncorr: Open-Source 2D Digital Image Correlation Matlab Software. Experimental Mechanics 55 (6), 1105–1122.

[9] Cartagena, A., Raman, A., 2014. Local viscoelastic properties of live cells investigated using dynamic and quasi-static atomic force microscopy methods. Biophysical Journal 106, 1033–1043.

[10] Clarkson, Y. L., McLaughlin, M., Waterfall, M., Dunlop, C. E., Skehel, P. A., Anderson, R. A., Telfer, E. E., 2018. Initial characterisation of adult human ovarian cell populations isolated by ddx4 expression and aldehyde dehydrogenase activity. Scientific reports 8 (1), 6953.

[11] Coleman, B., Noll, W., 1963. The thermodynamics of elastic materials with heat conduction and viscosity. Archive for Rational Mechanics and Analysis 13, 167–179.

[12] Cools, R., 2003. An encyclopaedia of cubature formulas. Journal of Complexity 19 (3), 445 – 453, oberwolfach Special Issue.
URL http://www.sciencedirect.com/science/article/pii/S0885064X03000116

[13] Cross, S. E., Jin, Y.-S., Rao, J., Gimzewski, J. K., 2007. Nanomechanical analysis of cells from cancer patients. Nature Nanotechnology 2, 780–783.

[14] Dahl, K. N., Kahn, S. M., Wilson, K. L., Discher, D. E., 2004. The nuclear envelope lamina network has elasticity and a compressibility limit suggestive of a molecular shock absorber. Journal of Cell Science 117, 4779–4786.

[15] Dassault Systèmes®, 2017. Abaqus Explicit - SIMULIA™. https://www.3ds.com/products-services/simulia/products/abaqus/.

[16] Deshpande, V. S., McMeeking, R. M., Evans, A. G., 2006. A bio-chemo-mechanical model for cell contractility. Proceedings of the National Academy of Sciences 103 (38), 14015–14020.
URL www.pnas.orgcgidoi10.1073pnas.0605837103http://www.pnas.org/cgi/doi/10.1073/pnas.0605837103

[17] Downey, G. P., Doherty, D. E., Schwab, B., Elson, E. L., Henson, P. M., Worthen, G. S., 1990. Retention of leukocytes in capillaries: role of cell size and deformability. Journal of Applied Physiology 69 (5), 1767–1778.
URL http://www.physiology.org/doi/10.1152/jappl.1990.69.5.1767

[18] Fletcher, D. A., Mullins, R. D., 2010. Cell mechanics and the cytoskeleton. Nature 463 (7280), 485–492.
URL http://www.ncbi.nlm.nih.gov/pubmed/20110992

[19] Flory, P. J., 1989. Statistical Mechanics of Chain Molecules. Hanser Publishers, Munich.

[20] Fraldi, M., Cugno, A., Deseri, L., Dayal, K., Pugno, N. M., 2015. A frequency-based hypothesis for mechanically targeting and selectively attacking cancer cells. Journal of The Royal Society Interface 12 (111), 20150656.
URL http://rsif.royalsocietypublishing.org/lookup/doi/10.1098/rsif.2015.0656

[21] Fuhrmann, A., Staunton, J. R., Nandakumar, V., Banyai, N., Davies, P. C. W., Ros, R., 2011. AFM stiffness nanotomography of normal, metaplastic and dysplastic human esophageal cells. Physical Biology 8, 1–10.

[22] Fushimi, K., Verkman, A. S., 1991. Domain of cell cytoplasm measured by picosecond polarization microfluorimetry. Journal of Cell Biology 112, 719–725.

[23] Garven, H. S. D., 1965. A STUDENT'S HISTOLOGY, 2nd Edition. URL https://physoc.onlinelibrary.wiley.com/doi/abs/10.1113/expphysiol.1967.sp001926

[24] Guilak, F., Tedrow, J. R., Burgkart, R., 2000. Viscoelastic properties of the cell nucleus. Biochemical and Biophysical Research Communications 269, 781–786.

[25] Guttman, P. H., Halpern, S., 1935. Nuclear-nucleolar volume ratio in cancer. American Journal of Cancer 25 (4), 802–806.

[26] Heyden, S., Conti, S., Ortiz, M., 2015. A nonlocal model of fracture by crazing in polymers. Mechanics of Materials 90, 131–139.

[27] Heyden, S., Li, B., Weinberg, K., Conti, S., Ortiz, M., 2015. A micromechanical damage and fracture model for polymers based on fractional strain-gradient elasticity. Journal of the Mechanics and Physis of Solids 74, 175–195.

[28] Heyden, S., Ortiz, M., 09 2016. Investigation of the influence of viscoelasticity on oncotripsy. Computer Methods in Applied Mechanics and Engineering 314.

[29] Heyden, S., Ortiz, M., 2016. Oncotripsy: Targeting cancer cells selectively via resonant harmonic excitation. Journal of the Mechanics and Physics of Solids 92, 164–175.

[30] Hughes, T. J. R., 2000. The finite element method : linear static and dynamic finite element analysis /, xxii, 682 p. :Reprint. Originally published: Englewood Cliffs, N.J. : Prentice-Hall, 1987. The author has corrected minor errors in the text and deleted the sections of Chapters 10 and 11 that are no longer necessary. URL http://caltech.tind.io/record/676251

[31] Ingber, D. E., 2003. Tensegrity II. How structural networks influence cellular information processing networks. Journal of Cell Science 116 (8), 1397–1408.

[32] Janmey, P. A., 1998. The cytoskeleton and cell signaling: component localization and mechanical coupling. Physiol Rev 78, 763–781.

[33] Jensen, M. H., Morris, E. J., Weitz, D. A., November 2015. Mechanics and dynamics of reconstituted cytoskeletal systems. Biochim Biophys Acta 1853 (11 0 0), 3038–3042.

[34] Kang, G., Kim, Y.-j., Moon, H.-s., Lee, J.-W., Yoo, T.-K., Park, K., Lee, J.-H., 2013. Discrimination between the human prostate normal cell and cancer cell by using a novel electrical impedance spectroscopy controlling the cross-sectional area of a microfluidic channel. Biomicrofluidics 7 (4), 044126.

[35] Kardas, D., Nackenhorst, U., Balzani, D., 2013. Computational model for the cell-mechanical response of the osteocyte cytoskeleton based on self-stabilizing tensegrity structures. Biomechanics and Modeling in Mechanobiology 12 (1), 167–183.

[36] Keshtkar, A., Keshtkar, A., Lawford, P., 2007. Cellular morphological parameters of the human urinary bladder (malignant and normal). International journal of experimental pathology 88 (3), 185–190.

[37] Kim, Y., Kim, M., Shin, J. H., Kim, J., 2011. Characterization of cellular elastic modulus using structure based double layer model. Med Biol Eng Comput 49 (4), 453–462.
URL http://link.springer.com/10.1007/s11517-010-0730-yhttp://www.ncbi.nlm.nih.gov/pubmed/21221828https://link.springer.com/content/pdf/10.1007{\%}2Fs11517-010-0730-y.pdf

[38] Konno, K. I., Kosawada, T., Kaneyama, Y., Endo, H., Feng, Z., 2013. Non-invasive stiffness detection method for living cell nucleus by using piezoelectric micro sensor. IFMBE Proceedings 39 IFMBE, 290–293.

[39] Labati, R. D., Piuri, V., Scotti, F., 2011. ALL-IDB : The Acute Lymphoblastic Leukemia Image Database for Image Processing. IEEE International Conference on Image Processing (ICIP), 2045–2048.

[40] Lammerding, J., 2011. Mechanics of the Nucleus. American Cancer Society, pp. 783–807.
URL https://onlinelibrary.wiley.com/doi/abs/10.1002/cphy.c100038

[41] Lekka, M., Gil, D., Pogoda, K., Dulińska-Litewka, J., Jach, R., Gostek, J., Klymenko, O., Prauzner-Bechcicki, S., Stachura, Z., Wiltowska-Zuber, J., et al., 2012. Cancer cell detection in tissue sections using afm. Archives of biochemistry and biophysics 518 (2), 151–156.

[42] Lekka, M., Laidler, P., Gil, D., Lekki, J., Stachura, Z., Hrynkiewicz, A., 1999. Elasticity of normal and cancerous human bladder cells studied by scanning force microscopy. European Biophysics Journal 28 (4), 312–316.

[43] Levental, K. R., Yu, H., Kass, L., Lakins, J. N., Egeblad, M., Erler, J. T., 2009. Matrix crosslinking forces tumor progression by enhancing integrin signaling. Cell 139, 891–906.

[44] Li, J., Dao, M., Lim, C. T., Suresh, S., 2005. Spectrin-level modeling of the cytoskeleton and optical tweezers stretching of the erythrocyte. Biophysical Journal 88 (5), 3707–3719.

[45] Li, M., Liu, L., Xi, N., Wang, Y., Dong, Z., Xiao, X., Zhang, W., 2012. Atomic force microscopy imaging and mechanical properties measurement of red blood cells and aggressive cancer cells. Science China Life Sciences 55 (11), 968–973.
URL http://link.springer.com/10.1007/s11427-012-4399-3

[46] Li, S., Sun, B., 2011. Advances in Cell Mechanics. Springer.

[47] Lim, C. T., Zhou, E. H., Quek, S. T., 2006. Mechanical models for living cells–a review. J Biomech 39 (2), 195–216.
URL http://www.ncbi.nlm.nih.gov/pubmed/16321622

[48] Liu, T., Liu, X., Spring, D. R., Xuhong Qian, X., Cui, J., Xu, Z., 2014. Quantitatively mapping cellular viscosity with detailed organelle information via a designed pet fluorescent probe. Scientific Reports 4, 5418.

[49] Lodish, H., Berk, A., Matsudaira, P., Kaiser, C. A., Krieger, M., Scott, M. P., Zipursky, S. L., Darnell, J., 2004. Molecular Cell Biology, 5th Edition. WH Freeman, New York.

[50] Luby-Phelps, K., Castle, P. E., Taylor, D. L., Lanni, F., 1987. Hindered diffusion of inert tracer particles in the cytoplasm of mouse 3t3 cells. Proceedings of the National Academy of Sciences 84 (14), 4910–4913.
URL https://www.pnas.org/content/84/14/4910

[51] Luby-Phelps, K., Mujumdar, S., Mujumdar, R. B., Ernst, L. A., Galbraith, W., Waggoner, A. S., 1993. A novel fluorescence ratiometric method confirms the low solvent viscosity of the cytoplasm. Byophisical Journal 65, 236–242.

[52] Marsden, J. E., Hughes, T. J. R., 1994. Mathematical Foundations of Elasticity. Dover Civil and Mechanical Engineering Series. Dover.
URL https://books.google.com/books?id=RjzhDL5rLSoC

[53] Milo, R., Phillips, R., 2017. Cell Biology by the Numbers, 1st Edition. Garland Science.

[54] Mittelstein, D. R., Ye, J., Schibber, E. F., Roychoudhury, A., Martinez, L. T., Fekrazad, M. H., Ortiz, M., Lee, P. P., Shapiro, M. G., Gharib, M., 2019. Selective ablation of cancer cells with low intensity pulsed ultrasound. bioRxiv.
URL https://www.biorxiv.org/content/early/2019/10/01/779124

[55] Mizrahi, N., Zhou, E. H., Lenorman, G., Krishnan, R., Weihs, D., Butler, J. P., Weitz, D. A., Fredberg, J. J.and Kimmel, E., February 2012. Low intensity ultrasound perturbs cytoskeleton dynamics. Soft Matter 8 (8), 2438–2443.

[56] Mofrad, M. R. K., 2009. Rheology of the cytoskeleton. Annual Review of Fluid Mechanics 41, 433–453.

[57] Nakamura, M., M., D. A. N., Decker, J. R., Hull, A. J., Verboon, J. M., Parkhurst, S. M., 2018. Into the breach: how cells cope with wounds. Open Biolology, 180135Http://dx.doi.org/10.1098/rsob.180135.

[58] Nematbakhsh, Y., Pang, K. T., Lim, C. T., 2017. Correlating the viscoelasticity of breast cancer cells with their malignancy. Convergent Science Physical Oncology 3 (3), 034003.
URL https://doi.org/10.1088/2057-1739/aa7ffb

[59] Noriega, S., Hasanova, G., Subramanian, A., 2013. The effect of ultrasound stimulation on the cytoskeletal organization of chondrocytes seeded in three-dimensional matrices. Cells Tissues Organs 197 (1), 14–26.

[60] Nowak, M. A., 2006. Evolutionary dynamics: exploring the equations of life. Belknap Press of Harvard University Press, Cambridge, Mass.

[61] Or, M., Kimmel, E., 2009. Modeling Linear Vibration of Cell Nucleus in Low Intensity Ultrasound Field. Ultrasound in Medicine and Biology 35 (6), 1015–1025.

[62] Ortiz, M., Stainier, L., 1999. The variational formulation of viscoplastic constitutive updates. Computer Methods in Applied Mechanics and Engineering 171 (3), 419 – 444.
URL http://www.sciencedirect.com/science/article/pii/S0045782598002199

[63] Panorchan, P., Lee, J. S. H., Kole, T. P., Tseng, Y., Wirtz, D., 2006. Microrheology and rock signaling of human endothelial cells embedded in a 3d matrix. Biophysical Journal 91, 3499–3507.

[64] Paszek, M. J., Zahir, N., Johnson, K. R., Lakins, J. N., Rozenberg, G. I., Gefen, A., 2005. Tensional homeostasis and the malignant phenotype. Cancer Cell 8, 241–254.

[65] Rosenbluth, M. J., Lam, W. A., Fletcher, D. A., 2006. Force microscopy of nonadherent cells: A comparison of leukemia cell deformability. Biophysical Journal 90 (8), 2994–3003.
URL https://ac.els-cdn.com/S0006349506724808/1-s2.0-S0006349506724808-main.pdf?{_}tid=271be2a6-ac8a-11e7-b192-00000aab0f01{\&}acdnat=1507509682{_}8c2fad407a0a66907ddaef5483701d8fhttp://linkinghub.elsevier.com/retrieve/pii/S0006349506724808

[66] Samandari, M., Abrinia, K., Mokhtari-Dizaji, M., Tamayol, A., 2017. Ultrasound induced strain cytoskeleton rearrangement: An experimental and simulation study. Journal of Biomechanics 60, 39–47.

[67] Schibber, E. F., Mittelstein, D. R., Gharib, M., Shapiro, M. G., Lee, P. P., Ortiz, M., 2019. A dynamical model of oncotripsy by mechanical cell fatigue: Selective cancer cell ablation by low-intensity pulsed ultrasound.

[68] Schibber, E. F., Salahshoor, H., Ortiz, M., 2019. Quantitative oncotripsy, work in progress.

[69] Schmid-Schonbein, G. W., Sung, K.-L. P., Tozeren, H., Skalak, R., Chien, S., 1981. PASSIVE MECHANICAL PROPERTIES OF HUMAN LEUKOCYTES. Biophysical Journal 36, 243–256.
URL https://ac.els-cdn.com/S0006349581847261/1-s2.0-S0006349581847261-main.pdf?{_}tid=6f42d16a-ac8b-11e7-a0d8-00000aacb360{\&}acdnat=1507510232{_}5192b891c103e0db402ba7d9dd949a95

[70] Schrader, J., Gordon-Walker, T. T., Aucott, R. L., van Deemter, M., Quaas, A., Walsh, S., Benten, D., Forbes, S. J., Wells, R. G., Iredale, J. P., 2011. Matrix stiffness modulates proliferation, chemotherapeutic response, and dormancy in hepatocellular carcinoma cells. Hepatology 53 (4), 1192–1205.

[71] Smith1, M., Hoffman, L. M., Beckerle, M. C., October 2014. Lim proteins in actin cytoskeleton mechanoresponse. Trends in Cell Biologyl 24 (10), 575–583.

[72] Smolyakov, G., Thiebot, B., Campillo., Labdi, S., Severac, C., Pelta, J., Dague, E., 2016. Elasticity, Adhesion, and Tether Extrusion on Breast Cancer Cells Provide a Signature of Their Invasive Potential. ACS Applied Materials and Interfaces 8 (41), 27426–27431.

[73] Sullivan, T. J., 2015. Introduction to Uncertainty Quantification. Vol. 63 of Texts in Applied Mathematics. Springer.
URL http://dx.doi.org/10.1007/978-3-319-23395-6

[74] Suresh, S., 1998. Fatigue of Materials. Cambridge University Press, Cambridge, Mass.

[75] Suresh, S., 2007. Biomechanics and biophysics of cancer cells. Acta Biomaterialia 3 (4), 413–438.
URL http://www.ncbi.nlm.nih.gov/pubmed/17540628

[76] Swaminathan, V., Mythreye, K., O'Brien, E. T., Berchuck, A., Blobe, G. C., Superfine, R., 2011. Mechanical stiffness grades metastatic potential in patient tumor cells and in cancer cell lines. Cancer Research 71 (15), 5075–5080.

[77] Taylor, H. B., Khuong, A., Wu, Z., Xu, Q., Morley, R., Gregory, L., Poliakov, A., Taylor, W. R., Wilkinson, D. G., 2017. Cell segregation and border sharpening by eph receptor–ephrin-mediated heterotypic repulsion. Journal of The Royal Society Interface 14 (132), 20170338.

[78] Thompson, G., Roth, C., Tolstykh, G., Kuipers, M., Ibey, B., 02 2013. Role of cytoskeleton and elastic moduli in cellular response to nanosecond pulsed electric fields. In: Progress in Biomedical Optics and Imaging - Proceedings of SPIE. Vol. 8585.

[79] Thoumine, O., Ott, A., 1997. Time scale dependent viscoelastic and contractile regimes in fibroblasts probed by microplate manipulation. Journal of cell science 110 (Pt 1, 2109–16.
URL http://www.ncbi.nlm.nih.gov/pubmed/9378761

[80] Treloar, L. R. G., 2005. The physics of rubber elasticity /, xii, 310 p. :This ed. originally published: Oxford: Clarendon, 1975.
URL http://caltech.tind.io/record/683214

[81] Weiner, J. H., 2002. Statistical Mechanics of Elasticity, 2nd Edition. Dover Publications, Mineola, N. Y.

[82] Xu, W., Mezencev, R., Kim, B., Wang, L., McDonald, J., Sulchek, T., 2012. Cell stiffness is a biomarker of the metastatic potential of ovarian cancer cells. PloS one 7 (10), e46609.

[83] Yanenko, N. N., 1971. The method of fractional steps: Solution of problems of mathematical physics in several variables. Springer.

[84] Zhang, G., Long, M., Wu, Z.-Z., Yu, W.-Q., 2002. Mechanical properties of hepatocellular carcinoma cells. World Journal of Gastroenterology 8 (2), 243–246.

[85] Zhou, Z. L., Hui, T. H., Tang, B., Ngan, A. H. W., 2014. Accurate measurement of stiffness of leukemia cells and leukocytes using an optical trap by a rate-jump method. RSC Advances 4 (17), 8453.
URL http://xlink.rsc.org/?DOI=c3ra45835k

[86] Zipursky, A., Bow, E., Seshadri, R., Brown, E., 1976. Leukocyte density and volume in normal subjects and in patients with acute lymphoblastic leukemia. Blood 48 (3), 361–371.
URL http://www.bloodjournal.org/content/48/3/361